PERFORMANCE ANALYSIS OF AN INTERCONNECTED MINI-CHANNEL HEAT SINK WITH WAVY WALL

by

Abdul Aziz Shuvo

MASTER OF SCIENCE IN MECHANICAL ENGINEERING

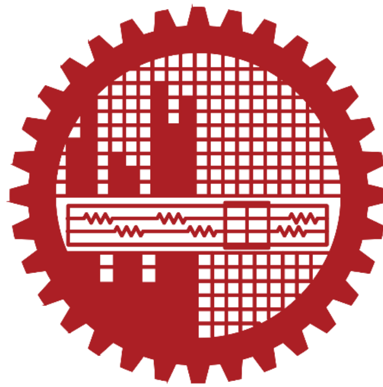

Department of Mechanical Engineering

BANGLADESH UNIVERSITY OF ENGINEERING AND TECHNOLOGY

June 2022

The thesis titled **"PERFORMANCE ANALYSIS OF AN INTERCONNECTED MINI-CHANNEL HEAT SINK WITH WAVY WALL"** submitted by **Abdul Aziz Shuvo**, St. Id: **0419102021**, Session: **April 2019**, has been accepted as satisfactory in partial fulfillment of the requirement for the degree of **Master of Science in Mechanical Engineering** on June 07, 2022.

BOARD OF EXAMINERS

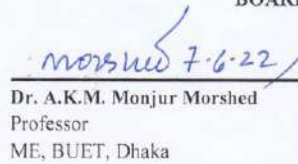

Dr. A.K.M. Monjur Morshed
Professor
ME, BUET, Dhaka

Chairman
(Supervisor)

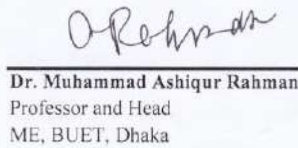

Dr. Muhammad Ashiqur Rahman
Professor and Head
ME, BUET, Dhaka

Member
(Ex-officio)

Dr. Md. Zahurul Haq
Professor
ME, BUET, Dhaka

Member

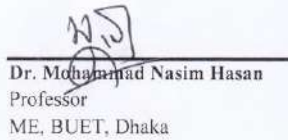

Dr. Mohammad Nasim Hasan
Professor
ME, BUET, Dhaka

Member

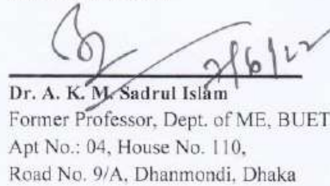

Dr. A. K. M. Sadrul Islam
Former Professor, Dept. of ME, BUET
Apt No.: 04, House No. 110,
Road No. 9/A, Dhanmondi, Dhaka

Member
(External)

CANDIDATE’S DECLARATION

It is hereby declared that this thesis or any part of it has not been submitted elsewhere for any award, degree, or diploma.

June 2022

Abdul Aziz Shuvo

ACKNOWLEDGEMENTS

First and Foremost, I would like to thank the Almighty Allah for giving me the strength to complete this work.

I would like to express my sincere gratitude to my honorable supervisor, Dr. A.K.M. Monjur Morshed, for his continuous support, encouragement, motivation, and guidance throughout all phases of this M.Sc. study. Without his persistent advice and support, this dissertation would not be possible. It has been a great privilege and honor for me to work with him.

I would like to thank the members of my thesis evaluation committee, Dr. Muhammad Ashiqur Rahman, Dr. Md. Zahurul Haq, Dr. Mohammad Nasim Hasan and Dr. A. K. M. Sadrul Islam for their valuable comments and suggestions.

I am also grateful to Dr. Titan C. Paul, Associate Professor, Mechancial Engineering Department, University of South Carolina Aiken, USA, and Amitav Tikadar, Graduate Research Assistant, Mechanical Engineering Department, Georgia Tech, USA for their continuous support and guidance.

Finally, I would like to thank my mother and my wife for their encouragement and support, without which this dissertation and research would not have been possible.

“Dream is not that which you see while sleeping;

It is something that does not let you sleep.”

– A.P.J. ABDUL KALAM

ABSTRACT

Due to recent breakthroughs in mini/micro-scale electronics systems, the need for an innovative thermal management solution to dissipate large quantity of heat from a limited space has grown increasingly to assure device reliability. Liquid cooling micro/mini-channel has been found effective in this regard and already found application in microelectronics cooling; however it causes significant pressure drop penalty. To further improve its performance, different researchers have taken different approaches by modifying geometry, surface morphology, altering thermal properties of the coolant, using active or passive heat transfer augmentation techniques, etc. In this study, a novel heat sink design has been proposed for mini-channel heat sink with sinusoidal wavy surface walls and interconnections between channels. The thermal performance of the proposed heat sink has been numerically investigated with commercially available software FLUENT and the results has been compared with conventional minichannel heat sink. Effect of different parameters of the proposed heat sink, i.e., wavelengths, wave amplitudes, and phase shifts of the sinusoidal wavy MCHS have been also investigated in this study. Three different wavelengths, three different amplitudes, and two different phase shifts are used in this study and Reynold number (*Re*) of the channel is varied from *300* to *800*. The Nusselt number (*Nu*) of IC w-MCHS increases as the wave amplitude ratio (α) and *Re* increases whereas it increases with the decrement of the wavelength ratio (β). *Nu* of the IC w-MCHS also depends on phase shift (θ_p). At $\theta_p = \pi$, the chaotic advection and flow reversal increase in the IC w-MCHS compared to $\theta p = 0$, resulting in higher *Nu* and higher pressure drop. Maximum *Nu* of the IC w-MCHS is found to be *115%* higher at *Re 550*, $\theta_p = \pi$, and $\alpha = 0.3$ compared to s-MCHS and it is found *77%* higher at *Re 550*, $\theta_p = 0$, and $\alpha = 0.3$. As the IC w-MCHS enhances the mixing of the coolant, the maximum temperature is also found to decrease compared to the s-MCHS. Maximum temperature of the heat sink has been found to decrease up to *24%* at *Re 800*, $\theta_p = \pi$, $\alpha = 0.3$, and $\beta = 0.08$ and up to *15%* for $\theta_p = 0$. Pressure drop in IC w-MCHS is also found to be lower than the w-MCHS without interconnectors (w-MCHS).

TABLE OF CONTENTS

CANDIDATE’S DECLARATION iii
ACKNOWLEDGEMENTS iv
ABSTRACT vii
LIST OF FIGURES xi
LIST OF TABLES xiv
NOMENCLATURE xv
.... xvii
CHAPTER 1: INTRODUCTION 1
1.1 Convection Heat Transfer 1
1.1.1 Natural Convection 2
1.1.2 Forced Convection 2
1.2 Boundary Layers 2
1.2.1 Velocity Boundary layers 2
1.2.2 Thermal Boundary Layer 3
1.3 Improvement of Heat Transfer 3
1.3.1 Active Techniques 4
1.3.2 Passive Techniques 5
1.3.3 Compound Techniques 5
1.4 Thermal Management of Power Electronics 5
1.5 Micro-/Mini-channel Heat Sink 6
1.6 Motivation of the Present Study 6
1.7 Main Objectives of the Thesis 8
1.8 Layout of The Thesis 9
CHAPTER 2: LITERATURE REVIEW 10

2.1 Introduction 10

2.2 Existing Literature on Micro-channel and Mini-Channel Heat Sink 10

2.3 Heat Transfer Enhancement by Geometry Modification 11

2.4 Heat Transfer Enhancement by Waviness 11

2.5 Heat Transfer Enhancement by Secondary Flow 13

2.6 Summary 14

CHAPTER 3: NUMERICAL MODELLING.. 15

3.1 Computational Fluid Dynamics 15

3.2 Ansys FLUENT.. 16

3.3 Mathematical Modeling 2D Wavy MCHS (w-MCHS) 16

3.3.1 Geometry of 2D w-MCHS... 16

3.3.2 Mesh Independence Test 18

3.3.3 Governing Equations 19

3.3.4 Boundary Conditions.. 19

3.3.4 Data Analysis.. 20

3.4 Mathematical Modeling 3D Wavy MCHS with Interconnectors (IC w-MCHS) 21

3.4.1 Geometry of 3D IC w-MCHS 21

3.4.2 Mesh Independence Test 25

3.4.3 Governing Equations 26

3.4.4 Boundary Conditions.. 27

3.4.4 Data Analysis.. 27

CHAPTER 4: RESULTS AND DISCUSSION... 29

4.1 Model Validation.. 29

4.2 Effect of Phase Shift in 2D w-MCHS 31

4.3 Effect of Sinusoidal Waviness and Interconnectors in 3D MCHS 40

4.3.1 Pressure and Velocity Distribution 40
4.3.2 Local Temperature Distribution 47
4.3.3 Maximum Temperature Reduction... 48
4.3.4 Maximum Heat Flux Extraction 48
4.3.5 Effect on Nusselt Number 49
4.3.6 Performance Evaluation Criteria 51
4.4 Effect of Amplitude and Wavelength in 3D IC w-MCHS 52
4.4.1 Effect of Amplitude and Wavelength in Cross Flow................................ 52
4.4.2 Local Temperature Distribution 54
4.4.3 Effect on Nusselt Number 57
4.4.4 Effect on Friction Factor and PEC 57
CHAPTER 5: CONCLUSIONS 62
REFERENCES 64

LIST OF FIGURES

Figure 1.1: Variation of friction factor (f_x) and convective heat transfer coefficient (h_x) in flow direction for flow in tube ($Pr>1$) [1] 4
Figure 1.2: Increasing degree of integration in mobile application processor (Qualcomm SnapdragonTH family) [10] 7
Figure 1.3: Power consumption trend of microelectronics [11] 8
Figure 3.1: The schematics of (a) w-MCHS and (b) its mesh for different phase shifts 18
Figure 3.2: (a) Computational domain of IC w-MCHS (b) Top view of IC w-MCHS at $\theta_p = 0, \pi$ (c) front view of IC w-MCHS at $\theta_p = 0$ (d) front view of IC w-MCHS at $\theta_p = \pi$ (e) left side view of IC w-MCHS, $\theta_p = 0, \pi$ 23
Figure 3.3: Schematic of (a) conventional mini-channel heat sink (s-MCHS) (b) straight mini-channel heat sink with interconnectors (IC s-MCHS) (c) wavy mini-channel heat sink without interconnectors at $\theta_p = 0$ (w-MCHS, $\theta_p = 0$) (d) wavy mini-channel heat sink without interconnectors at $\theta_p = \pi$ (w-MCHS, $\theta_p = \pi$) 24
Figure 3.4: Meshed computational domain of (a) IC w-MCHS, $\theta_p = 0$ (b) IC w-MCHS, $\theta_p = \pi$ 26
Figure 4.1: (a) Comparison of *Nu* with Fan *et al.* [46], Ho *et al.* [54], and Shah and London [53] (b) comparison of f with Shah and London [20] correlation for distinct *Re* 30
Figure 4.2: (a) Comparison of *Nu* of interconnected Mini-channel Heat Sink (IC s-MCHS) with Tikadar *et al.* [48] at different *Re*. The maximum deviation was less than *2%* (b) Comparison of *Nu* and ΔP with Gong *et al.* [39] for different wavelengths at $Re=150$ 31
Figure 4.3: Streamline and velocity profile in wavy microchannel for (a) θ_p=0 (case 1) (b) θ_p= π/2 (case 2) (c) θ_p= π (case 3) at *Re* 700 and $W_L = 14\ mm$ 33
Figure 4.4: Streamline and velocity profile in wavy microchannel for (a) θ_p=0 (case 4) (b) θ_p= π/2 (case 5) (c) θ_p= π (case 6) at *Re* 700 and W_L = 7 mm 34

Figure 4.5: Variation of average *Nu* with *Re* for wavy channel (a) W_L = 14 mm (case 1- case 3) (b) W_L = 7 mm (case 4- case 6) (c) W_L = 3.5 mm (case 7- case 9) 36
Figure 4.6: (a) Maximum induced velocity for W_L= *14 mm* (*case 1- case 3*) (b) maximum induced velocity for W_L =*7mm* (*case 4- case 6*) (c) maximum induced velocity for W_L =*3.5 mm* (*case 7- case 9*).. 38
Figure 4.7: Variation *f* with *Re* for wavy channel (a) W_L= *14 mm* (*case 1- case 3*) (b) W_L = 7 mm (*case 4- case 6*) (c) W_L = 3.5 mm (*case 7- case 9*) 39
Figure 4.8: Pressure and velocity profile in center plane of the MCHS at *Re = 800* 41
Figure 4.9: (a) Streamline (*x = 0.13 mm*) in the MCHS (b) velocity vector field at *z = 0.45 mm* velocity contour in the ZX plane of the MCHS at *Re = 800* 42
Figure 4.10: Velocity contour in the ZX plane of the MCHS at *Re = 800*................ 43
Figure 4.11: Pressure and velocity along with centerline in XY-plane (a) IC s-MCHS (b) w-MCHS, $\theta_p = 0$ (c) IC w-MCHS, $\theta_p = 0$ (d) w-MCHS, $\theta_p = \pi$ (e) IC w-MCHS, $\theta_p = \pi$.. 46
Figure 4.12: Variation of friction factor (*f*) with *Re* for $\alpha= 0.2$ and $\beta= 0.08$........ 46
Figure 4.13: Local temperature distribution at the bottom of the microchannel at *Re = 800*.. 47
Figure 4.14: Maximum bottom temperature of MCHS at constant heat flux, *q''= 32 W/cm*^{2} 48
Figure 4.15: Maximum heat flux (*q''*) for different MCHS at maximum temperature 85^{0}C.. 49
Figure 4.16: (a) Variation of *Nu* with *Re* (b) Variation of Nusselt number ratio with *Re = 800* for $\alpha= 0.2$ and $\beta= 0.08$ 51
Figure 4.17: Variation of *PEC* with *Re* for $\alpha= 0.2$ and $\beta= 0.08$............................... 52
Figure 4.18 (a) Variation of % of cross flow with different amplitude ratio, α at *Re =800* (b) Variation of % of cross flow with different wavelength ratio, β at *Re =800* (c) cross-sectional area's of interconnector for different amplitude ratio, α where $\beta=0.08$ (d) cross-sectional area's of interconnector for different amplitude ratio, β where $\alpha=0.2$ 53
Figure 4.19: Variation of local temperature of bottom surface of MCHS at *Re=800* for (a) $\alpha = 0.15$ (b) $\alpha = 0.2$ (c) $\alpha = 0.3$ (d) $\beta = 0.06$ (e) $\beta = 0.08$ (d) $\beta = 0.15$............... 55

Figure 4.20: Variation of maximum bottom temperature (^{o}C) with Re under constant heat flux ($q''=32W/m^2$) for (a) $\alpha = 0.15$ (b) $\alpha = 0.2$ (c) $\alpha = 0.3$ (d) $\beta = 0.06$ (e) $\beta = 0.08$ (d) $\beta = 0.15$ 56
Figure 4.21: Variation of Nusselt number ratio, *Nu* with *Re* for (a) $\alpha = 0.15$ (b) $\alpha = 0.2$ (c) $\alpha = 0.3$ (d) $\beta = 0.06$ (e) $\beta = 0.08$ (d) $\beta = 0.15$ 58
Figure 4.22: Variation of Nusselt number ration, Nu/Nu_o with *Re* for (a) $\alpha = 0.15$ (b) $\alpha = 0.2$ (c) $\alpha = 0.3$ (d) $\beta = 0.06$ (e) $\beta = 0.08$ (d) $\beta = 0.15$ 59
Figure 4.23: Variation of friction factor, *f* with *Re* for (a) $\alpha = 0.15$ (b) $\alpha = 0.2$ (c) $\alpha = 0.3$ (d) $\beta = 0.06$ (e) $\beta = 0.08$ (d) $\beta = 0.15$ 60
Figure 4.24: Variation of *PEC* with *Re* for (a) $\alpha = 0.15$ (b) $\alpha = 0.2$ (c) $\alpha = 0.3$ (d) $\beta = 0.06$ (e) $\beta = 0.08$ (d) $\beta = 0.15$ 61

LIST OF TABLES

Table 1: Channel classification by Kandlikar and Grande [9] 6
Table 2: Case-specific 2D w-MCHS 17
Table 3: Grid independent test for 2D w-MCHS 18
Table 4: The dimension of IC w-MCHS's parameters 21
Table 5: The combination of variable parameters in the study 22
Table 6: Grid independent test for 3D IC w-MCHS 25

NOMENCLATURE

q''_{eff}	effective heat flux, $W.m^{-2}$
Q	total heat input, W
T_w	wall temperature, K
T_f	fluid temperature, K
T_{sol}	solid temperature, K
k	coolant thermal conductivity, $W.m^{-1}.K^{-1}$
K_{sol}	solid thermal conductivity, $W.m^{-1}.K^{-1}$
L	total length, mm
D_h	hydraulic diameter, mm
A_c	cross-sectional area, mm^2
V	velocity of the fluid, ms^{-1}
p	local pressure. Pa
ΔP	pressure drop, Pa
u, v, w	fluid velocity in x, y and z direction
h	convection heat transfer coefficient, $W.m^2.K^{-1}$
$\dot{m}$	mass flow rate, kg/s
W_A	wave amplitude, mm
W_L	wavelength, mm
θ_p	wave phase shift
IC	interconnector
MCHS	mini-channel heat sink
w-MCHS	wavy MCHS with no interconnectors
IC w-MCHS	interconnected wavy MCHS
IC s-MCHS	interconnected straight MCHS
s-MCHS	conventional Straight MCHS with no interconnectors
C1	channel 1
C2	channel 2

Non-dimensional parameter

Re	Reynolds number
Nu	Nusselt number
f	friction factor
PEC	Performance Evaluation Criteria

Greek letters

ρ	density, kgm^{-3}
μ	dynamic viscosity, Pas
α	wave amplitude ratio, W_A/H
β	wavelength ratio, W_L/H
θ_p	wave phase shift

Subscript

in	inlet
out	outlet
eff	effective
m	mean
b	bottom wall
w	wall
c	cross-section
o	s-MCHS
max	maximum
t	total
sol	solid

CHAPTER 1: INTRODUCTION

Heat transfer is an area of science that focuses on thermal energy transfer. Heat transfer is a regular occurrence in our everyday lives. Heat transfer is dealt with by various mechanical equipment such as air conditioners, refrigerators, etc. Heat transfer takes place in a variety of ways. Forced convection heat transfer is an essential mode of heat transfer. Steam generation and condensation in power plants and cooling modern electrical gadgets are common examples of forced convective heat transfer. As convective heat transfer plays a vital role in energy and thermal science, numerous researches are being conducted to enhance heat transfer. Experimental investigations can have some limitations, such as being time-consuming and costly. So, Computational Fluid Dynamics (CFD) is now a widely used method for the design and study of heat transfer problems. CFD can anticipate solutions that are close to those found in experiments.

1.1 Convection Heat Transfer

Convection, also known as convective heat transfer, is the movement of fluids that allows heat to be transferred from one location to another. When it comes to heat transfer in fluids, convection is probably the most common method. Convection is more sophisticated than conduction (heat diffusion) and radiation. Energy is transmitted as heat in thermal conduction, either by the movement of free electrons or the vibrational waves of the lattice (phonons). The temperature gradient is necessary for heat transfer by conduction. Medium is required for both conduction and convection. However, convection needs the presence of fluid motion, whereas conduction does not. It is important to note that energy flow at the surface occurs solely by conduction. This is occurred due to no slip condition. However, the overall convective heat transfer is caused by both the random motion of molecules and the fluid's bulk motion. The convective heat transfer can be natural convection and forced convection based on fluid motion.

1.1.1 Natural Convection

Natural convection is a heat transfer process in which fluid motion is affected by buoyancy force. The fluid density varies as a result of the temperature gradient in this mechanism. As a result, the lighter hot fluid rises while, the denser cold fluid moves closer to the heated surface. As a result, the fluid circulates naturally, with the cold fluid rising after being heated and the surrounding cold fluid filling the space. This mechanism transfers thermal energy from the heated surface to the relatively cold fluid layer. Natural convection is significant because it occurs in nature and engineering applications.

1.1.2 Forced Convection

Forced convection is a heat transfer method in which fluids are forced to circulate in order to increase heat transfer. A ceiling fan, a pump, a suction device, or other equipment can exert this force. As a result, when compared to natural convection, the heat transfer rate increases dramatically. Forced convection can be controlled by changing the fluid velocity, whereas spontaneous convection happens independently. Heat exchangers, pipe flow, duct design in air conditioning systems, steam turbines, lid-driven cavity flow, and other applications use forced convection.

1.2 Boundary Layers

1.2.1 Velocity Boundary layers

When a viscous fluid is pumped to flow over a nonporous solid surface, it is seen that the fluid in motion has zero velocity relative to the surface. This condition is called no slip condition. The no slip condition causes the development of the velocity profile for flow. The layer that adheres to the wall slows the following fluid layer, which slows the next layer, and so on, due to friction between the fluid layers. The region of the viscous flow above the solid surface is termed velocity boundary layer and the thickness of the boundary layer is known as velocity boundary layer thickness, δ_h. The boundary layer thickness gradually grows in flow direction and it merges at the centerline of the duct in case of internal flow. The area between the tube inlet and the point where the boundary layer merges at the centerline is defined as the hydrodynamic entrance region. Flow in the entrance zone is also referred to as hydrodynamically

developing flow. The hydrodynamically fully developed region is the area beyond the entrance region where the velocity profile is entirely developed and remains unchanged. The distance from inlet to hydrodynamic developed region is called hydrodynamic entrance length, L_h as shown in fig 1.1.

1.2.2 Thermal Boundary Layer

When the fluid flows over a nonporous solid surface having more temperature than fluid. A temperature gradient is developed among the adjacent fluid layers. The thermal boundary layer is the layer up to which the temperature gradient exists. Thermal boundary layer thickness, δ_t develops in the flow direction. The growth of the thermal boundary layer becomes unaltered in the thermally fully developed region. The thermal entrance length, L_t is the distance between the inlet and the thermally fully developed zone, as shown in fig 1.1. The relation between L_t and L_h in circular tube is given below [1, 2]:

$$L_t = Pr\, L_h \tag{1.1}$$

Here, Pr is called Prandtl Number. As illustrated in fig 1.1, both local friction factor, f_x, and local heat transfer coefficient, h_x become constant in fully developed regions. Heat transfer and pumping power are higher in the thermal and hydrodynamic developing region.

1.3 Improvement of Heat Transfer

Heat Transfer can be enhanced by increasing effective heat transfer surface area and interrupting and redeveloping the thermal boundary layer. Heat transfer can also be enhanced by improving the physical properties of the flowing fluids. The heat transfer coefficient is greater for the fluid with high thermal conductivity and volume specific heat.

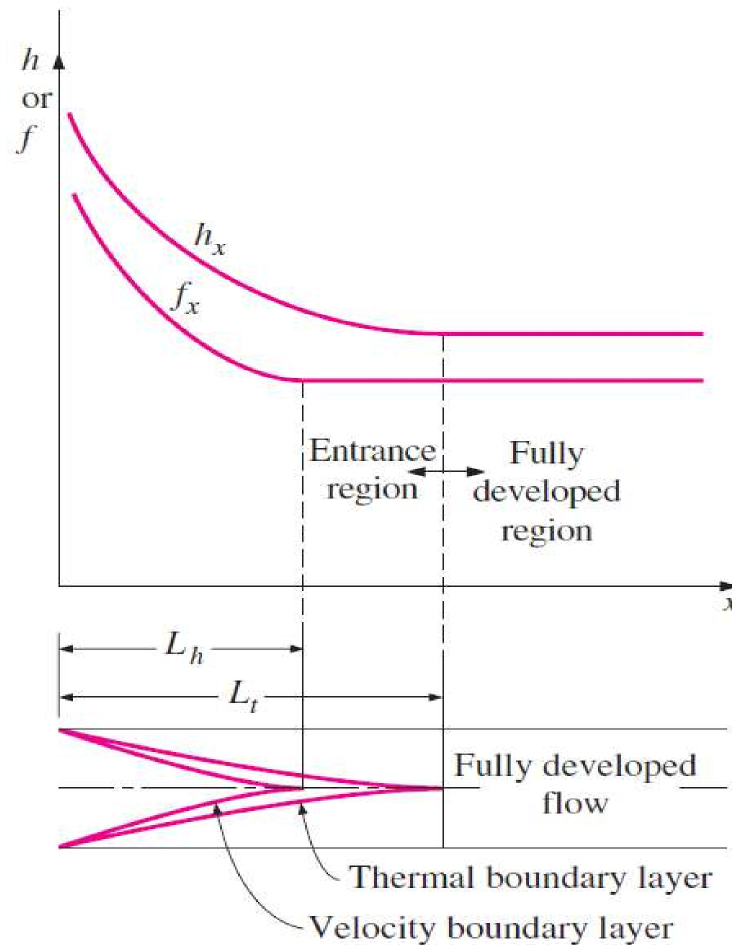

Figure 1.1: Variation of friction factor (f_x) and convective heat transfer coefficient (h_x) in flow direction for flow in tube ($Pr>1$) [1]

1.3.1 Active Techniques

Active techniques require external power to improve heat transfer. These techniques include electro hydrodynamic, spray, mechanical aids, surface vibration, fluid vibration, impingement jet, etc. [3, 4]. Electro hydrodynamic (EHD) enhances heat transfer by combining electric and fluid fields. High voltage and currents are applied to the fluid in this procedure. It converts electrical energy into kinetic energy. Another method for heat transfer enhancement is using jet in between fluid. In the method, high velocity of the fluid is projected to enhance the heat transfer coefficient. Jets are employed in various industrial applications, including thermal control of high flux equipment like electronics, X-rays, optics, gas turbines, and engine cooling. Mechanical aids, such as mechanically rotating the fluid, can improve heat transfer.

Surface vibrations of low or high frequency are utilized to improve single phase heat transfer. In order to improve heat transfer, a piezoelectric device can vibrate a heat transfer surface. Due to the mass of the heat exchangers, fluid vibration is the most feasible type of vibration augmentation, and it is usually used for single phase fluids.

1.3.2 Passive Techniques

Passive techniques improve heat transfer by altering surface exchange or fluid characteristics, modifying surface geometry, and interrupting boundary layers [4]. The main advantage of passive approaches does not need external power source. Coating, etching, directional growth, and other methods of nanoscale structuration modify the chemical and physical properties of surfaces. The heat transfer surface area is unaffected by the nano scale roughness. In particular in phase change conditions, an effect on the heat transfer coefficient can be achieved: an increase in the number of nucleation sites or a change in the wettability of the liquid on the wall can greatly improve heat transmission. Khan *et al.* [5] investigated the use of surface coating to improve pool boiling heat transfer. One of the most effective ways to improve heat transfer is to coat porous metal surfaces. Due to the presence of gas trapped in the coating pores, the nucleation sites are abundant and easily activated. Some other passive techniques include topological modification of heat exchanger, inserting vortex generators, secondary flow have reported positive effect on heat transfer enhancement.

1.3.3 Compound Techniques

Both active and passive approaches sometimes become insufficient to meet the higher heat transfer demand. It combines the benefits of both active and passive techniques.

1.4 Thermal Management of Power Electronics

Overall power and heat flux dissipation have increased dramatically due to the advancement of technology. Thermal management is required in such systems to keep the core temperatures of miniature devices below acceptable limits for better and safe performance. Micro-/Mini-channel heat sinks, jet impingement cooling, phase-change

technologies, thermosiphons, and vapor chambers are all gaining popularity to serve the purpose [6-8].

1.5 Micro-/Mini-channel Heat Sink

With the advancement of modern technology, power electronics are becoming miniature, sophisticated and compact. The demand for heat flux removal is growing as technology evolves. Micro-/Mini-channels can play an essential role in regulating the temperature of electronic devices. In terms of channel hydraulic diameters, micro-/mini-channel heat exchangers differ from conventional heat exchangers. Kandlikar and Grande [9] proposed classifications of micro-/mini-channel based on hydraulic diameter. The type is listed in table 1:

Table 1: Channel classification by Kandlikar and Grande [9]

Channel	Hydraulic Diameter
Conventional HX	$D_h > 3$mm
Mini-channels (MCHS)	200 μm $< D_h \leq 3$ mm
Micro-channels (MiCHS)	10 μm $< D_h \leq 200$ μm
Transitional channels	0.1 μm $< D_h \leq 10$ μm
Molecular nanochannels	$D_h \leq 0.1$ μm

1.6 Motivation of the Present Study

Modern technology is advancing with the passage of time. These modern electronics are made of different types of IC circuits, transistors, etc. The size of the electronic devices is also getting compacted and sophisticated over time. New features and software are introduced in electronic devices. Hence, the performance and power consumption have been boosted up. Figure 1.2 shows data of introducing new features in the Qualcomm Snapdragon processesors. Qualcomm Snapdragon is one of the best processors for the smartphone. Figure 1 shows that the degree of integration after 2008 keeps increasing to meet the demands of (i) higher computational performance (ii) faster wireless connections, and (iii) richer multimedia capabilities [10]. to integrate the new feature to meet the rising demands, the processors are needed to redesign to allow the new features.

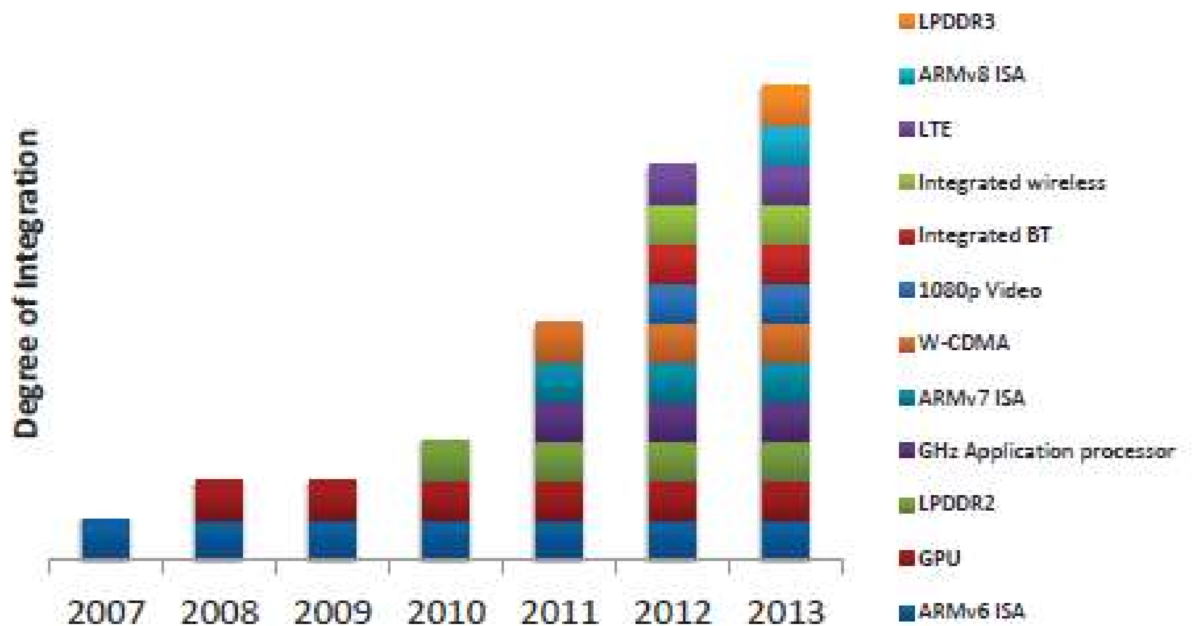

Figure 1.2: Increasing degree of integration in mobile application processor (Qualcomm SnapdragonTH family) [10]

The new processors are getting more compact over time. Apart from the compactness, the processors are consuming more power. Figure 1.3 shows the power consumption scenario of microelectronic devices [11]. The power consumption is increasing over time, and the power consumption curve is in increasing trend. The enhancement of power consumption requires higher heat dissipation from the microelectronic to ensure effective microelectronics performance. Removing heat from microelectronics can reduce power consumption. Liu *et al.* [12] showed that the average heat flux generation in microelectronic was 50 W/cm^2 during operation. Naqiuddin *et al.* [13] predicted that the heat flux generation might reach up to 100 W/cm^2 after 2020.

Therefore, the conventional air cooling method is insufficient for removing the higher demanded heat flux. So, the cooling of microelectronics has introduced a new challenge for researchers. So, many researchers are focused on developing new cooling solutions for the problem. The aim of the thesis is to propose a new type of interconnected mini-channel heat sink with wavy walls for improved cooling solution.

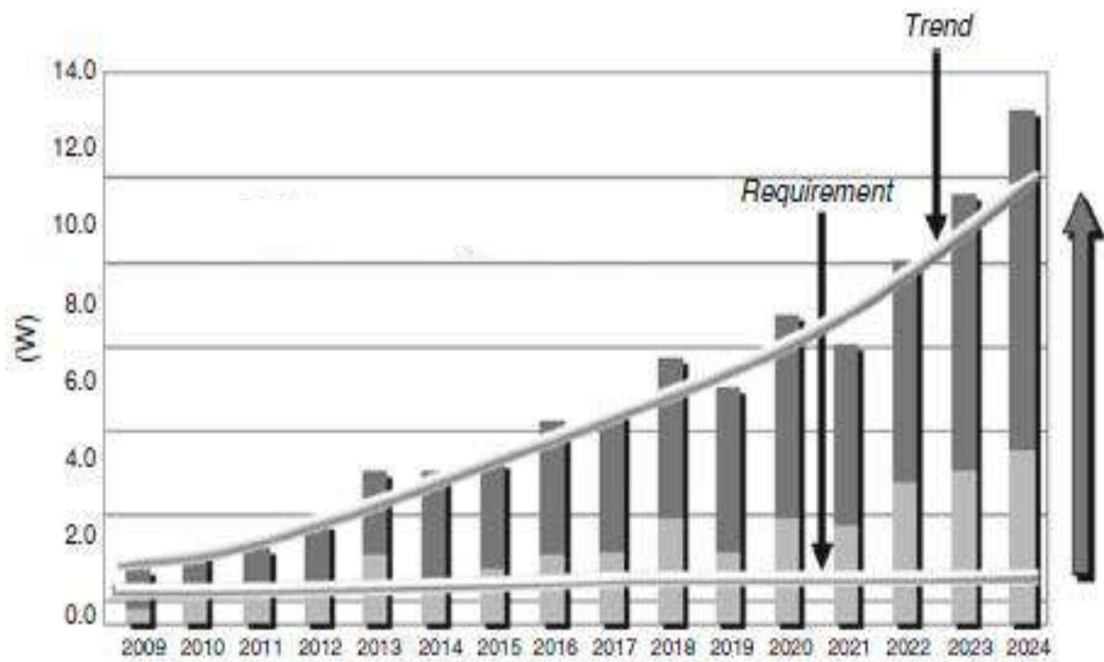

Figure 1.3: Power consumption trend of microelectronics [11]

1.7 Main Objectives of the Thesis

The objectives of the present work can be summarized as follows:

i) To study the fluid flow and heat transfer mechanism in interconnected wavy MCHS.
ii) To study effect of different wavy channel parameters, such as wavelengths, amplitudes and phase shifts, on the thermal and hydraulic performance of interconnected wavy MCHS.
iii) To assess the thermal and hydraulic performance of interconnected wavy MCHS and compare it with the conventional straight MCHS in terms of Nusselt numbers, friction factors, local temperature distributions, and maximum temperatures of the heat sink.

To optimize wavy mini-channel parameters, such as wavelengths, amplitudes and phase shifts, for the best thermal performance of interconnected wavy MCHS.

1.8 Layout of The Thesis

The study presented in this dissertation has addressed "Performance Analysis of An Interconnected Mini-Channel Heat Sink with Wavy Wall". The dissertation has been organized as follows. In chapter 1, a general discussion on heat transfer, thermal cooling techniques, and objectives of the dissertation are discussed. In chapter 2, a detail literature review. In chapter 3, numerical modeling, numerical boundary conditions have been discussed. In chapter 4, model validation and analysis of the numerical solution have been discussed. In chapter 5, conclusion has been drawn.

CHAPTER 2: LITERATURE REVIEW

2.1 Introduction

With the advancement of technology, the size of modern electronics is constantly shrinking whereas power density is increasing constantly which makestraditional heat extraction techniques insufficient for further development of theses electronics devices. Numerous researchers have focused to developed new techniques for developing effective cooling solutions for these devices. Liquid cooling with a micro/mini-channel posses a promising solution. This chapter reviews current research of micro/mini-channel heat sink.

2.2 Existing Literature on Micro-channel and Mini-Channel Heat Sink

The concept of a microchannel heat sink (MiCHS) was proposed by Tuckerman and Pease [14] to remove significant amounts of heat from a compact and small location, such as microelectronic devices. They claimed that the MiCHS has a higher heat transfer coefficient because of its smaller hydraulic diameter. Phillis [15] investigated the thermo-hydraulic performance of MiCHS both experimentally and numerically. MiCHS has a higher pressure drop penalty than conventional heat sinks, providing superior cooling performance [16]. For practical applications, mini-channel heat sinks (MCHS) are an excellent alternative to MiCHSs, as they provide a high heat transfer coefficient with a lower pumping power penalty than MiCHSs. Channels with hydraulic diameters ranging from 200 μm to 3 mm are referred to as MCHSs [17]. Dang *et al.* [18] used numerical and experimental methods to investigate the thermal performance and required pumping power of MCHSs. They came to a conclusion that, because it requires less pumping power, an MCHS could be a feasible alternative to a MiCHS.

Furthermore, most researchers concluded that traditional MCHSs' reduced pumping power requirement is offset by a thicker thermal boundary layer, resulting in poor thermal performance compared to MiCHSs. Enhanced heat transfer performance can be achieved with low pumping power by interrupting and reinitializing the thermal boundary layer in MCHSs [19, 20].

2.3 Heat Transfer Enhancement by Geometry Modification

According to conventional theory, Nusselt number (*Nu*) is constant in the laminar region for internal flow through channels [1, 2]. Kandlikar *et al.* [21] reported many heat transfer augmentation approaches for MiCHSs/MCHSs, including surface roughness, geometric alteration, and channel curvature. These techniques interrupt the thermal boundary layer to enhance heat transfer. In laminar flow, Saad *et al.* [22] knurled the bottom surface of the MiCHS to disrupt the thermal and hydraulic boundary layers. The authors reported a maximum *255%* increase in Nusselt number and a *360%* increase in friction factors for the enhanced heat sink. A considerable effect of roughness height on the pressure drop and heat transfer characteristics of a trapezoidal silicon MiCHS was discovered by Wu *et al.* [23]. Zhang *et al.* [24] investigated the heat transfer performance of circular channels with zigzag geometry. They found that chaotic advection due to zigzag geometry enhanced the thermal performance compared to straight MiCHS. Chai *et al.* [25] designed a novel interrupted MiCHS with varied geometries and a transverse micro-chamber to optimize heat transfer performance by interrupting boundary layers. According to the authors, heat transfer and pumping power requirements increased significantly. Chai *et al.* [26] also investigated the influence of the MiCHS's periodic expansion-constriction cross-section on overall thermal-hydraulic performance experimentally and numerically. They reported 1.8 times enhancement in *Nu* compared to the conventional MiCHS but pumping power requirements increases significantly. Several other research studies [27-30] also reported similar results .

2.4 Heat Transfer Enhancement by Waviness

The improvement of thermal performance of MCHS is a challenging issue for meeting the increased heat removal demand from the miniature devices. Researchers are proposing various teechniques to improve the thermal performance of MCHS with a little pressure drop penalty. Sui *et al.* [31] proposed a wavy microchannel as an alternative to a straight microchannel. According to the Authors, a wavy microchannel with the same cross-sectional area and a slight increase in pressure drop could provide better thermal performance. Afterwards, different researchers conducted research to determine the best cooling performance of wavy MCHS [32-34]. The heat transfer

was reported to be increased by all the researchers due to the thinning of the boundary layers, secondary flow, vorticity, and convective impact. The thermal-hydraulic performance of a wavy microchannel is affected by geometric characteristics such as wavelength and wave amplitude [35-38]. For example, Sakanova *et al.* [37] claimed that higher wave amplitude and shorter wavelength, results in improved cooling performance of a wavy MCHS. Gong *et al.* [39] studied the thermal properties of wavy MCHS with phase shifts (θ) of π and *0*, and reported that heat transfer in $\theta = \pi$ is better than in $\theta = 0$ for the same Re. The Authors also performed experiments with different wavelengths and amplitudes in the study. They found that higher thermal performance is achieved at the expense of higher pressure drop for shorter wavelengths and higher amplitudes. The effect of increased surface area owing to wavy passage on thermal enhancement was determined to be minor, and no vortices were seen in their research. Finally, they concluded that the improvement in the thermal performance of wavy microchannels is due to the thinning of the thermal boundary layer. Due to the thinner thermal boundary layers, thermal performance of a wavy MCHS is increased by *26%* compared to that of a straight MCHS[36]. For various wave amplitudes and wavelengths, Khoshvaght-Aliabadi *et al.* [40] numerically analyzed the thermo-hydraulic performance of counter and co-current flow in wavy MCHS. The authors claimed that wavy MCHS enhances heat transfer and reduces junction temperature regardless of flow direction while suffering a higher pressure drop penalty than straight mini-channels.

Vertical gas-liquid flow in sinusoidal wavy channels was explored by Nilpueng and Wongwises [41]. Three sinusoidal phase shifts of 0°, 90°, and 180° were used in the study. The findings of the experiments revealed that the phase shifts in wavy wall have great effect in flow pattern and pressure drop. As the phase shifts rise from 0° to 180°, the areas of the bubbly flow pattern and the dispersed bubbly flow pattern grow larger. Nilpueng *et al.* [42] also studied crosscutting wavy plate-fin heat sink with phase shifts of 0° to 180°. The results showed that this approach can improve heat sink's thermal performance roughly *5.9%–19.1%* for a phase shift of 180°.

2.5 Heat Transfer Enhancement by Secondary Flow

In fluid dynamics, fluid flow can be of primary flow and secondary flow. The adverse pressure gradient can cause secondary flow, which interrupts the boundary layer. Heat transfer can be enhanced by the secondary flow, which is a passive heat transfer enhancement technique. Kuppusamy *et al.* [26] used slanted passages in the alternate direction to facilitate secondary flow and quantitatively investigated their influence on the overall thermo-hydraulic performance of MiCHS. The combined effect of flow mixing and thermal boundary layer regeneration improved overall performance of the redesigned MiCHS by *146%* while reducing pressure drop by *6%.* Lee *et al.* [43] proposed the idea of oblique fin to generate secondary flow between two parallel streams. Following that, they also conducted numerous experimental and numerical studies [44-46] to investigate the effect of the oblique fin on thermal-hydraulic performance. They found that the oblique fin outperformed the conventional MiCHS/MCHS because the thermal boundary layer was reinitialized at the leading edge of each oblique fin. To allow cross-channel mixing, Chiam *et al.* [47] built a wavy MiCHS with alternating secondary branches. The authors came to the conclusion that secondary branches and short-wave amplitude gave a superior thermal performance without pressure drop tradeoff. Tikader *et al.* [48, 49] conducted numerical and experimental research with interconnected mini-channels to improve thermal performance without increasing pumping requirements by employing a boundary layer redeveloping concept. The secondary flow resulted in flow separation, recirculation, and reattachment in MCHS owing to the interconnectors in counterflow mode. As a result, the boundary layers were disrupted and reinitialized. The Authors claimed that Nusselt number increased by *45%* while friction factor decreased by 30% for an interconnector width of *1.5 mm* and interconnector location at *6.5 mm* from the inlet at *Re 1044*. The cumulative effect of the rectangular rib, secondary channel, and triangular cavity on the performance of the MiCHS was numerically studied by Japar *et al.* [50], who claimed outstanding overall performance owing to the shared effect of flow mixing and boundary layer disruption.

Several studies have been conducted previously for improving thermal performance of a minichannel heat sink. Interconnected channel and wavy channel both have been reported to increase thermal performance of the heat sink. However, a combined effect

of these two techniques can enhance performance of the channel further. In this study, a new minichannnel heat sink design has been proposed with wavy wall and interconnetors between channel. No study has been reported yet about this study.

2.6 Summary

Disrupting boundary layer and secondary flow are one of passive heat transfer enhnancement techniques. The conventional straight mini-channel promotes the continual growth of the boundary layer thickness in the channel. However, this continuous expansion of boundary layer thickness can be disturbed by introducing waviness in the MCHS. Heat transfer and pumping power are both enhanced as an outcome. Adding secondary flow into the mini-channel can mitigate the adverse effects of increased pumping power. By dint of adding interconnectors (IC) in mini-channel, the benefit of the secondary flow can be achieved successfully if there is a pressure difference across the ICs. Counterflow in IC min-channel allows cross-flow between the channels due to pressure difference across ICs and disrupts the continuous expansion of boundary layer thickness in the mini-channel [48, 49].

Moreover, cross flow brings up with flow separation, recirculation, and reattachment. As a result, the MCHS's thermal and hydraulic performance improves. This research aims to investigate how the thermal and hydraulic characteristics of wavy mini-channel heat sinks (MCHS) with interconnectors respond in wave amplitudes, wavelengths, and wave phase shifts variations.

CHAPTER 3: NUMERICAL MODELLING

A problem can be solved either experimentally, analytically or numerically. The experimental procedure can be expensive and time-consumingwhereas the numerical solution can give a better insight into any problems quickly. When the equations and the physical problems are complicated, the numerical method is preferable over the analytical process. This chapter describes the numerical procedure, geometry modeling, meshing, and mathematical modeling adopted for this study.

3.1 Computational Fluid Dynamics

Computational Fluid Dynamics (CFD) is a discipline of fluid mechanics that analyzes and solves problems involving fluid flows using numerical analysis and data structures. Computers are utilized to execute the computations required to simulate the fluid's free-stream flow and the fluid's interaction with surfaces defined by boundary conditions. The Navier–Stokes equations, which describe numerous single-phase (gas or liquid, but not both) fluid flows, are the foundation of practically all CFD problems. The Euler equations can be obtained by omitting the viscosity elements from these equations, and the entire potential equations can be obtained by omitting the vorticity terms. CFD uses mathematical modeling, numerical methods, discretization and solution approaches, and software tools with solvers and pre-processing and post-processing utilities to provide a qualitative and even quantitative prediction of fluid flows.

There are many different numerical solution procedures, but the finite difference, finite element, finite volume, and spectral element approaches are the most widely used. All of these methods can be used to arrive at a numerical solution. However, using the right method can reduce computation time and improve numerical accuracy. Although Finite Element Methods have several limitations, modern techniques are used to address these drawbacks and maintain numerical inaccuracy to a minimum.

3.2 Ansys FLUENT

Computational fluid dynamics simulation can be helpful in many engineering applications, and Ansys FLUENT software [51] can be a vital tool for solving complex CFD-related problems. Ansys FLUENT software contains the broad physical modeling capabilities needed to model flow, turbulence, heat transfer, and reactions. Many industrial applications, from air flow over an aircraft wing to combustion in a furnace, bubble columns to oil platforms, blood flow to semiconductor manufacturing, and cleanroom design to wastewater treatment plants, can be solved reliably with Ansys FLUENT. Ansys FLUENT software includes CAD modeling, meshing, solver, and post-processing. Furthermore, to customize the solution of any unique and complicated problem, user-defined functions (UDF) can be used in the software. Ansys FLUENT is a frequently used CFD solver because of its quick, exact solutions and user-friendly interface.

3.3 Mathematical Modeling 2D Wavy MCHS (w-MCHS)

The essential parameters of w-MCHS are wavelength (W_L), wave amplitude (W_A), and wave phase shift (θ_p). Most of the studies related to w-MCHS are focused on the effect of wavelength and wave amplitude [31, 32, 37]. A 2D numerical model is studied in the current research to understand the effect of phase shift in fluid flow and heat transfer characteristics.

3.3.1 Geometry of 2D w-MCHS

A two-dimensional w-MCHS, as shown in fig. 3.1(a) – 3.1(b), with a length of L=700 mm, and a height of $H=1.5$ *mm*, has been modeled for the numerical analysis. Wave amplitude, $W_A=0.4$ *mm* is constant in the study for understanding the effect of phase shift only. Three distinct wavelengths, $W_L=14$ *mm*, *7 mm*, and *3.5 mm*, as well as three different phase shifts, $\theta_p=0$, π/2, π between the upper and bottom boundary layers of the wavy w-MCHS, are investigated. The length of the wavy MiCHS is chosen at *700 mm* to ensure thermally and hydrodynamically fully developed flow in the w-MCHS. The heat transfer coefficient, Nusselt number, friction factor becomes constant in the fully developed region of MCHS. The enhancement of heat transfer can be possible by redevelopment and interruption of boundary layers. Table 2 illustrates the geometric dimensions in detail. *Case 0* is a straight MCHS (s-MCHS), while cases 1-

case 9 are 2D w-MCHS for different W_L and θ_p. All of the cases in table 2 have the same length, height, and W_A.

Table 2: Case-specific 2D w-MCHS

Case no	W_L (*mm*)	θ_p
0	-----	-----
1		*0*
2	*14*	*π/2*
3		*Π*
4		*0*
5	*7*	*π/2*
6		*Π*
7		*0*
8	*3.5*	*π/2*
9		*Π*

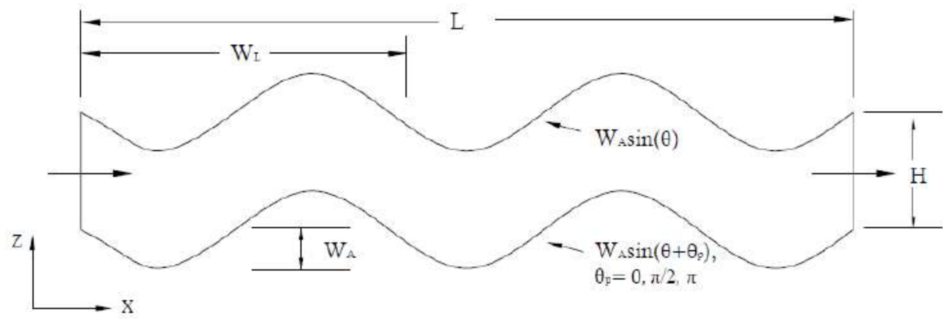

(a)

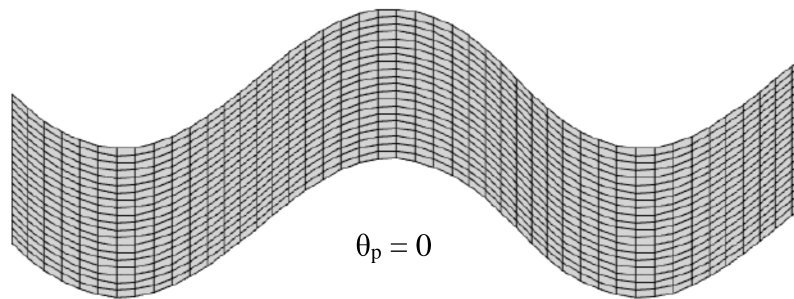

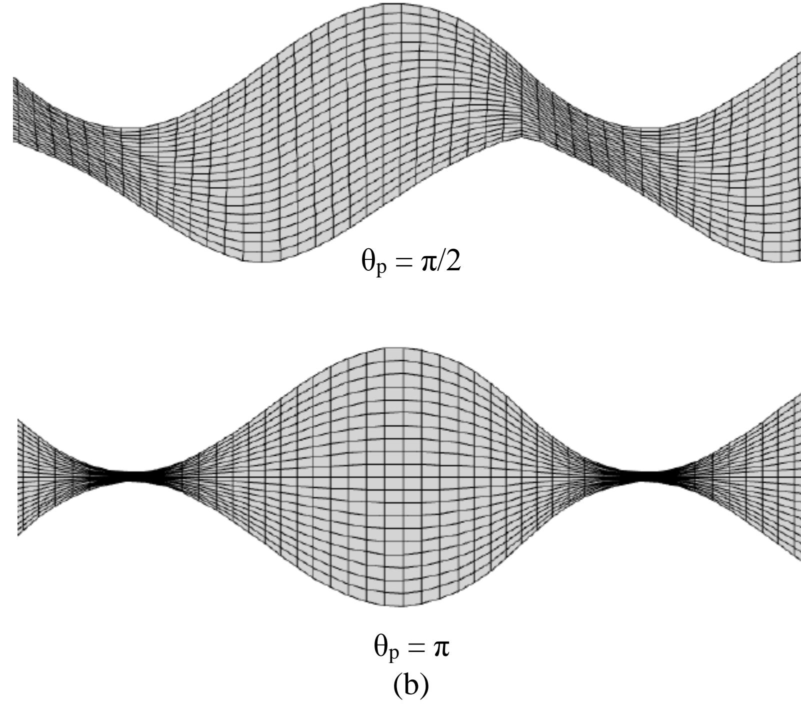

Figure 3.1: The schematics of (a) w-MCHS and (b) its mesh for different phase shifts

3.3.2 Mesh Independence Test

The grid independence test has been performed to optimize the solution accuracy with minimum computational cost. For the grid-independence test, *Nu* and *f* are evaluated for *case 1* at *Re 700*. Three distinct mesh numbers has been selected as shown in table 3, and the deviation between mesh 2 and mesh 3 is less than *1%*. The mesh 2 is chosen for the present study due to less computational time than mesh 3 (90000). In addition, mesh 2 also shows better accuracy than mesh 1.

Table 3: Grid independent test for 2D w-MCHS

Sl. no.		Mesh no	*Nu*	*f*
Mesh 1		*30000*	*9.25*	*.044*
Mesh 2	*Case 1*	*60000*	*8.99*	*0.0443*
Mesh 3		*90000*	*8.91*	*0.045*

3.3.3 Governing Equations

A two-dimensional wavy microchannel heat sink model is used to study the thermal performance. The assumptions that are employed are as follows:

(1) incompressible, laminar, and steady-state flow.

(2) constant fluid properties; neglected gravitational force and viscous dissipation.

(3) neglected heat losses between the ambient and the heat sink.

The governing equations for flow and heat transfer can be written based on the adopted assumptions.

The finite volume method is used to solve continuity, momentum, and energy equations:

$$\frac{\partial(\rho u)}{\partial x}+\frac{\partial(\rho v)}{\partial y}=0 \tag{3.1}$$

$$u\frac{\partial u}{\partial x}+v\frac{\partial u}{\partial y}= -\frac{1}{\rho}\frac{\partial p}{\partial x}+\frac{\mu}{\rho}(\frac{\partial^2 u}{\partial x^2}+\frac{\partial^2 u}{\partial y^2}) \tag{3.2a}$$

$$u\frac{\partial v}{\partial x}+v\frac{\partial v}{\partial y}= -\frac{1}{\rho}\frac{\partial p}{\partial y}+\frac{\mu}{\rho}(\frac{\partial^2 v}{\partial x^2}+\frac{\partial^2 v}{\partial y^2}) \tag{3.2b}$$

$$u\frac{\partial T}{\partial x}+v\frac{\partial T}{\partial y}= \alpha(\frac{\partial^2 T}{\partial x^2}+\frac{\partial^2 T}{\partial y^2}) \tag{3.3}$$

3.3.4 Boundary Conditions

At the inlet of the w-MCHS, a uniform mass flow rate of fluid has specified for numerical simulation. T_{inlet} is *300K* for the coolant temperature at the inlet. A constant heat flux of $q''=1.5\ W/cm^2$ is applied in both walls of w-MCHS. For all cases in Table 2, the Reynolds number (*Re*) is varied between *150* and *800*. In the MCHS, no-slip boundary condition is applied to the walls. The followings are the hydrodynamic boundary conditions adopted for this study.

Inlet: at $x= 0$, $u= m_{in}$ and $T_{inlet} = 300\ K$, $v= 0$, $w= 0$.

Outlet: at $x= L$, $P_{outlet}= 0$.

Ansys FLUENT® is utilized to solve the governing equations for velocity, pressure, and temperature fields simultaneously with appropriate boundary conditions. For the numerical solution, the SIMPLE scheme and second-order upwind are used to solve the governing equations with a convergence criterion of 10^{-6}. Under-relaxation factors are chosen as *0.7, 1, 0.3, 1,* and *1* for momentum, density, pressure, energy, and body forces, respectively.

3.3.4 Data Analysis

This study has used the numerical solution to calculate wall temperature, coolant velocity, coolant temperature at the microchannel outlet, and pressure drop through the microchannel. To evaluate the thermal-hydraulic performance of the wavy microchannel, Nusselt number (*Nu*), Reynolds number (*Re*), and friction factor (*f*) are salient non-dimensional parameters. The performance of the wavy microchannel is predicted using these factors.

$$h = \frac{q''_{eff}}{T_s - T_m} \tag{3.4}$$

$$Nu = \frac{h\,H}{K} \tag{3.5}$$

where *h, k* and *H* are average heat transfer coefficient, fluid thermal conductivity, and height of the channel, respectively. T_s is the area-weighted average wall temperature, and T_o is the mass-weighted average outlet temperature of the wavy microchannel. $T_m = \frac{T_{in}+T_o}{2}$ is the mass-weighted bulk fluid temperature.

Re and f are evaluated using the following equations:

$$Re = \frac{\rho v H}{\mu} \tag{3.6}$$

$$f = -\frac{2\,H\,\Delta P}{\rho L\,v^2} \tag{3.7}$$

Where, ρ, *v*, μ and ΔP are density, velocity, viscosity and pressure drop respectively.

$$\Delta P = P_{outlet} - P_{inlet} \tag{3.8}$$

To compare the thermo-hydraulic performance of w-MCHS with s-MCHS, performance evaluation criteria (*PEC*) is calculated [7, 48, 49].

3.4 Mathematical Modeling 3D Wavy MCHS with Interconnectors (IC w-MCHS)

Heat transfer enhancement by modifying the geometry of MCHS causes higher pressure drop. Similarly, as previously indicated in the literature, introducing waviness to a mini-channel improves heat transfer at the expense of increased pressure drop [31, 37]. In addition, secondary flow in MCHS improved the thermo-hydraulic performance of straight mini-channels with interconnectors [48, 49]. Therefore, a wavy mini-channel with interconnectors can improve heat transfer by breaking and redeveloping thermal boundary layer more than a conventional straight mini-channel. The current research investigates the thermal and hydraulic performance of IC w-MCHS in response to different waviness parameters.

3.4.1 Geometry of 3D IC w-MCHS

The computational domain for the study is a three-dimensional mini-channel, as shown in Figure 3.2. Table 4 shows the detailed dimensions of the computational 3D model. The front, top, and side views of the interconnected wavy mini-channel heat sinks (IC w-MCHS), as well as the primary and secondary flow directions, are shown in Figure 3.2(b)- 3.2(e). Two ICs can divide the flow domain of the channel into three zones. Wave amplitude (W_A), wavelength (W_L), and wave phase shift (θ_p) are the design parameters. To visualize the effect of waviness in interconnected mini-channel heat sinks, location (L_i) and width (W_i) of the ICs have been kept constant in this study. The coolant was chosen as water, and the material of the MCHS was chosen as copper. Table 4 lists all the dimensions and design parameters. Table 5 illustrates different parameters used for this study. Figure 3.3 shows the different schematics of different MCHS.

Table 4: The dimension of IC w-MCHS's parameters

W_i, mm	L_i, mm	L, mm	H, mm	W, mm	W_d, mm	θ_p	W_A, mm	W_L, mm	$\alpha = W_A/H$	$\beta = W_L/L$
						0	.075	1.57	0.15	0.06
1.25	6.5	26	0.5	1.5	1	π	0.1	2.08	0.2	0.08
							0.15	4	0.3	0.15

Table 5: The combination of variable parameters in the study

amplitude ratio, $\alpha = 0.15, 0.2, 0.3$	$\theta_p = 0, \pi$	$\beta = 0.08$
wavelength ratio, $\beta = 0.06, 0.08, 0.15$	$\theta_p = 0, \pi$	$\alpha = 0.2$

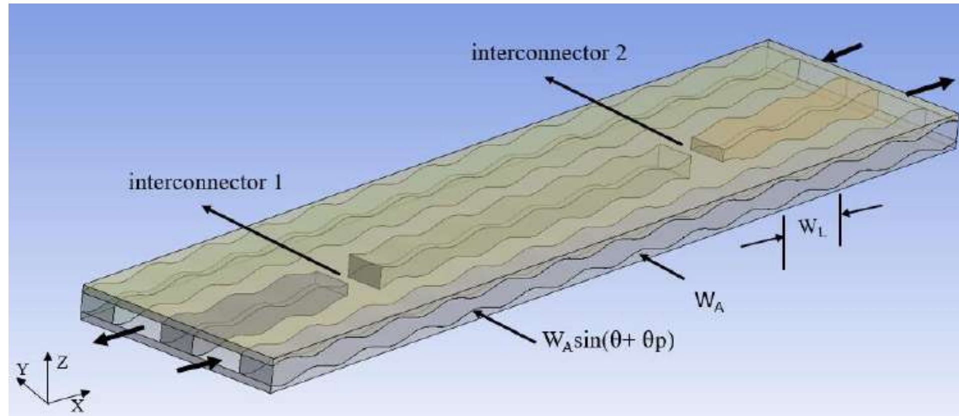

(a)

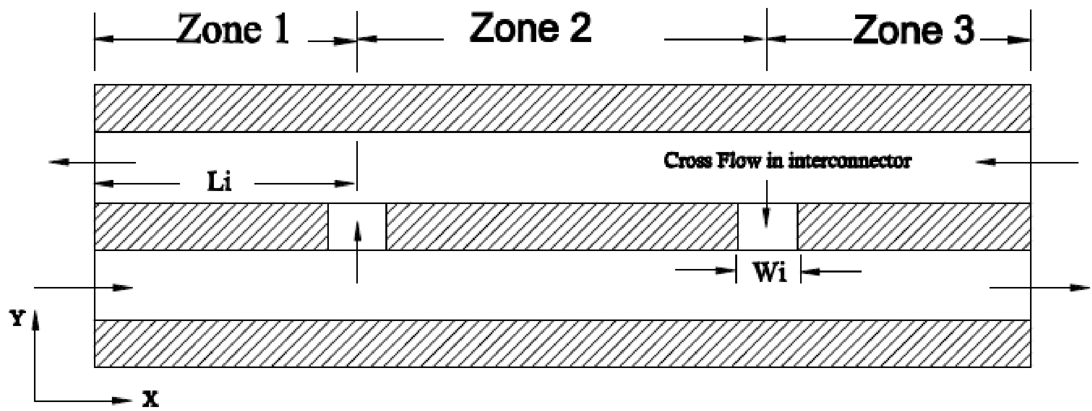

(b)

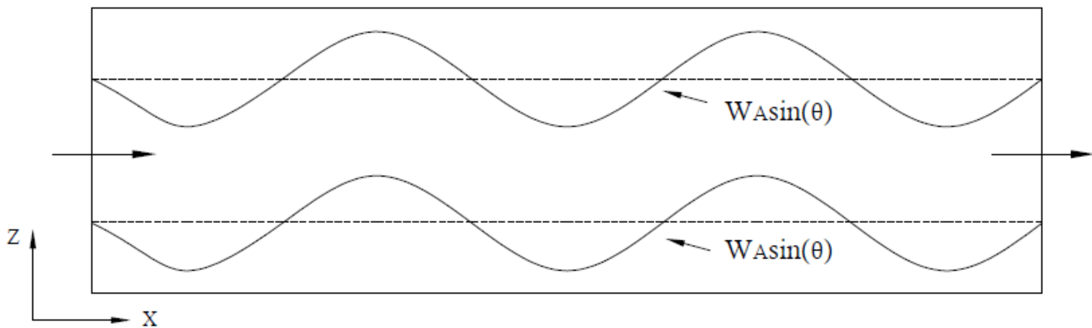

(c)

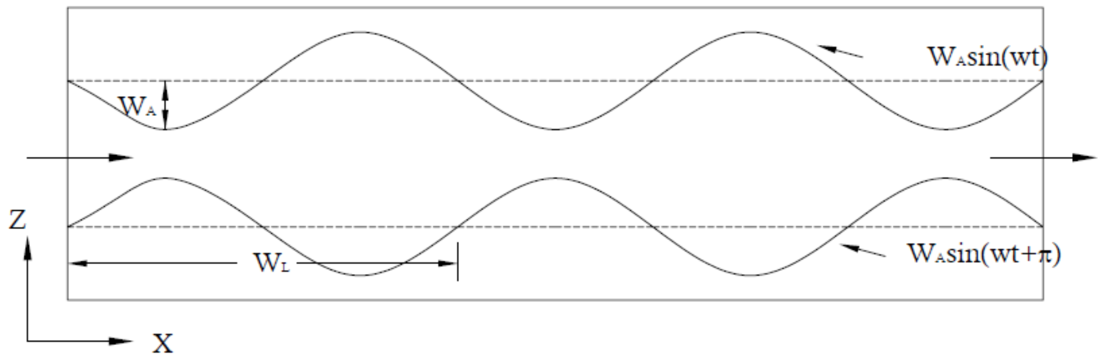

(d)

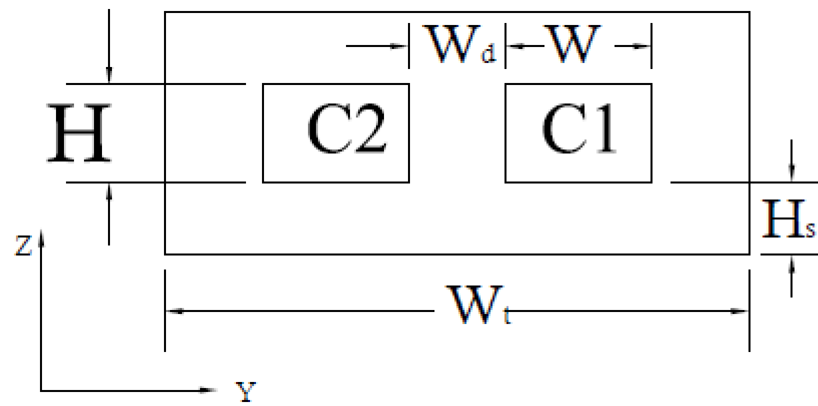

(e)

Figure 3.2: (a) Computational domain of IC w-MCHS (b) Top view of IC w-MCHS at $\theta_p = 0, \pi$ (c) front view of IC w-MCHS at $\theta_p = 0$ (d) front view of IC w-MCHS at $\theta_p = \pi$ (e) left side view of IC w-MCHS, $\theta_p = 0, \pi$

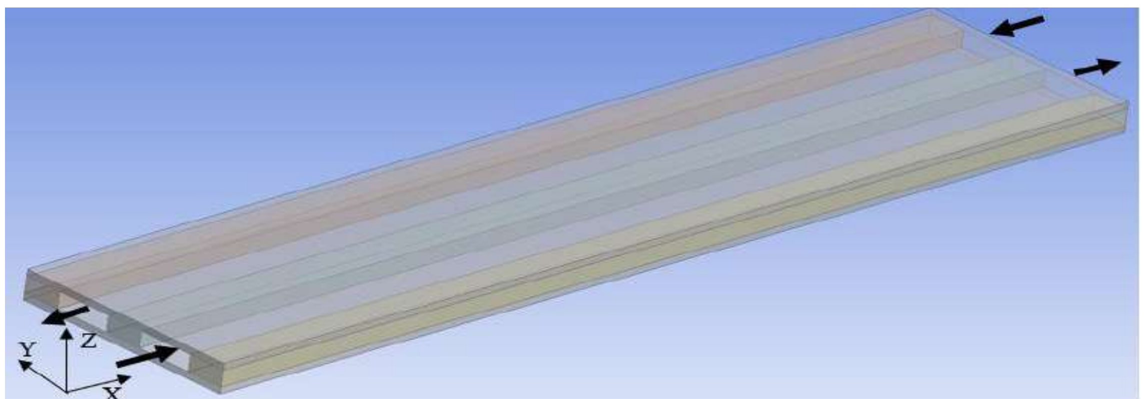

(a)

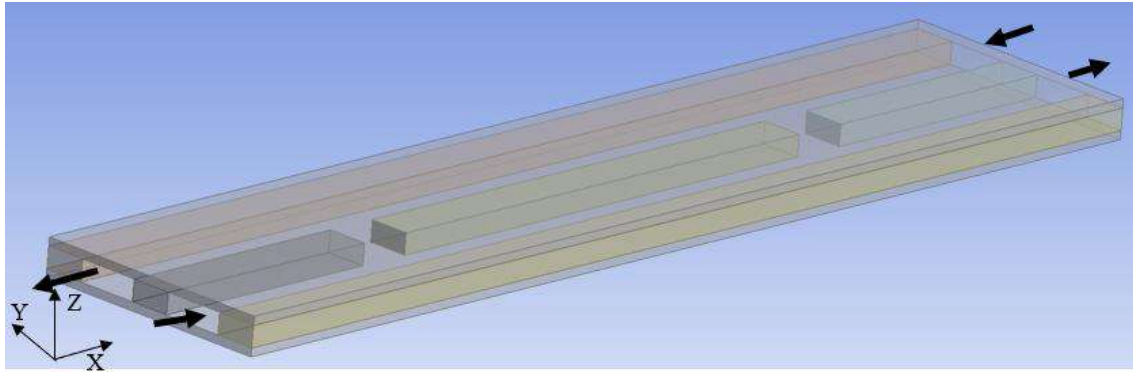

(b)

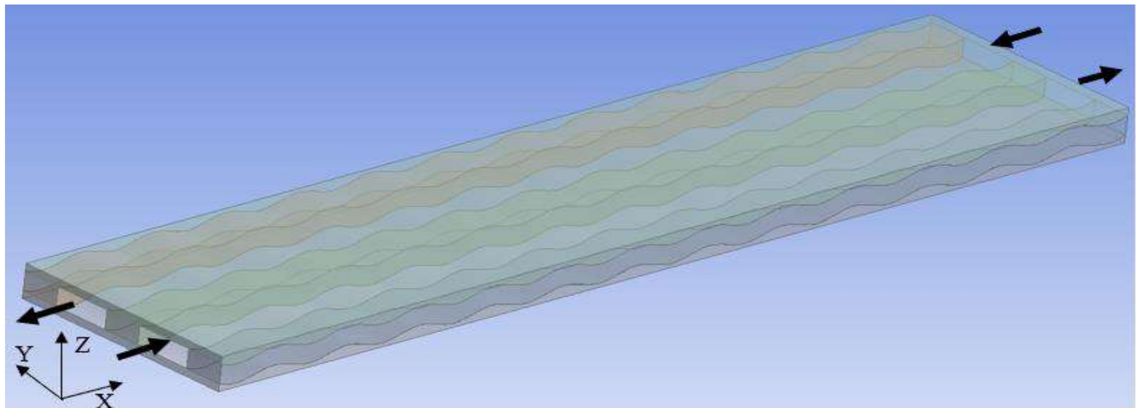

(c)

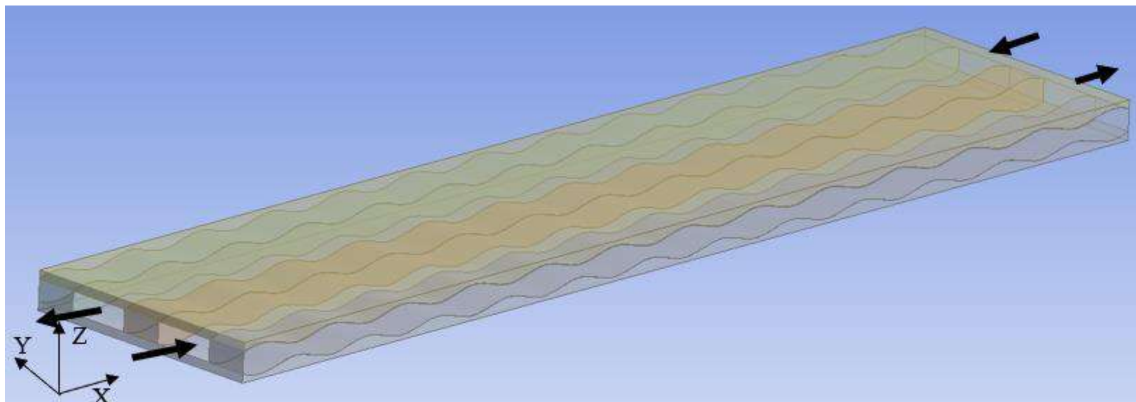

(d)

Figure 3.3: Schematic of (a) conventional mini-channel heat sink (s-MCHS) (b) straight mini-channel heat sink with interconnectors (IC s-MCHS) (c) wavy mini-channel heat sink without interconnectors at $\theta_p = 0$ (w-MCHS, $\theta_p = 0$) (d) wavy mini-channel heat sink without interconnectors at $\theta_p = \pi$ (w-MCHS, $\theta_p = \pi$)

3.4.2 Mesh Independence Test

The structured grid constructs the computational fluid domain used for the simulation. Three different grid systems has been generated for IC w-MCHS for phase shifts, $\theta_p = \pi$ and 0; detailed size of the grids is summarized in Table 6. The grid independence test has been carried out for *Re 550*; *Nu* and *f* are calculated for each of the grid systems. The effect of grid size on the results is presented in Table 6. Almost insignificant differences have been observed for the three grid systems. The error percentage of mesh 2 is an accepted level of less than *1%* compared to mesh 3. Mesh 2 provides the accurate solution with less computational time compared to mesh 3. So, mesh 2 is selected for the numerical simulation. Figure 3.4 shows the meshed computational domains of IC w-MCHS.

Table 6: Grid independent test for 3D IC w-MCHS

Sl. No.		Mesh no	*Nu*	*f*
Mesh 1	*IC w-MCHS,*	*837900*	*15.71*	*.315*
Mesh 2	$\theta_p = \pi$,	*1019200*	*15.51*	*0.316*
Mesh 3	$\alpha=0.2, \beta=0.06$	*1565300*	*15.46*	*0.317*
Mesh 1	*IC w-MCHS,*	*796700*	*12.46*	*0.191*
Mesh 2	$\theta_p = 0$,	*998000*	*12.41*	*0.192*
Mesh 3	$\alpha=0.2, \beta=0.06$	*1524400*	*12.38*	*0.194*

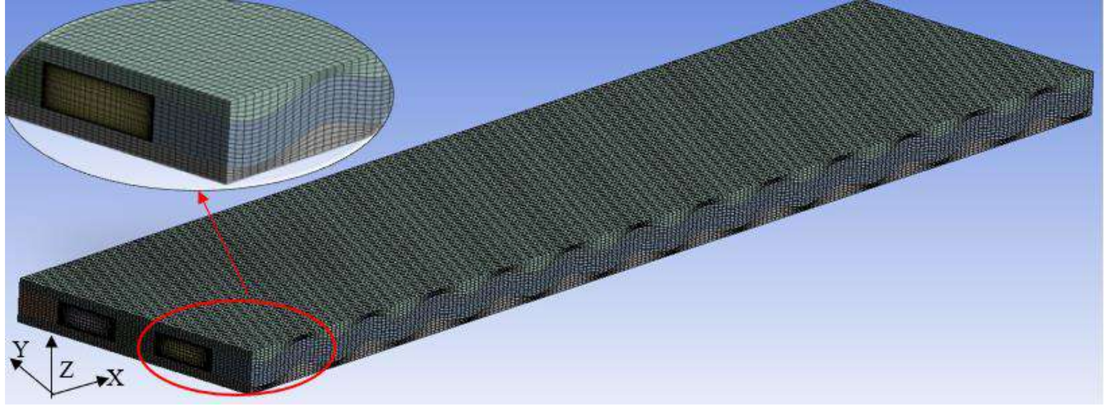

(a)

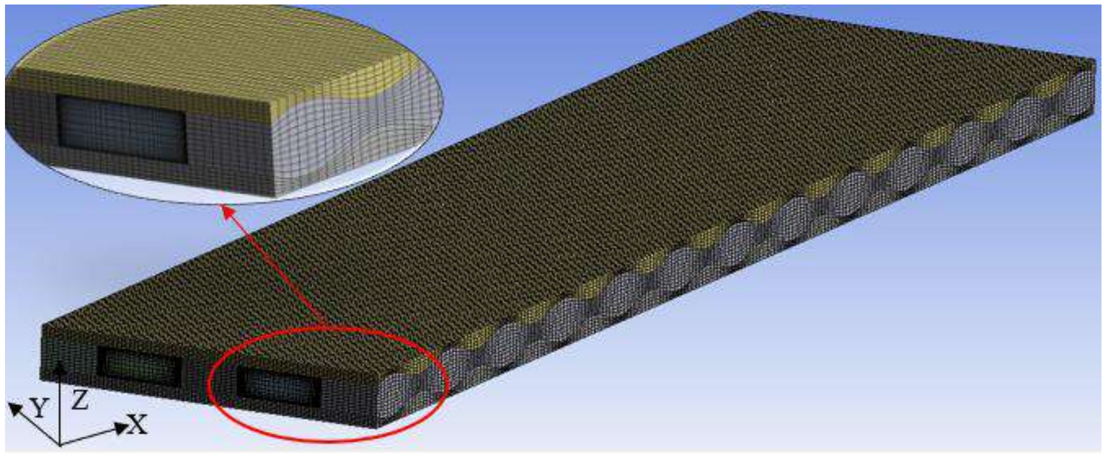

(b)

Figure 3.4: Meshed computational domain of (a) IC w-MCHS, $\theta_p = 0$ (b) IC w-MCHS, $\theta_p = \pi$

3.4.3 Governing Equations

To derive the simplified governing equation for conjugate heat and mass transfer in the MCHS, some important assumptions are considered. The fluid flow is laminar. Thus, *Re* is varied from *300* to *800* for this study. Water is used as coolant in the study and its thermal properties are considered constant. Furthermore, the dimension of the MCHS is small enough to have less buoyancy and gravitational force effect.

According to the above assumptions, the continuity, momentum, and energy equations for the fluid domain can be written as follows:

$$\frac{\partial(u)}{\partial x}+\frac{\partial(v)}{\partial y}+\frac{\partial(w)}{\partial z}=0 \tag{3.9}$$

$$u\frac{\partial u}{\partial x}+v\frac{\partial u}{\partial y}+w\frac{\partial u}{\partial z}= -\frac{1}{\rho}\frac{\partial p}{\partial x}+\frac{\mu}{\rho}(\frac{\partial^2 u}{\partial x^2}+\frac{\partial^2 u}{\partial y^2}+\frac{\partial^2 u}{\partial z^2}) \quad (3.10a)$$

$$u\frac{\partial v}{\partial x}+v\frac{\partial v}{\partial y}+w\frac{\partial v}{\partial z}= -\frac{1}{\rho}\frac{\partial p}{\partial y}+\frac{\mu}{\rho}\left(\frac{\partial^2 v}{\partial x^2}+\frac{\partial^2 v}{\partial y^2}+\frac{\partial^2 v}{\partial z^2}\right) \quad (3.10b)$$

$$u\frac{\partial w}{\partial x}+v\frac{\partial w}{\partial y}+w\frac{\partial w}{\partial z}= -\frac{1}{\rho}\frac{\partial p}{\partial z}+\frac{\mu}{\rho}(\frac{\partial^2 w}{\partial x^2}+\frac{\partial^2 w}{\partial y^2}+\frac{\partial^2 w}{\partial z^2}) \quad (3.10c)$$

$$u\frac{\partial T_f}{\partial x}+v\frac{\partial T_f}{\partial y}+w\frac{\partial T_f}{\partial z}= \alpha\left(\frac{\partial^2 T_f}{\partial x^2}+\frac{\partial^2 T_f}{\partial y^2}+\frac{\partial^2 T_f}{\partial z^2}\right) \quad (3.11)$$

Whereas energy equation for the solid region can be expressed as follows:

$$K_{sol}\left(\frac{\partial^2 T_{sol}}{\partial x^2}+\frac{\partial^2 T_{sol}}{\partial y^2}+\frac{\partial^2 T_{sol}}{\partial z^2}\right)=0 \quad (3.12)$$

3.4.4 Boundary Conditions

For numerical simulation, uniform inlet velocity of fluid is specified. The inlet temperature of fluid, T_{in} is *300 K*. Constant heat flux $q''= 32\ W/cm^2$ is applied at the bottom of the MCHS. No slip boundary conditions are applied on the inner walls of the MCHS. The hydrodynamic boundary conditions are as follows:

Inlet: $x= 0$, $u= V_{in}$ and $T_{in} = 300\ K$, $v= 0$, $w= 0$.

Outlet: $x= L$, $P_{out} = 0$.

Ansys FLUENT® has utilized to solve the governing equations for velocity, pressure, and temperature fields simultaneously with appropriate boundary conditions. For the numerical solution, the SIMPLE scheme and second-order upwind are used to solve the governing equations with a convergence criterion of 10^{-6}. Under-relaxation factors were chosen as *0.7, 1, 0.3, 1,* and *1* for momentum, density, pressure, energy, and body forces, respectively.

3.4.4 Data Analysis

To evaluate thermo-hydraulic performance of the w-MCHS, Nusselt number (*Nu*), Reynolds number (*Re*), friction factor (*f*) are salient non-dimensional parameters. The performance of the wavy microchannel is predicted using these factors.

$$h=\frac{q''_{eff}}{T_w-T_m} \quad (3.13)$$

$$Nu = \frac{h\, D_h}{K_f} \quad (3.14)$$

$$D_h = \frac{2WH}{W + H} \quad (3.15)$$

where $q"_{eff}$, h, k and D_h are the heat flux at the solid liquid interface, average heat transfer coefficient, thermal conductivity of the fluid, and microchannel hydraulic diameter, respectively. T_w is the area-weighted average wall temperature and T_{out} is the outlet temperature of the channels. $T_m = \frac{T_{in}+T_{out}}{2}$ is mass-weighted bulk fluid temperature.

Re and *f* are evaluated using the following equations:

$$Re = \frac{\rho v D_h}{\mu} \quad (3.16)$$

$$f = -\frac{2\, D_h\, \Delta P}{\rho L\, v^2} \quad (3.17)$$

where ρ, v, μ and ΔP are density, velocity, viscosity and pressure drop respectively.

$$\Delta P = P_{outlet} - P_{inlet} \quad (3.18)$$

To compare the thermal-hydraulic performance of w-MCHS with s-MCHS, performance evaluation criteria (*PEC*) is calculated [7, 48, 49]. Positive heat transfer impact above pressure drop penalty is denoted by a *PEC* larger than one.

$$PEC = (\frac{Nu}{Nu_o})(\frac{f}{f_o})^{-\frac{1}{3}} \quad (3.19)$$

CHAPTER 4: RESULTS AND DISCUSSION

The main objective of the present study is to investigate the effect on fluid flow and heat transfer characteristics of interconnected wavy mini-channel. Nusselt numbers, friction factors, local temperature distributions, and pressure and velocity distributions in the IC w-MCHS are evaluated in the laminar regime for different wavelength (W_L), wave amplitudes (W_A), and shift phases (θ_p). The Reynolds number is varied between *300* to *800* for the numerical investigations.

4.1 Model Validation

Validation is the vital process of assessing the accuracy and reliability of the numerical analysis. *Nu* for s-MCHS in parallel flow mode has modeled to validate with the experimental results of Fan *et al.* [46] for *Re* ranging from *150* to *450*, Ho *et al.* [52] for *Re* ranging from *450* to *1044*. The result is also compared with the theoretical result of Shah and London [53] as shown in fig 4.1(a). Nu obtained in the present study is in good agreement with the previous numerical and experimental studies. The correlation developed for thermally developing flow by Shah and London [53] is shown in the following equations:

$$Nu = 1.953\left(\frac{Re\,\mathrm{Pr}\,D_h}{L}\right)^{\frac{1}{3}}; \qquad \frac{RePrD_h}{L} \geq 33.33 \tag{4.20}$$

$$Nu = 4.264 + 0.0722\left(\frac{Re\,\mathrm{Pr}\,D_h}{L}\right); \qquad \frac{RePrD_h}{L} < 33.33 \tag{4.21}$$

In fig 4.1(b), the numerically calculated friction factor for a parallel flow s-MCHS is compared to the generally used Shah and London [20] correlation of friction factor for fully developed and developing flow. The deviation of the friction factor of the present study is less than *4%* compared to Shah and London’s correlation. The correlation of Shah and London is given below:

$$f_{app}(L)Re_{ave,0-L} = \sqrt{\left[\frac{3.2}{(L/D_h\,Re)^{0.57}}\right]^2 + (fRe)_{fd}^2} \tag{4.22}$$

Where$(fRe)_{fd} = 96(1 - 1.3553 \propto +1.9467 \propto^2 - 1.7012 \propto^3 +$
$0.9564 \propto^4 \; 0.2537 \propto^5)$ is applicable only for fully developed laminar flow.

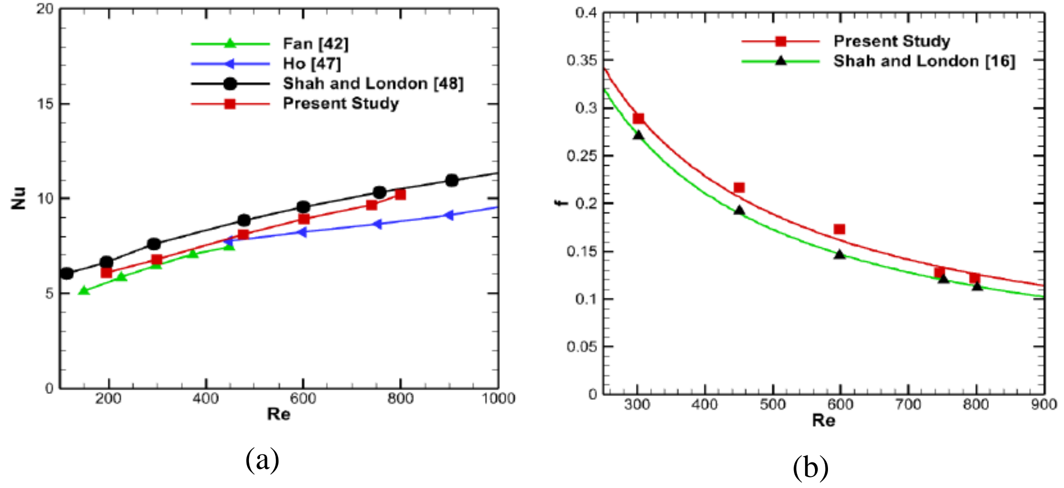

(a) (b)

Figure 4.1: (a) Comparison of *Nu* with Fan *et al.* [46], Ho *et al.* [54], and Shah and London [53] (b) comparison of f with Shah and London [20] correlation for distinct *Re*

Furthermore, *Nu* for 3D straight mini-channel with interconnectors (IC s-MCHS) has evaluated and compared with Tikadar *et al.* [48] for *Re* ranging from *150* to *1044*. For verification, the dimensions of the mini-channels are the same. The interconnector width (*Wi*) is *1.25 mm*, and the location of the interconnector (*Li*) is *6.5 mm* from the inlet. Both *Nu* of the present study and *Nu* of Tikadar [48] follows a similar trend with *Re* as illustrated in fig 4.2 (a), and the maximum deviation is within *2%.*

To improve the reliability of the current numerical study, *Nu* and ΔP of wavy microchannel with the same dimension as Gong *et al.* [39] with four different wavelengths, W_L= *1.3, 2, 2.6,* and *4 mm* and constant amplitude, W_A=*100* μm, and phase shift (θp) = *0,* π at *Re*= *150* have evaluated to compare with the present numerical study, and good agreement (deviation less than *4%*) has found. Figure 4.2 (b) shows the *Nu* and ΔP of Gong *et al.* [39] and the present study.

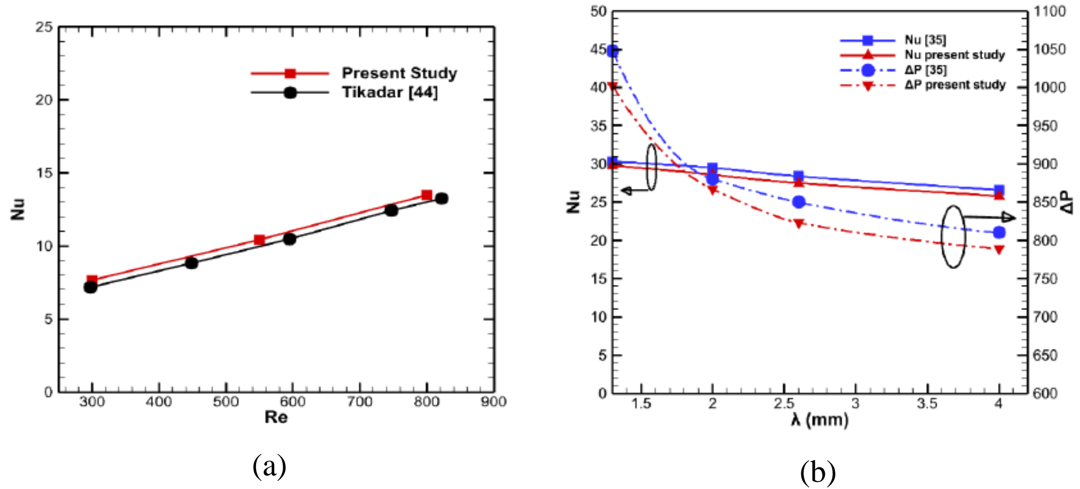

(a) (b)

Figure 4.2: (a) Comparison of *Nu* of interconnected Mini-channel Heat Sink (IC s-MCHS) with Tikadar *et al.* [48] at different *Re*. The maximum deviation was less than *2%* (b) Comparison of *Nu* and ΔP with Gong *et al.* [39] for different wavelengths at *Re=150*.

4.2 Effect of Phase Shift in 2D w-MCHS

In s-MCHS, boundary layers expand uninterruptedly along the flow direction, and *Nu* is constant in the thermally fully developed region for s-MCHS. The introduction of wavy wall, on the other hand, can disrupt and redevelop boundary layers [36, 39]. The wavelength, wave amplitude, and phase shift are vital wavy parameters. The majority of prior studies [31, 35, 38] have concentrated on the effect of wavelengths and wave amplitude on heat transfer and flow characteristics. However, recent investigations on the gas-liquid vertical sinusoidal channel and sinusoidal cross-cut fin by Nilpueng and Wongwises [41, 42] have revealed that phase shift substantially impacts fluid flow and heat transfer characteristics. As a result, the present section will discuss how the phase shift will influence the fluid flow and heat transfer characteristics. Three distinct phase shifts (θ_p= 0, π/2, π) are investigated for 2D w-MCHS to examine the influence of phase shift on wavy MCHS.

Firstly, the flow pattern in 2D w-MCHS will assist in understanding the effect of phase shifts in the improvement of thermal and hydraulic performance. In the case of w-MCHS at θ_p= 0 for W_L= 14 mm (case 1) and W_L = 7 mm (case 4), as shown in fig 4.3 and fig 4.4, vorticity is not visible for case 1 and case 4 at Re 700. At the same Re, w-MCHS at θ_p= π/2, π for W_L = 14 mm (case 2, case 3) and W_L = 7 mm(case 5, case 6)

show intensive flow reversal. The flow reversal and intensive chaotic advection cause better mixing of the coolant. Hence, heat transfer and pressure drop enhance in w-MCHS.

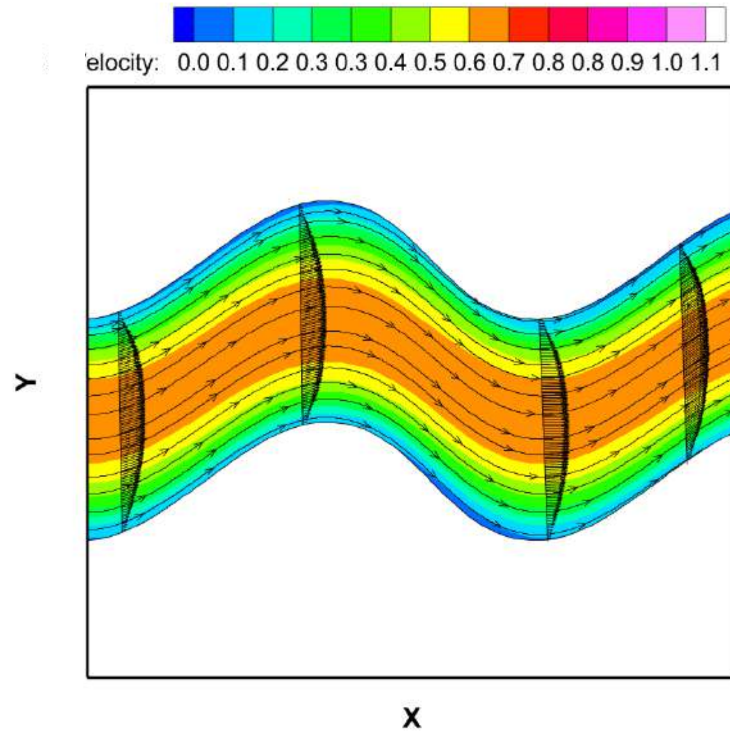

(a)

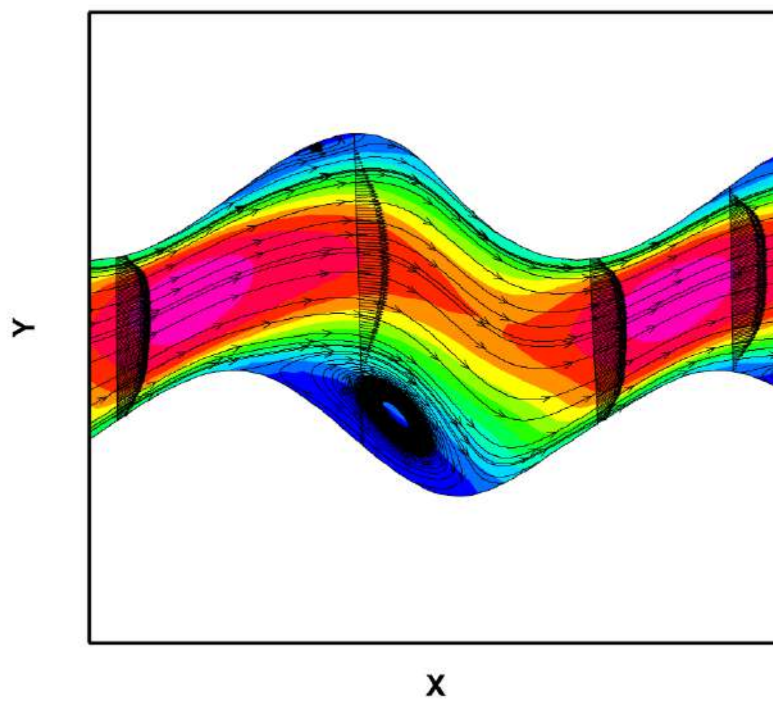

(b)

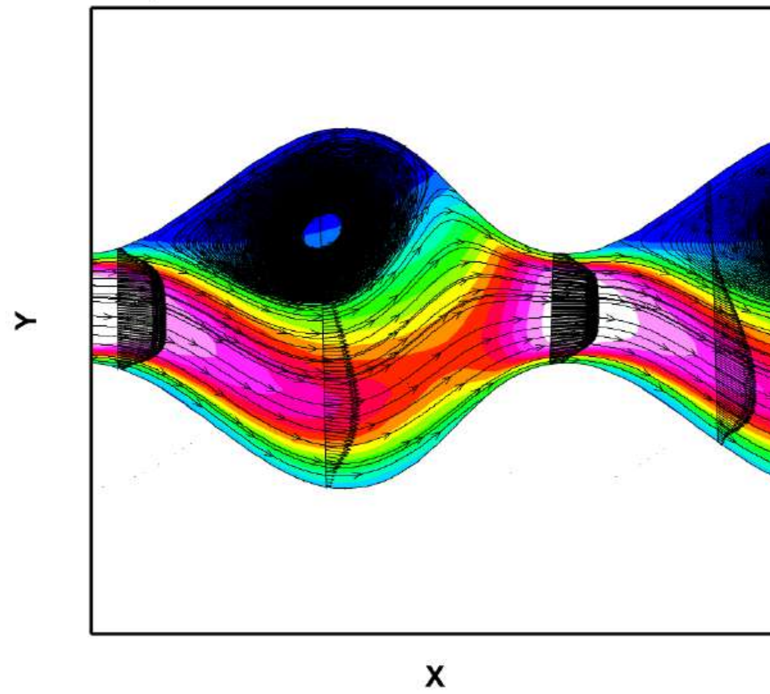

(c)

Figure 4.3: Streamline and velocity profile in wavy microchannel for (a) θ_p=0 (case 1) (b) θ_p= π/2 (case 2) (c) θ_p= π (case 3) at *Re* 700 and W_L = *14 mm*

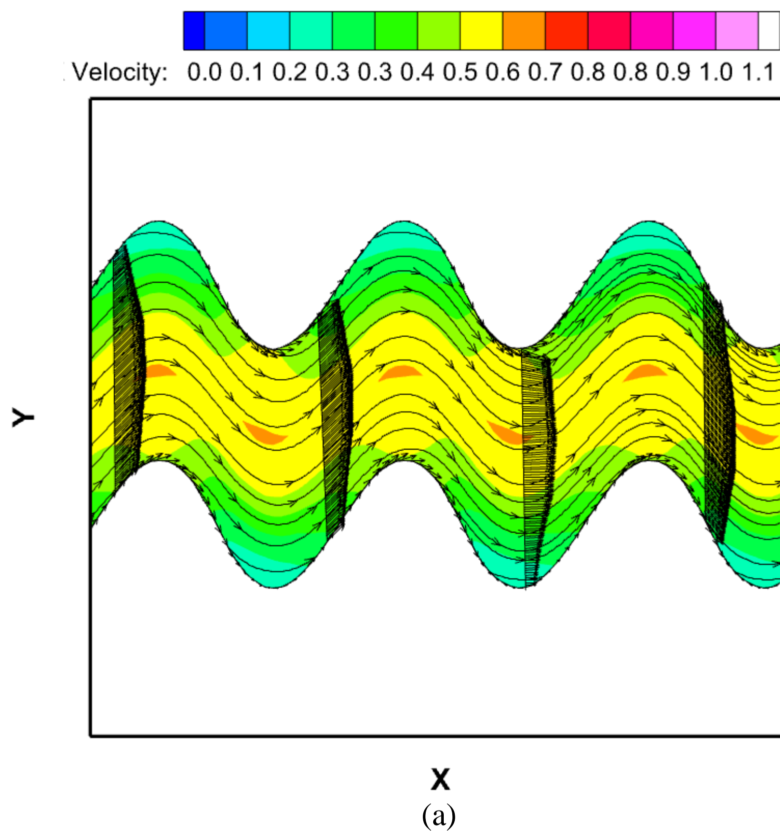

(a)

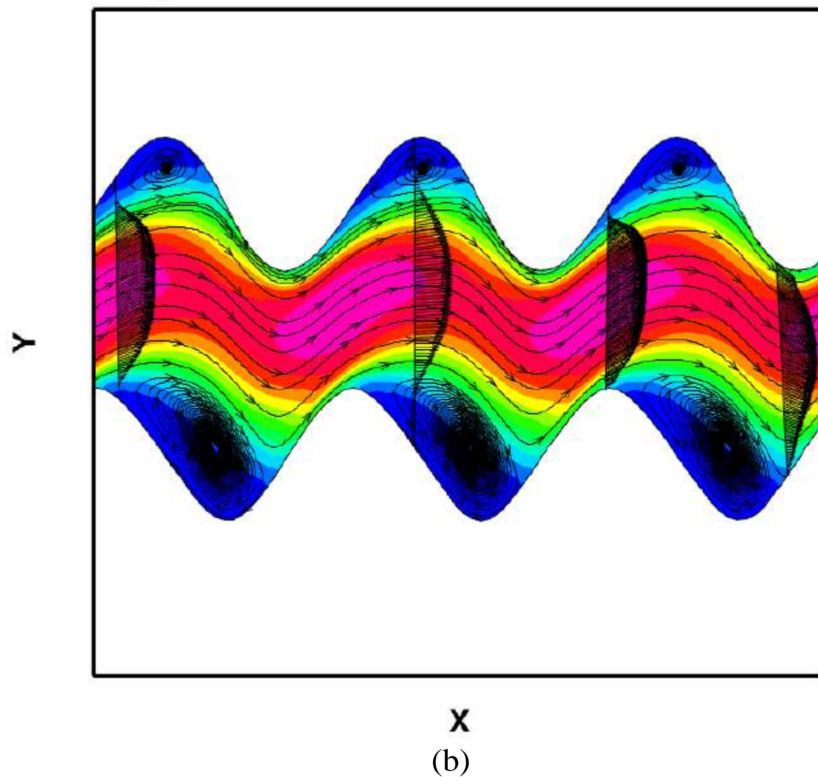

(b)

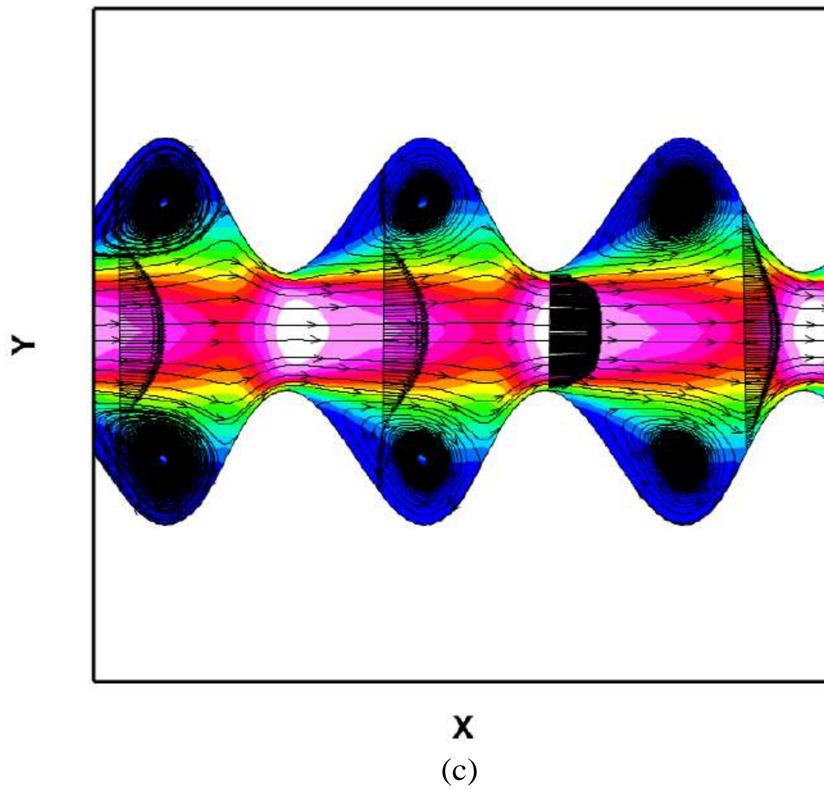

(c)

Figure 4.4: Streamline and velocity profile in wavy microchannel for (a) θ_p=0 (case 4) (b) θ_p= π/2 (case 5) (c) θ_p= π (case 6) at *Re* 700 and W_L = 7 mm

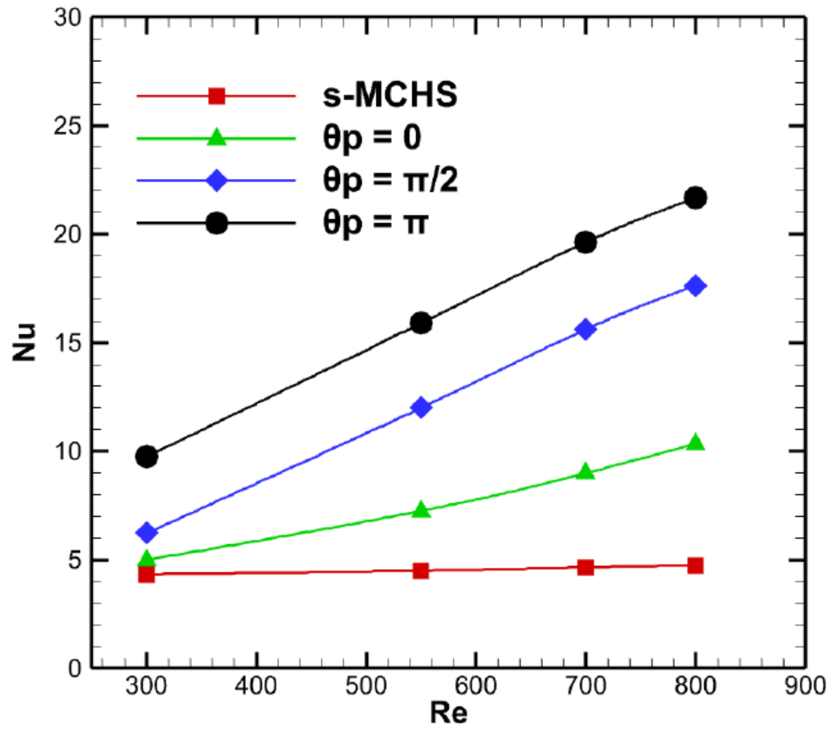

(a)

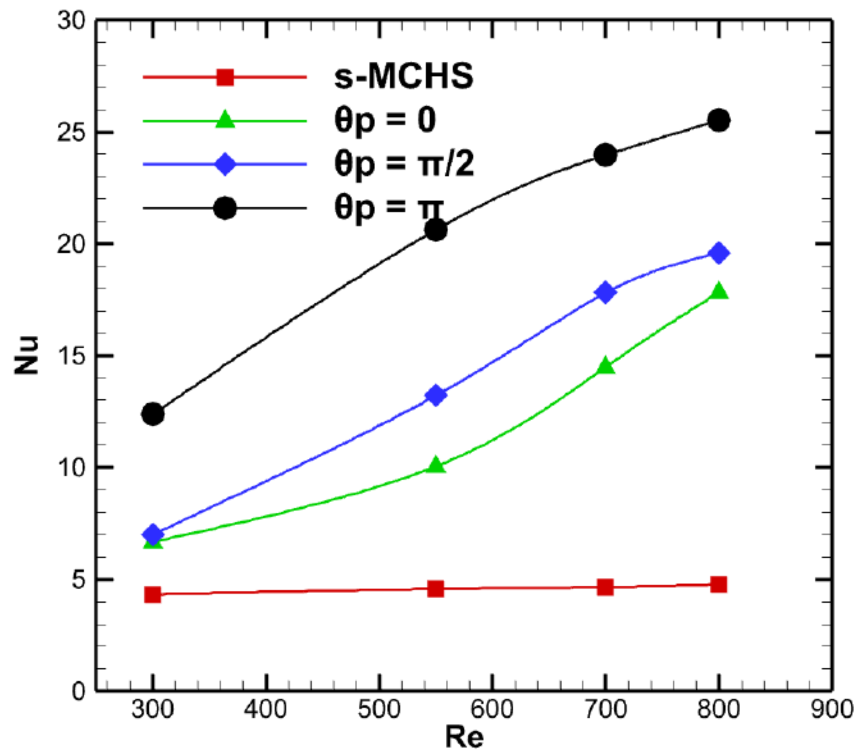

(b)

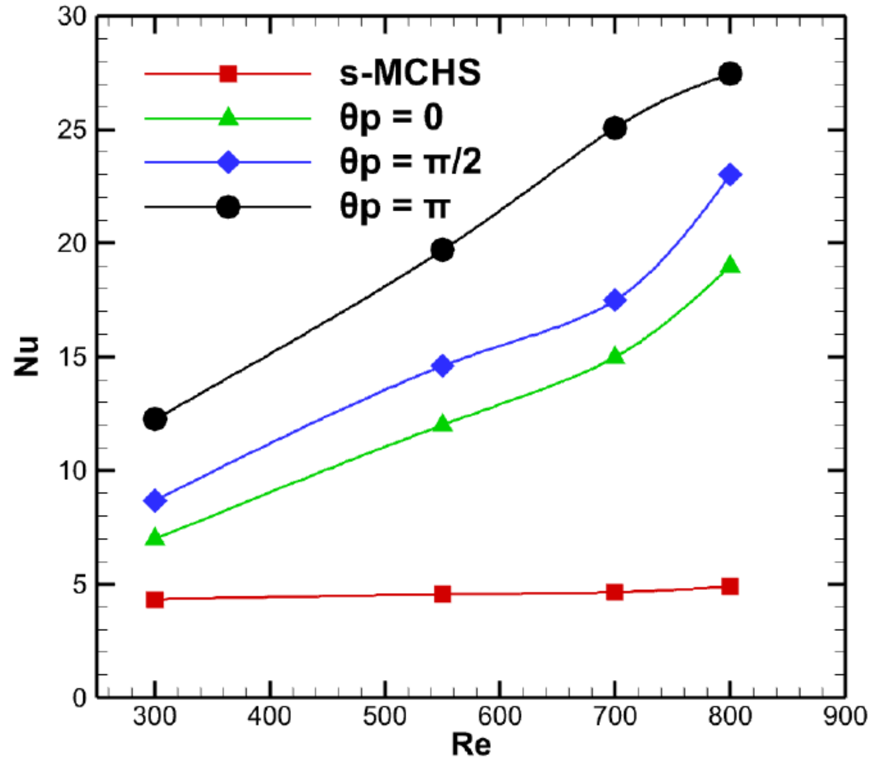

(c)

Figure 4.5: Variation of average *Nu* with *Re* for wavy channel (a) W_L = 14 mm (case 1- case 3) (b) W_L = 7 mm (case 4- case 6) (c) W_L = 3.5 mm (case 7- case 9)

Heat transfer can be enhanced by increasing surface area, temperature gradient, and heat transfer coefficient. Surface area enhancement due to waviness is less than *5%* in w-MCHS. So, heat transfer is enhanced in w-MCHS by increasing temperature gradient and heat transfer coefficient.

Two prominent effects are found in 2D w-MCHS: (i) flow reversal and changing velocity direction from the centerline, (ii) different velocity magnitude due to changes in cross-sectional area along the flow directions. These effects cause the interruption and redevelopment of the thermal boundary layer in w-MCHS. So, the temperature gradient and heat transfer coefficient are enhanced in w-MCHS. The advective and convective effects in the wavy MCHS are enhanced by vorticity at $\theta_p = \pi/2, \pi$. Vorticity formation and boundary layers redevelopment are more intense for phase-shifted wavy MCHS than wavy MCHS with $\theta_p = 0$ (case 1, case 4, case 7). As a result, the Nusselt number (Nu) is higher for phase shift, $\theta_p = \pi/2, \pi$ than s-MCHS and w-MCHS with $\theta_p =$

0 regardless of W_L as shown in fig 4.5. Nu for phase shift, $\theta_p = \pi$ is higher for all wavelengths

Figure 4.6 depicts the maximum induced velocity in MCHS. While $\theta_p = \pi$, the induced velocity is higher than other cases. Higher velocity gradient is caused by higher vorticity, flow reversal, and thinning of boundary layer thickness.

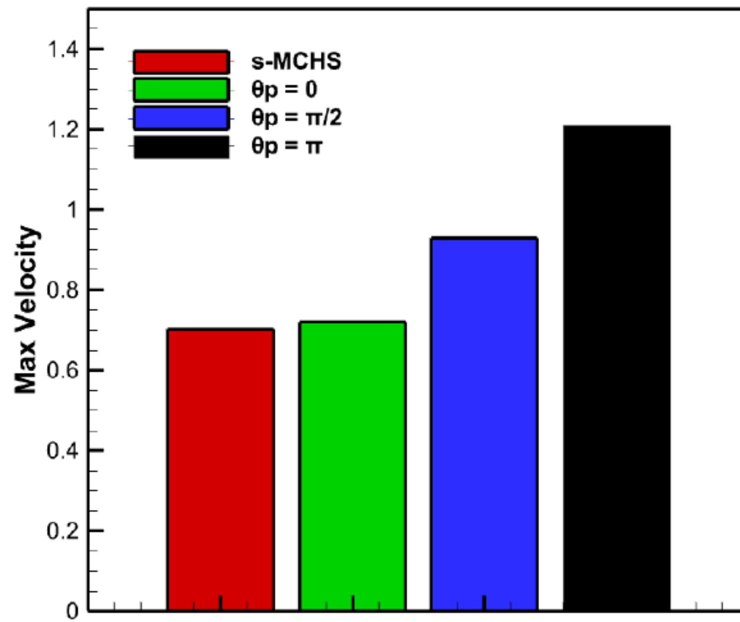

(a)

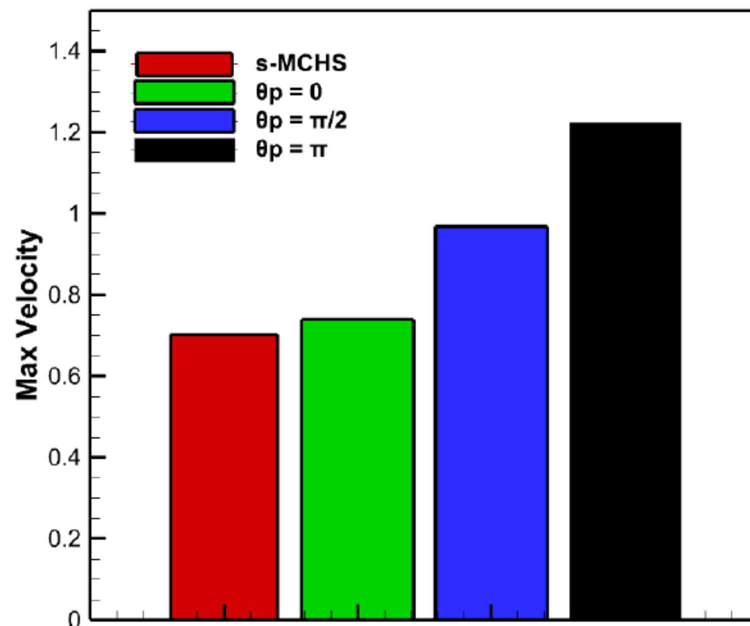

(b)

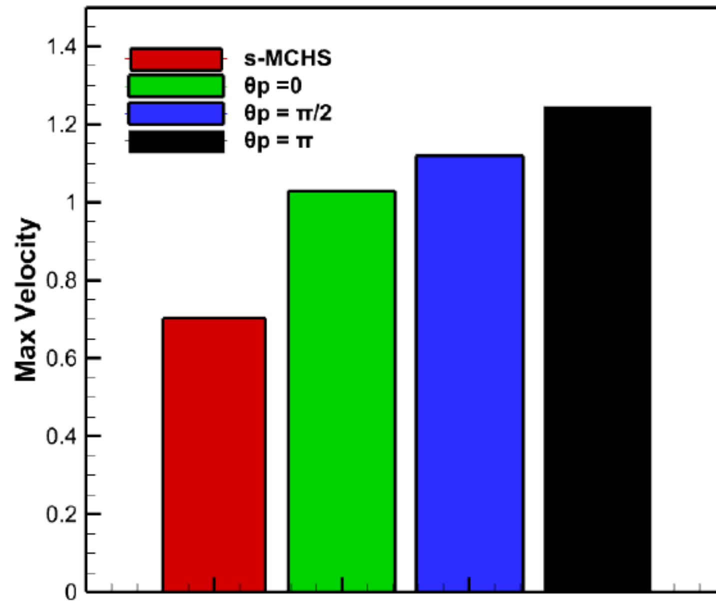

(c)

Figure 4.6: (a) Maximum induced velocity for W_L= *14 mm* (*case 1- case 3*) (b) maximum induced velocity for W_L =*7mm* (*case 4- case 6*) (c) maximum induced velocity for W_L =*3.5 mm* (*case 7- case 9*)

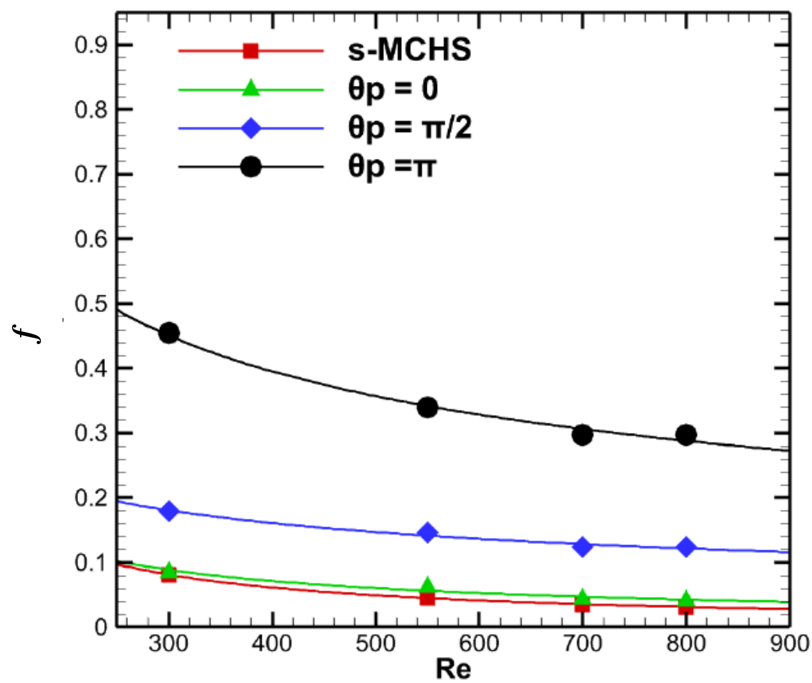

(a)

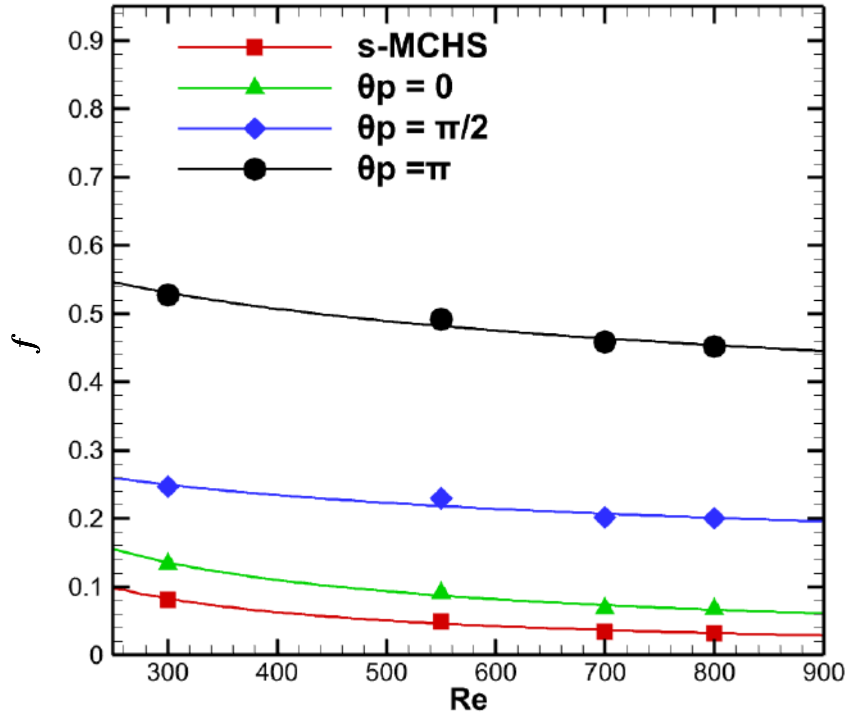

(b)

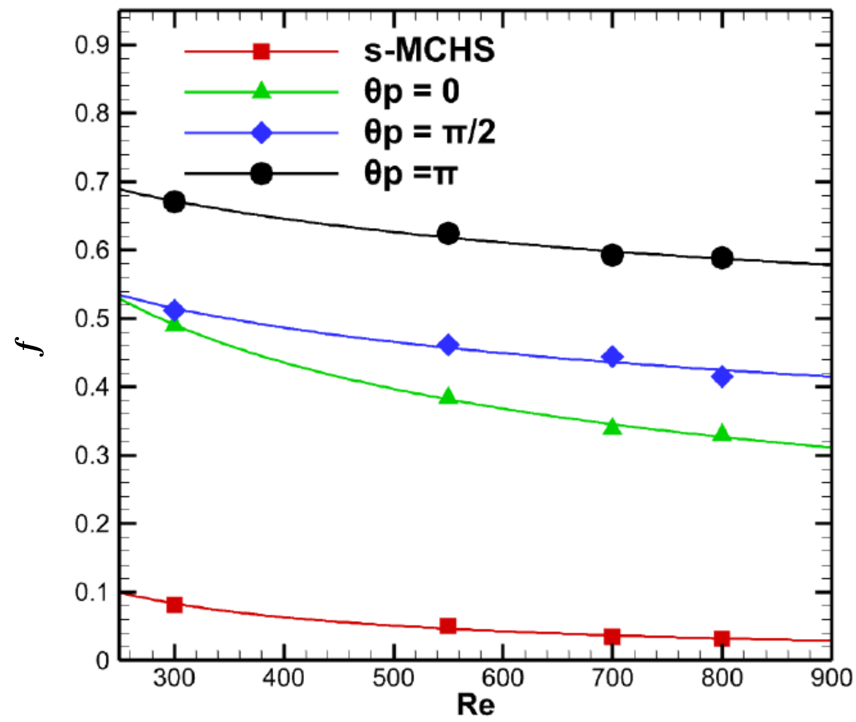

(c)

Figure 4.7: Variation *f* with *Re* for wavy channel (a) W_L= *14 mm* (*case 1- case 3*) (b) W_L = 7 mm (*case 4- case 6*) (c) W_L = 3.5 mm (*case 7- case 9*)

Moreover, the higher velocity gradient causes a higher shear force on the wall in MCHS. As a result, the pressure drop is higher for w-MCHS than s-MCHS. Pressure drop increases with θ_p. Similarly, smaller wavelength enhances the pressure drop in w-MCHS. Figure 4.7 shows the variation of friction factor (*f*) with the *Re*. Friction factors for w-MCHS are higher than s-MCHS in all cases.

4.3 Effect of Sinusoidal Waviness and Interconnectors in 3D MCHS

Interconnectors (IC) in MCHS can significantly improve the thermal performance of MCHS [48, 49]. IC allows the cross-flow in the counter flow MCHS. The percentage of coolant flowing from one channel to another is called cross-flow. Hence, the thermal boundary layer was disputed in IC s-MCHS. However, IC is found to be inactive in the parallel flow MCHS. The current study will investigate the effect of waviness in interconnected mini-channel. Hence, sinusoidal waviness was added on walls of MCHS normal to Z-direction. The wavy wall follows $Y=W_A sin(\theta+\theta p)$. θ_p is the phase shift of the w-MCHS. The position of interconnector is kept constant in the analysis. Tikadar et al. studied straight mini-channel with three different length (L_i) of interconnectors (*4 mm , 6.5 mm,* and 9 *mm* from the inlet of the MCHS). They stated that lower L_i caused lower heat transfer and higher L_i caused higher pressure drop. Therefore, L_i is selected *6.5 mm* in the research.

4.3.1 Pressure and Velocity Distribution

When the counter flow MCHS has the interconnectors (IC) between two channels, the pressure difference is generated across the IC of the MCHS resulting cross-flow. Hence, the pressure and velocity distribution in MCHS are investigated extensively. Figure 4.8 shows pressure, streamline, and velocity profile in the XY plane to better comprehend cross-flow and boundary layer redevelopment and disruption in IC s-MCHS and IC w-MCHS. At the presence of IC, the cross-flow occurs in the MCHS. As illustrated in fig 4.8, the cross-flow causes flow separation, recirculation, and reattachment. As an outcome, boundary layer in the MCHS is disrupted. The velocity profile in both IC s-MCHS and IC w-MCHS cannot be fully developed in the presence of interconnectors, as illustrated in fig 4.8.

Furthermore, the interruption and redevelopment of the boundary layer are also enhanced in MCHS by adding waviness in interconnected MCHS, as illustrated in fig 4.9. The waviness also provokes the vorticity and flow reversal in the MCHS, as shown in fig 4.10. Hence, the pressure drop and chaotic advection [31] rise in the MCHS, as shown in fig 4.8 and fig 4.9. Waviness enhances the pressure drop in the MCHS. On the other hand, the interconnectors reduce the pressure drop in MCHS, as shown in fig 4.11. The interconnectors divide the flow region into three zones. Fluid flow gets separated in zone 1 and gets reattached again in zone 3 owing to the presence difference across the ICs. As a result, the pressure in MCHS rises in zone 2 and decreases in zone 3, following Bernoulli's principle. Similarly, velocity quickly decreases in zone 2 and increases in zone 3, as illustrated in fig 4.11. The pressure drop across the IC w-MCHS is lower than w-MCHS in the presence of IC.

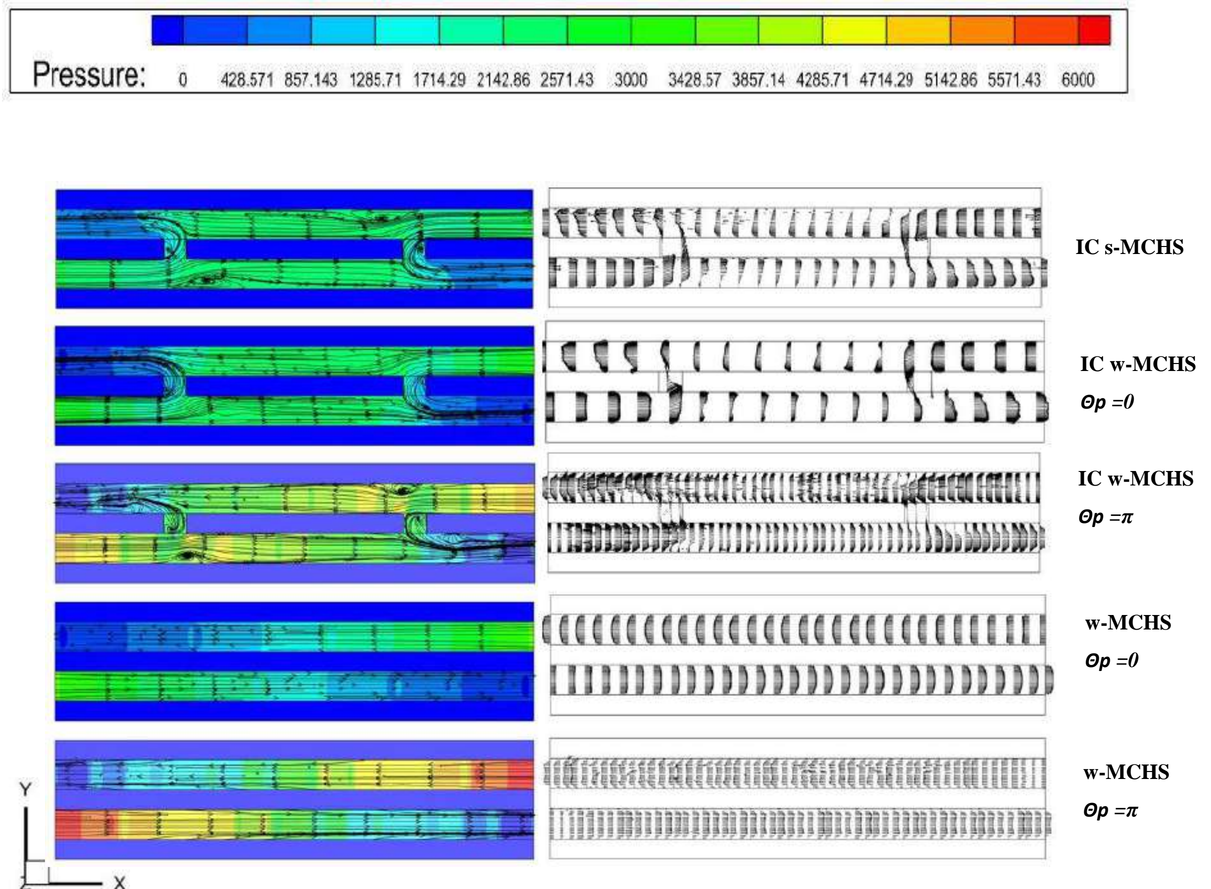

Figure 4.8: Pressure and velocity profile in center plane of the MCHS at *Re = 800*

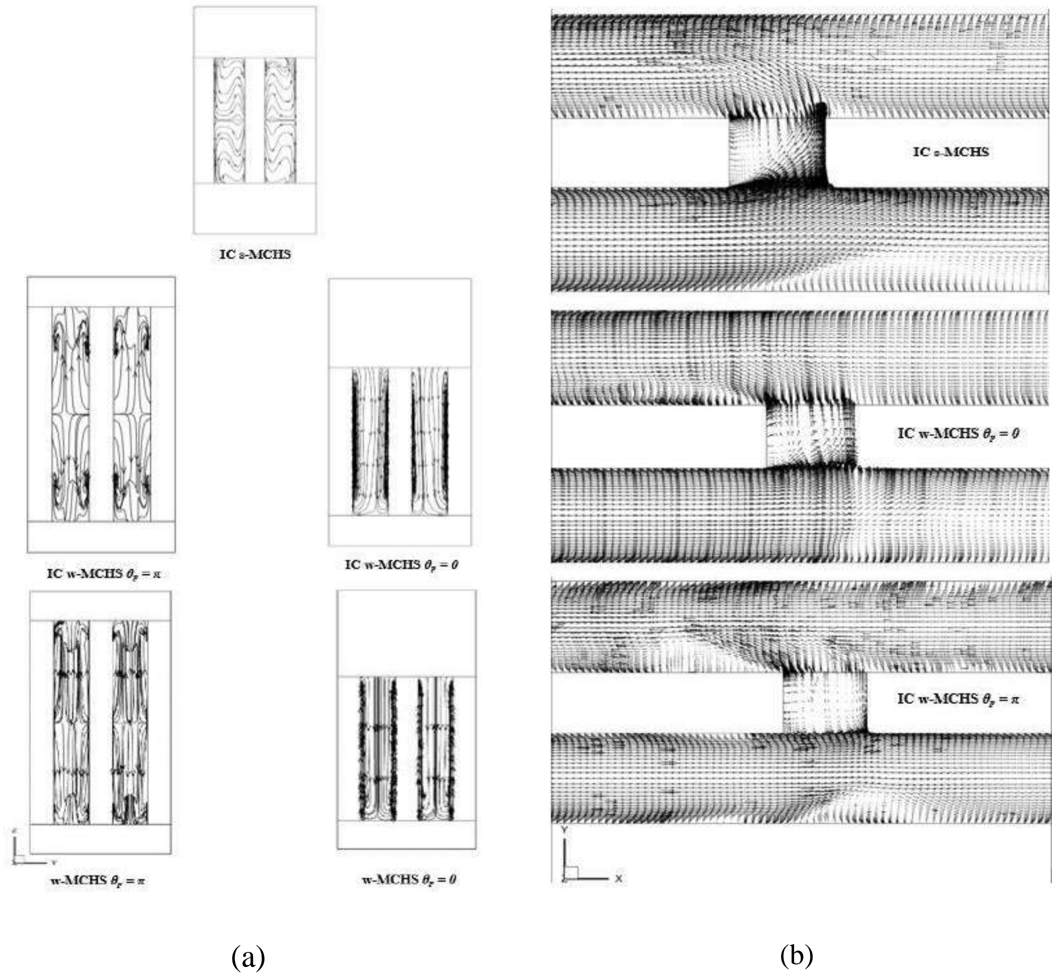

Figure 4.9: (a) Streamline (*x = 0.13 mm*) in the MCHS (b) velocity vector field at *z = 0.45 mm* velocity contour in the ZX plane of the MCHS at *Re = 800*

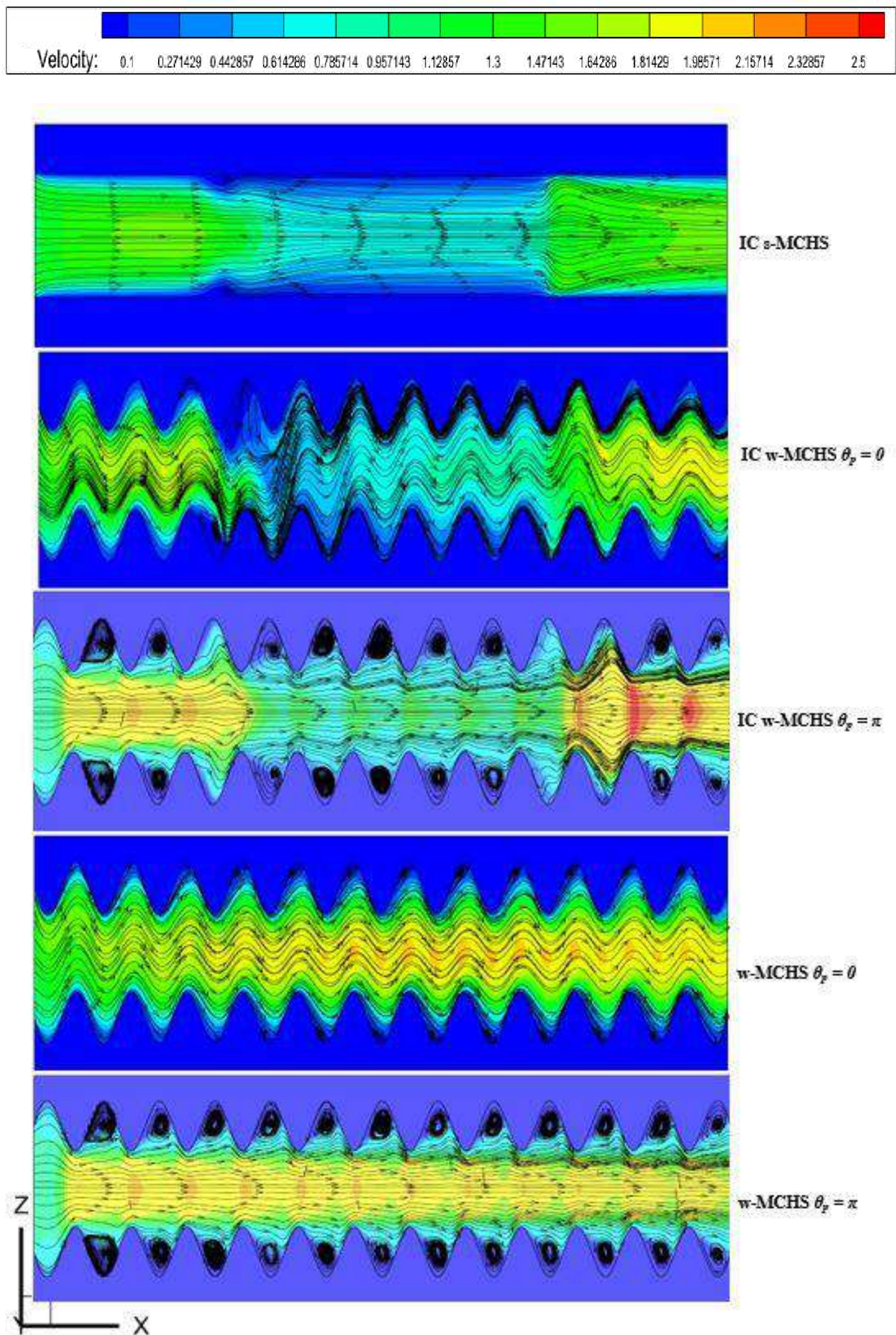

Figure 4.10: Velocity contour in the ZX plane of the MCHS at $Re = 800$

As the pressure drop of IC w-MCHS is lower than w-MCHS, the friction factor (f) is also lower for IC w-MCHS than w-MCHS. At $Re = 300$ and for $\beta = 0.08$ and $\alpha = 0.2$, f is found *15%* lower for IC w-MCHS, $\theta_p = 0$ compared to w-MCHS, $\theta_p = 0$ and f is found *31%* lower for IC w-MCHS, $\theta_p = \pi$ compared to w-MCHS, $\theta_p = \pi$ shown in fig 4.12. However, the f of IC w-MCHS is higher than s-MCHS and IC s-MCHS due to the waviness.

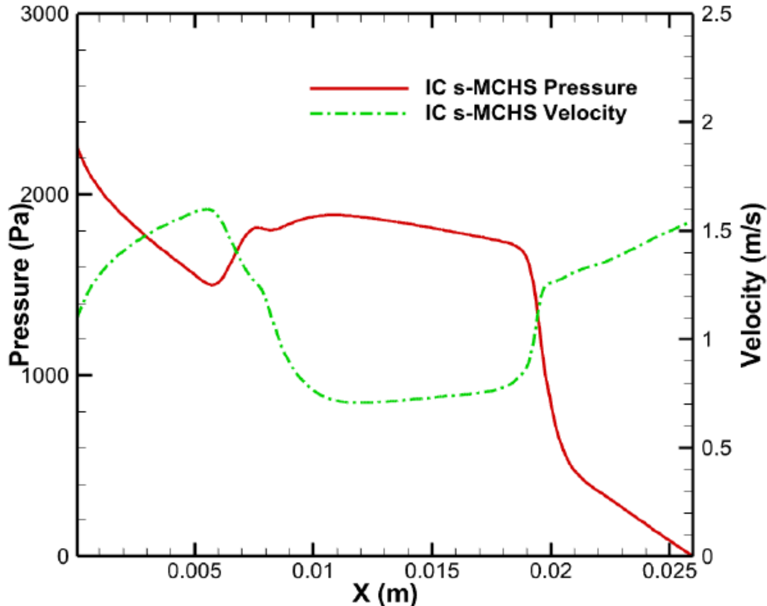

(a)

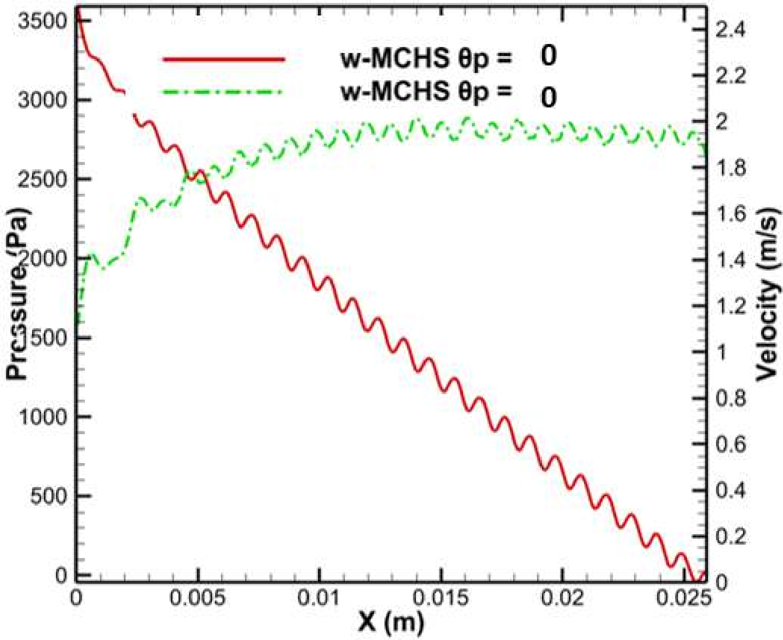

(b)

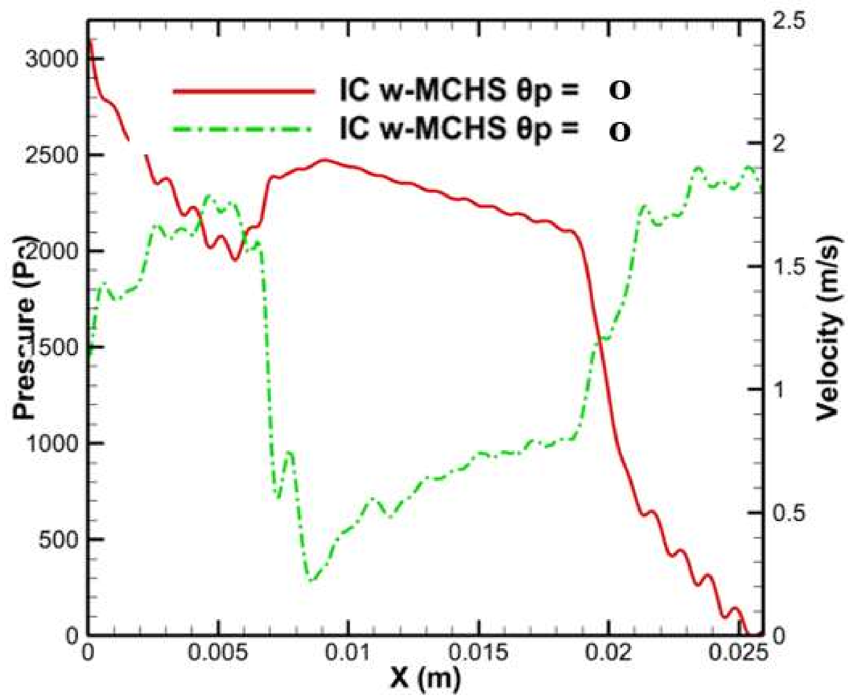

(c)

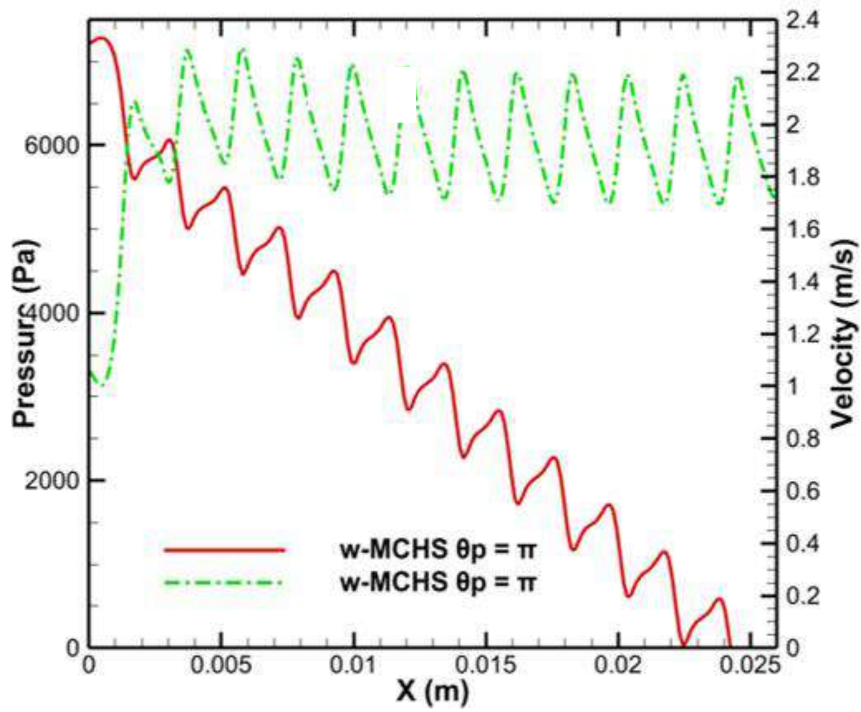

(d)

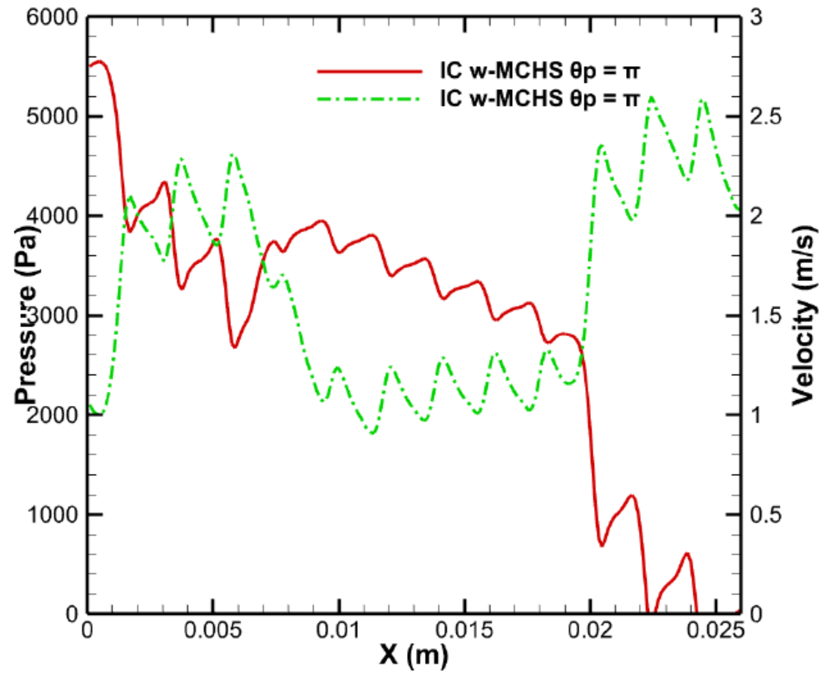

(e)

Figure 4.11: Pressure and velocity along with centerline in XY-plane (a) IC s-MCHS (b) w-MCHS, $\theta_p = 0$ (c) IC w-MCHS, $\theta_p = 0$ (d) w-MCHS, $\theta_p = \pi$ (e) IC w-MCHS, $\theta_p = \pi$

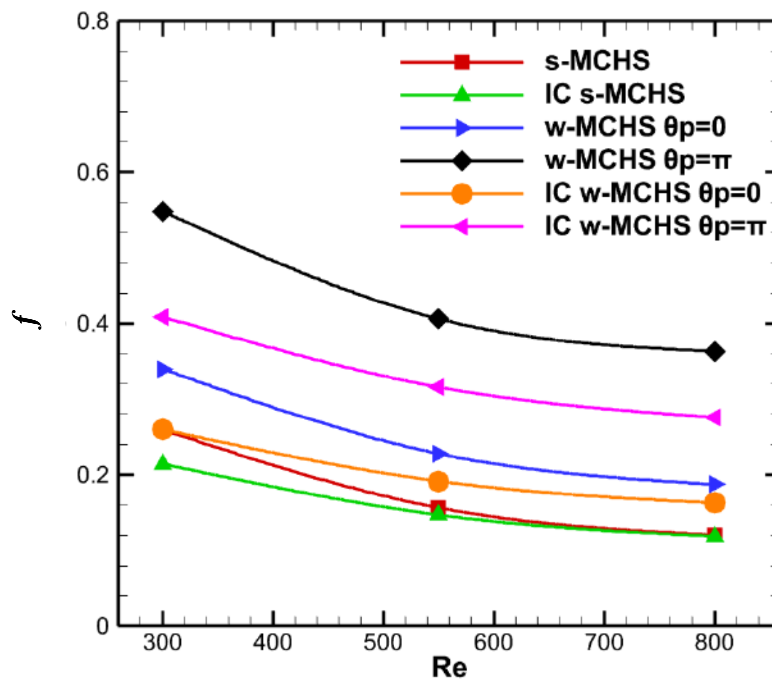

Figure 4.12: Variation of friction factor (f) with Re for $\alpha = 0.2$ and $\beta = 0.08$

4.3.2 Local Temperature Distribution

Figure 4.13 depicts the local temperature distribution at the MCHS's lower surface at *Re = 800*. The coolant in the counter flow MCHS comes from the opposite directions. Thus, the inlet and outlet temperature is lower and higher in the middle zone. A wavy channel generates greater vortices and flow reversal than s-MCHS, and it enhances chaotic advection and improves the mixing of coolant in the MCHS. As a result, the temperature at the bottom surface of both IC w-MCHS and the w-MCHS is lower than the IC s-MCHS and s-MCHS. It is discussed in the previous section that fluid flow decreases in zone 2 due to the cross flow in the interconnected MCHS. As a result, the temperature in zone 2 rises in the interconnected MCHS. The temperature at zone 2 increases with the percentage of cross flow in interconnected MCHS.

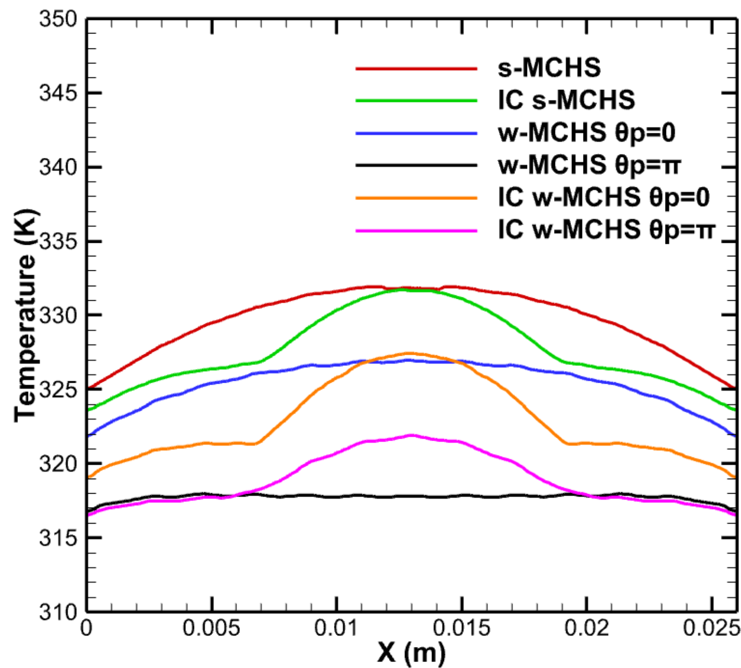

Figure 4.13: Local temperature distribution at the bottom of the microchannel at *Re = 800*

Temperature is lower in wavy channel than s-MCHS and IC s-MCHS. Whereas at $\theta p = \pi$, the temperature is the lowest in w-MCHS and IC w-MCHS, as shown in fig 4.13. The cross-sectional area of MCHS at $\theta_p=\pi$, as shown in fig 3.2(d), gradually decreases and increases. It causes rapid acceleration and deceleration of fluid flow. Therefore, the boundary layers are disturbed severely.

4.3.3 Maximum Temperature Reduction

Figure 4.14 shows the maximum temperature of channel's bottom surface as a function of *Re* at a constant heat flux of *q''= 32 W/cm²*. As shown in fig 4.13, both IC w-MCHS and w-MCHS regardless of phase shifts show lower temperature than IC s-MCHS and s-MCHS under constant heat flux condition. Due to drop in mass flow rate in zone 2 for interconnected channels, maximum temperature rises in zone 2. Thus, the temperature is slightly higher in IC w-MCHS than w-MCHS. As illustrated in fig 4.14, the maximum temperature reduction has been found for $\theta_p = \pi$. At $\theta_p = \pi$, maximum *28%* and *24%* reduction have been recorded for w-MCHS and IC w-MCHS with respect to s-MCHS at *Re=800*.

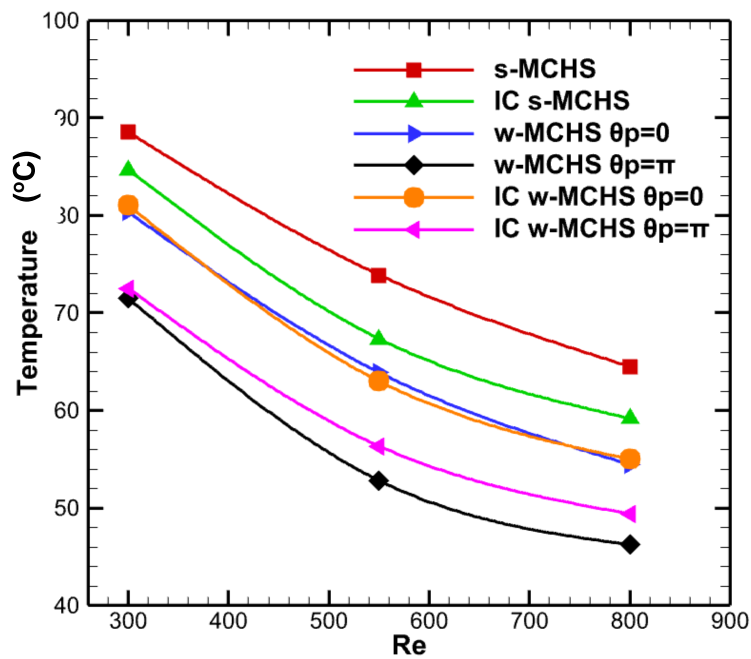

Figure 4.14: Maximum bottom temperature of MCHS at constant heat flux, *q''= 32 W/cm²*

4.3.4 Maximum Heat Flux Extraction

It is essential to keep the maximum temperature of miniature electronic devices below *85°C* to ensure reliability and efficiency [12]. Figure 4.15 depicts the maximum temperature of MCHS (~*85 °C*) with heat flux response at constant *Re=800*. As shown in fig. 4.15, w-MCHS with $\theta_p = \pi$ can withstand a heat flux up to *96 W/cm²*, which is *94%* higher than s-MCHS, while keeping the maximum temperature below *85°C*. IC w-MCHS, $\theta_p = \pi$ can extract heat flux up to *84 W/cm²*, which is *70%* more heat flux

than s-MCHS. w-MCHS can remove more heat flux than IC w-MCHS. IC w-MCHS removes less heat flux than w-MCHS due to cross flow.

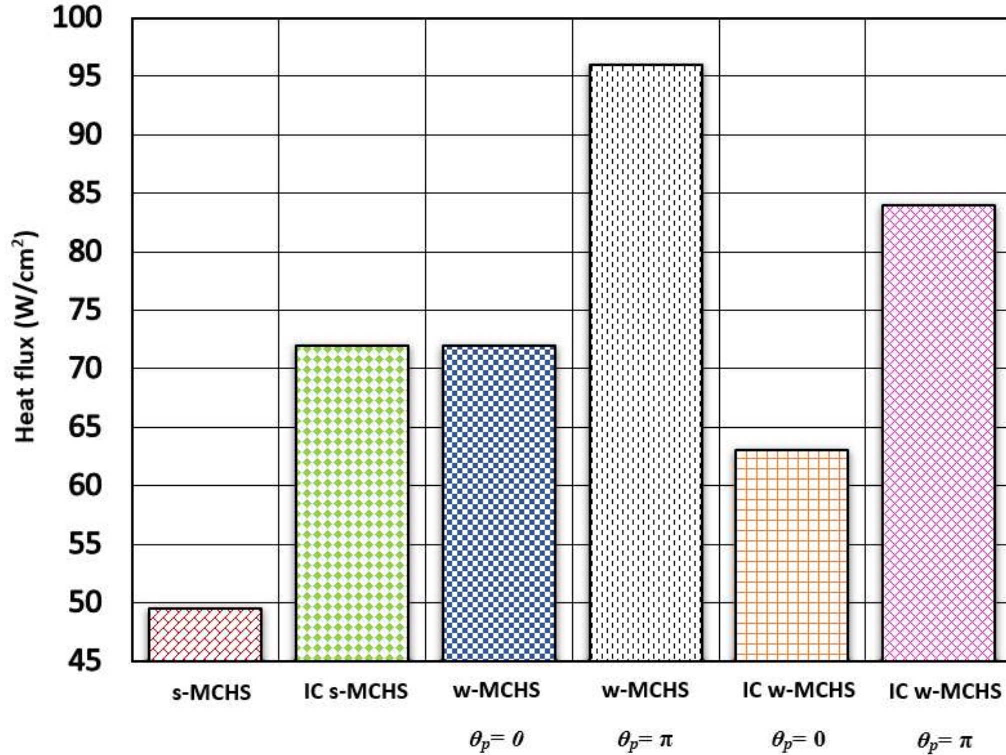

Figure 4.15: Maximum heat flux (*q”*) for different MCHS at maximum temperature 85^0C

4.3.5 Effect on Nusselt Number

The relationship between the average *Nu* and *Re* is depicted in fig 4.16. Two strategies can be used to increase net heat transfer: (i) increasing the effective heat transfer area, and (ii) interrupting and redeveloping the thermal boundary layer. Because the IC w-MCHS has a surface area that is only *6.2%* higher than the s-MCHS, heat transfer enhancement through increased surface area is insignificant, meaning that heat transfer enhancement is predominantly achieved by interrupting the thermal boundary layer. In the case of an IC w-MCHS, a significant increase in *Nu* is visible in fig. 4.16. The enhancement in heat transfer in IC w-MCHS is due to the significant interruption and re-development of the thermal boundary layer, and better fluid mixing, as shown in fig. 4.9 and 4.10. *Nu* increases with *Re* in all cases. At $\theta_p = 0$, *Nu* for IC w-MCHS is higher than w-MCHS for all *Re* due to the flow separations, attachment, and

recirculation. Therefore, the combine effect of secondary flow due to ICs and waviness surpasses the heat transfer effect in IC w-MCHS at $\theta_p = 0$ than w-MCHS, as illustrated in fig. 14.16.

At $\theta_p = \pi$, *Nu* is higher for IC w-MCHS than w-MCHS at lower *Re*. Effect of ICs reduces with the increment of *Re*. The convective effect owing to waviness becomes weak in the presence of ICs in channels. Due to flow separation in ICs, zone 2 has a lower coolant flow rate. The lower flow rate reduces the convective effect in zone 2 of IC w-MCHS and raises the temperature of the bottom of the mini-channel. Therefore, Nu is slightly lower for IC w-MCHS than w-MCHS at $Re=800$ and $\theta_p = \pi$. Maximum *Nu* has been recorded *99%* and *59%* enhancement compared to s-MCHS at $Re=550$ for IC w-MCHS, $\theta_p = \pi$, and IC w-MCHS, $\theta_p = 0$, respectively.

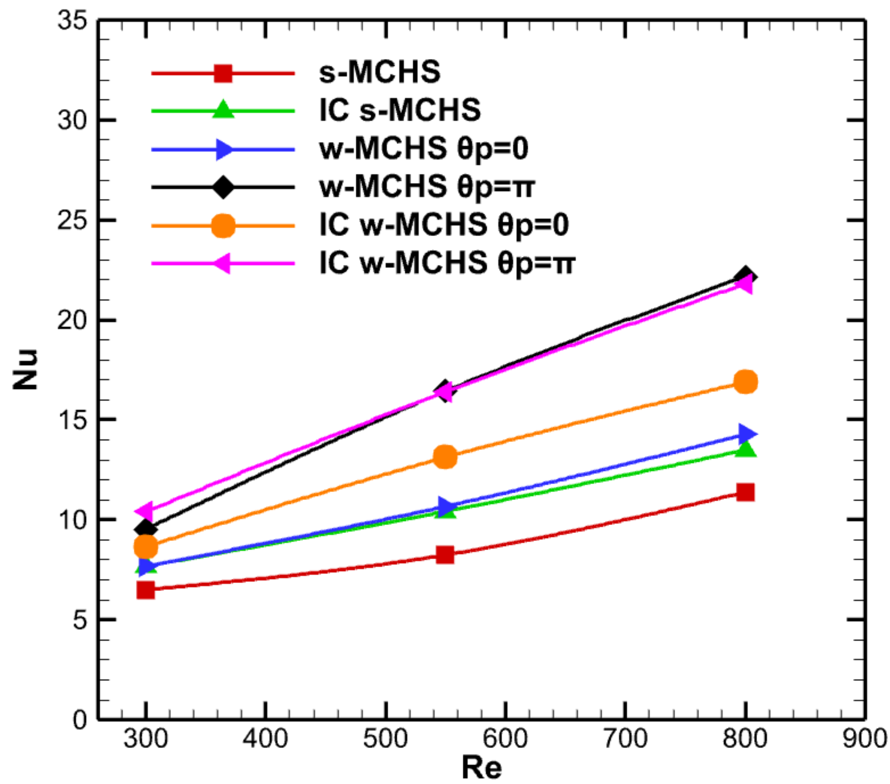

(a)

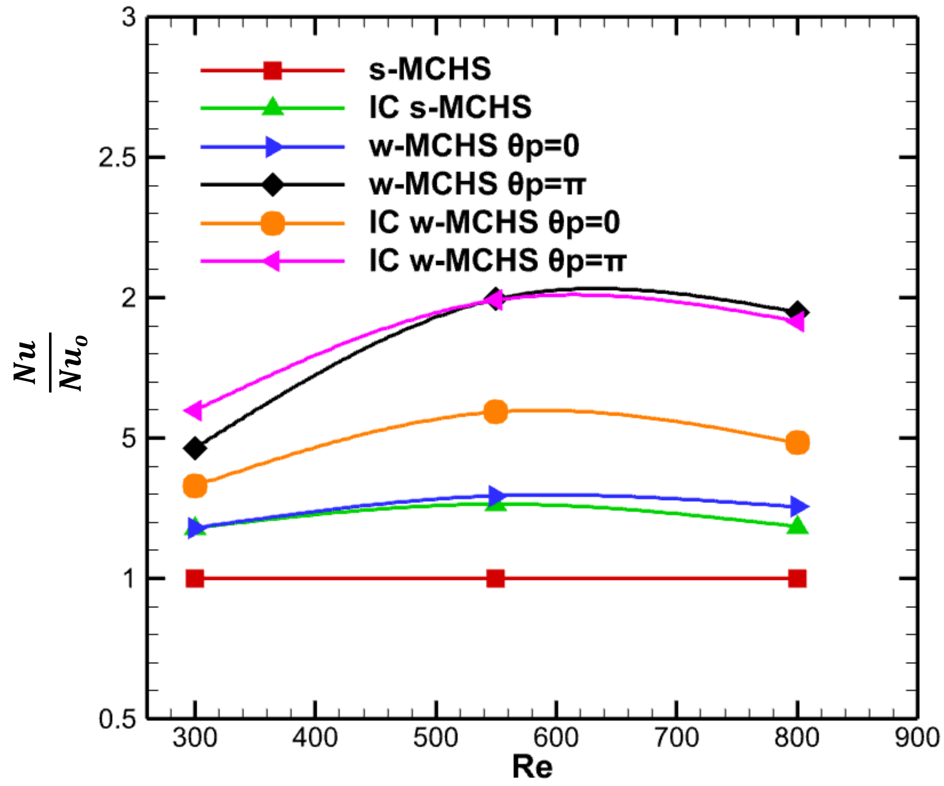

(b)

Figure 4.16: (a) Variation of *Nu* with *Re* (b) Variation of Nusselt number ratio with $Re = 800$ for $\alpha = 0.2$ and $\beta = 0.08$

4.3.6 Performance Evaluation Criteria

PEC is simply the ratio of *Nu* of IC w-MCHS, w-MCHS and IC s-MCHS to the Nu_o of s-MCHS at the same *Re*. *PEC* is greater than *1* shows better thermal and hydraulic performance compared to s-MCHS. The performance evaluation criteria (*PEC*) for mini-channel in all scenarios are shown in fig. 4.17. *PEC* for IC w-MCHS for all phase shifts is higher than all other cases. Maximum *PEC*'s are recorded *1.58*, *1.49* for IC w-MCHS, $\theta_p = \pi$, IC w-MCHS, $\theta_p = 0$ respectively, at $Re=550$. On the other hand, *PEC* for w-MCHS at $\theta_p = \pi$, w-MCHS at $\theta_p = 0$, IC s-MCHS, and s-MCHS are *1.45*, *1.14*, *1.29*, and *1*, respectively.

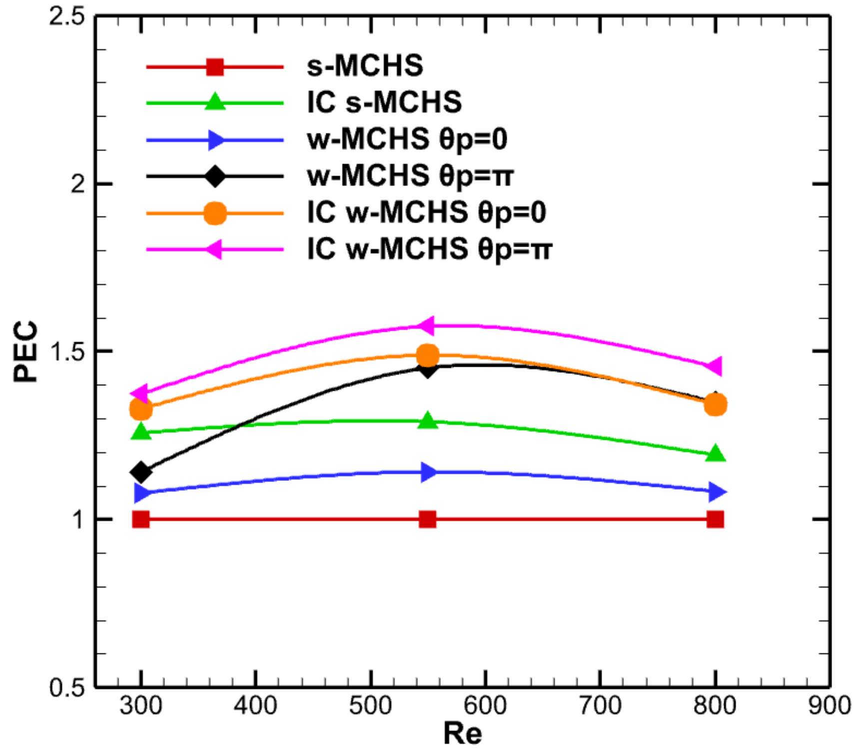

Figure 4.17: Variation of *PEC* with *Re* for $\alpha = 0.2$ and $\beta = 0.08$

4.4 Effect of Amplitude and Wavelength in 3D IC w-MCHS

4.4.1 Effect of Amplitude and Wavelength in Cross Flow

Introducing secondary flow caused by the interconnectors and waviness in the MCHS contribute to improving the thermal performance of MCHS. The thermal performance of interconnected MCHS is influenced by cross flow across the channels. Percent of cross flow is defined as the ratio of the mass flow rate going through the interconnectors and the total mass flow rate in the MCHS inlets. The pressure difference across the interconnector governs the percent of cross flow. Figure 4.18(a)-4.18(b) show the variation of the percent of cross flow for different amplitudes and wavelengths in IC w-MCHS. The percent of cross flow is nearly constant for IC w-MCHS, θ_p =0 regardless of amplitude ratio (α) and wavelength ratio (β) of sinusoidal wavy mini-channel. As the cross-sectional area of interconnectors are not changing with the variation of amplitude ratio and wavelength ratio as illustrated in fig 4.18(c)-4.18(d). Therefore, the change of pressure difference across the interconnectors and the percent of cross flow for IC w-MCHS, θ_p =0 are nearly constant at the same *Re* for different α and β.

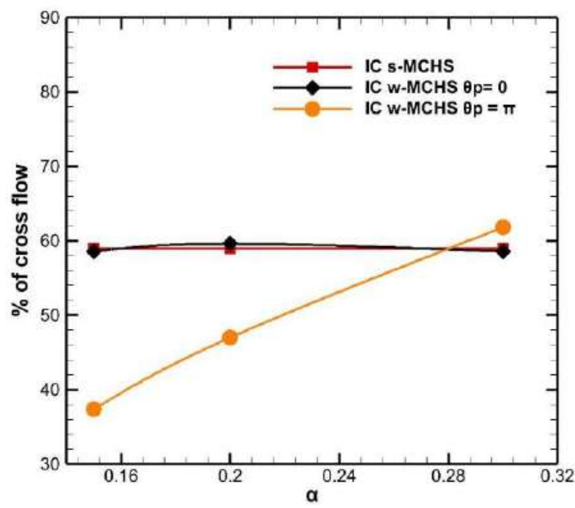

(a)

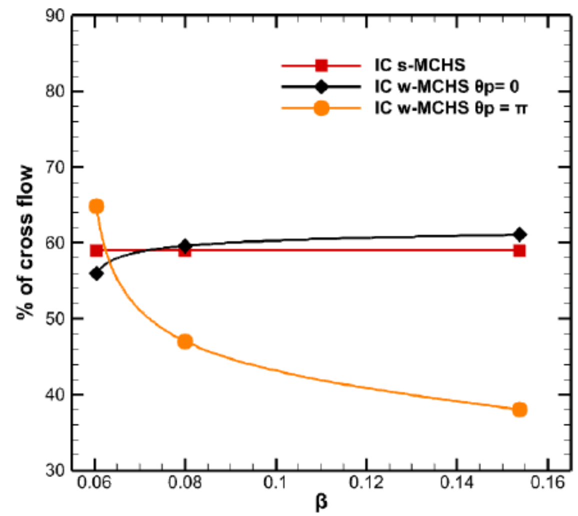

(b)

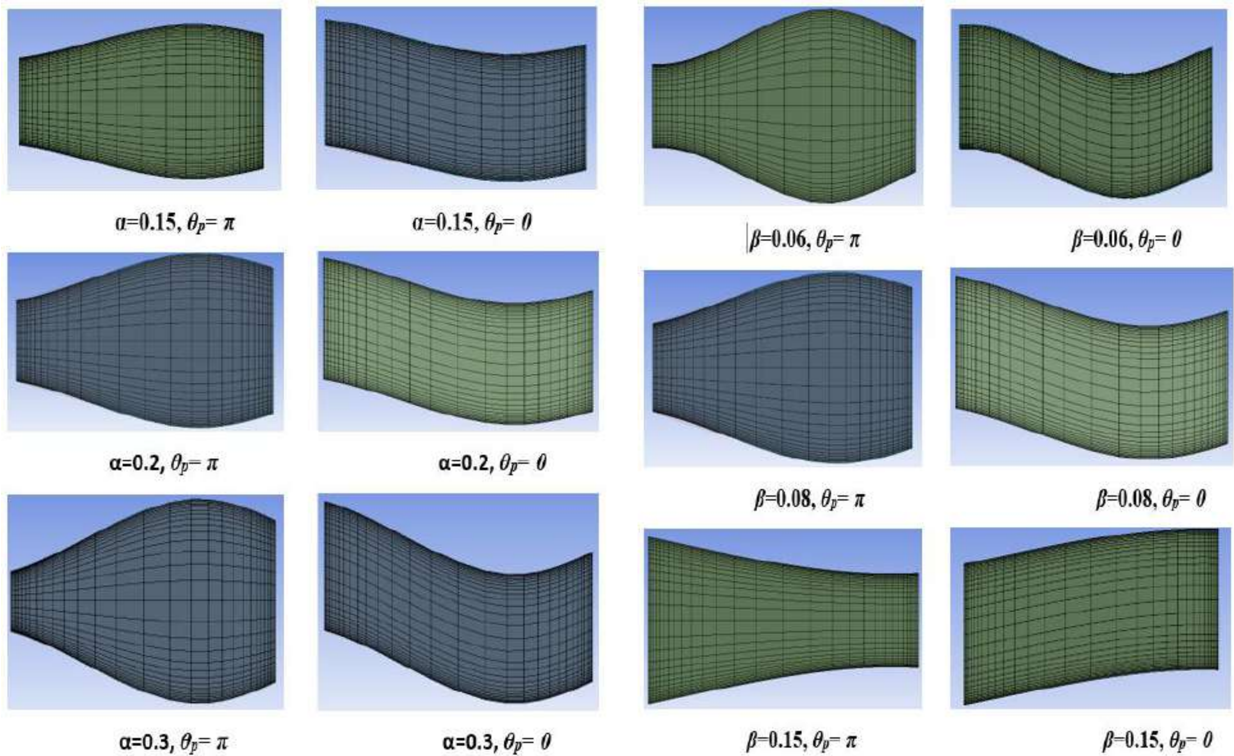

(c) (d)

Figure 4.18 (a) Variation of % of cross flow with different amplitude ratio, α at $Re=800$ (b) Variation of % of cross flow with different wavelength ratio, β at $Re=800$ (c) cross-sectional area's of interconnector for different amplitude ratio, α where $\beta=0.08$ (d) cross-sectional area's of interconnector for different amplitude ratio, β where $\alpha=0.2$

On the other hand, the percent of cross flow of IC w-MCHS, $\theta_p = \pi$ is greatly affected by α and β as the cross-sectional area of the interconnectors is varied with α and β at the same *Re*, as depicted in fig 4.18(c)-4.18(d). The percent of cross flow in IC w-MCHS, $\theta_p = \pi$ increases with the increment of α and β due to enhancement in pressure difference across interconnectors at the same *Re*.

4.4.2 Local Temperature Distribution

Figure 4.19(a)-4.19(f) illustrate the local temperature distribution for different α and β. The local temperatures of IC w-MCHS is lower than s-MCHS and IC s-MCHS in all cases. The waviness and interconnectors cause flow reversal, vorticity, etc. The vorticity and flow reversal improve the mixing of coolant. Hence, the local temperature of IC w-MCHS is lower than s-MCHS and IC w-MCHS. The local temperature of MCHS reduces with the increment of α. Similarly, the decrement of β reduces the local temperature of MCHS.

Figure 4.20(a)-4.20(f) illustrate the maximum temperature under constant heat flux. Maximum *19%, 24%* and *26%* reduction in bottom temperature are evicted in compared to s-MCHS for $\alpha=0.15$, $\alpha=0.2$ and $\alpha=0.3$ at *Re 800* for IC w-MCHS, $\theta_p = \pi$ respectively. Again, maximum *25%, 24%* and *10%* reduction in bottom temperature with respect to s-MCHS are evident for $\beta=0.06$, $\beta=0.08$ and $\beta=0.15$ at *Re 800* for IC w-MCHS, $\theta_p = \pi$ respectively. Similarly, Maximum temperature reduction in bottom surface of channels are found *13%, 15%* and *19%* compared to s-MCHS for $\alpha=0.15$, $\alpha=0.2$ and $\alpha=0.3$ for IC w-MCHS, $\theta_p = 0$ at *Re 800* respectively. Again, maximum *18%, 15%* and *11%* reduction in bottom temperature with respect to s-MCHS are evident for $\beta=0.06$, $\beta=0.08$ and $\beta=0.15$ at *Re 800* for IC w-MCHS, $\theta_p = 0$ respectively.

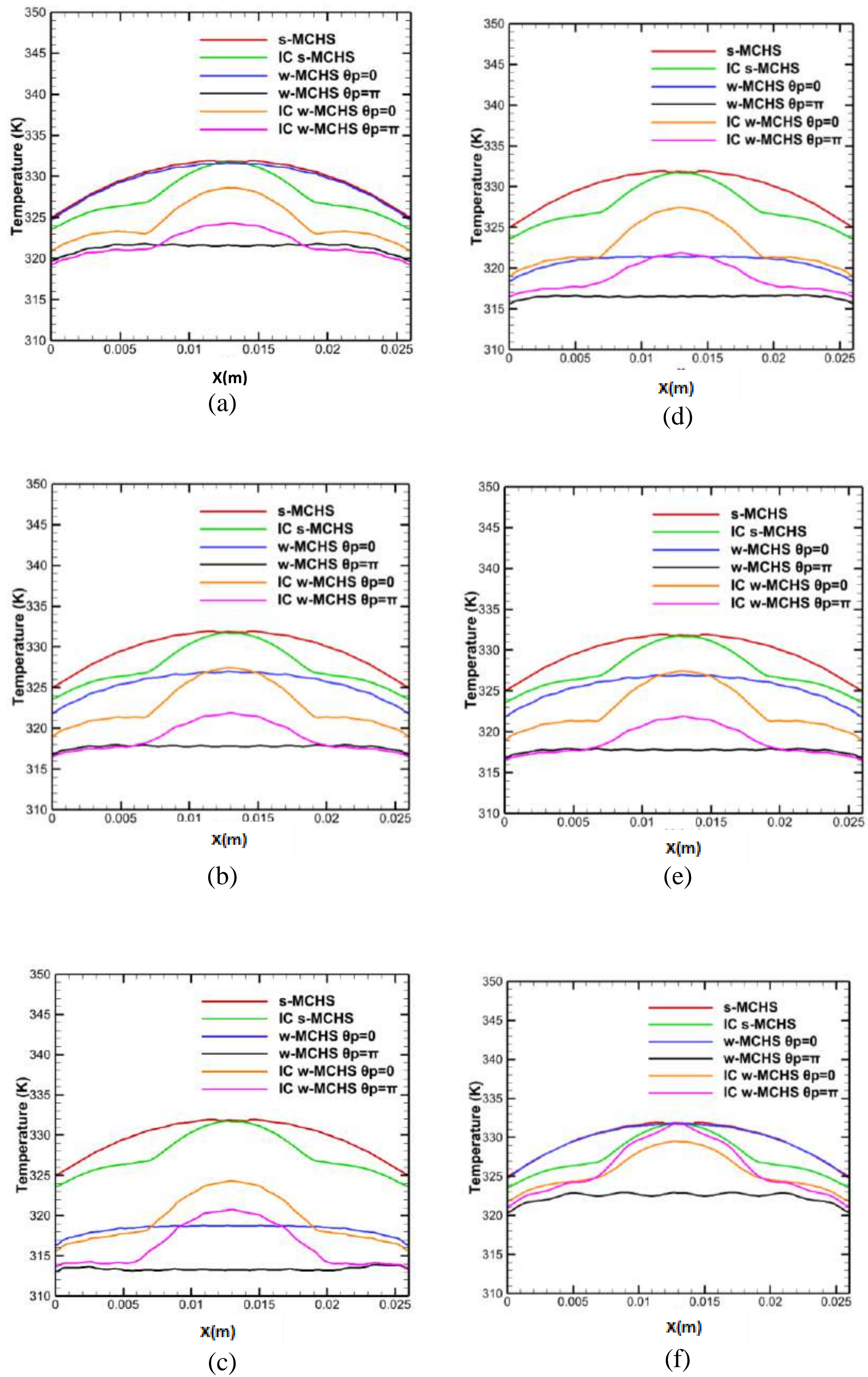

Figure 4.19: Variation of local temperature of bottom surface of MCHS at *Re=800* for (a) $\alpha = 0.15$ (b) $\alpha = 0.2$ (c) $\alpha = 0.3$ (d) $\beta = 0.06$ (e) $\beta = 0.08$ (d) $\beta = 0.15$

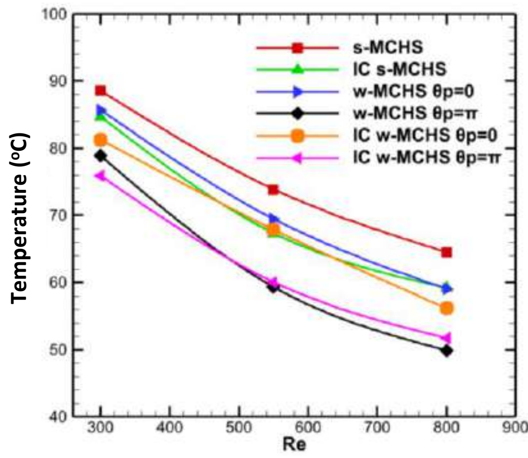

(a)

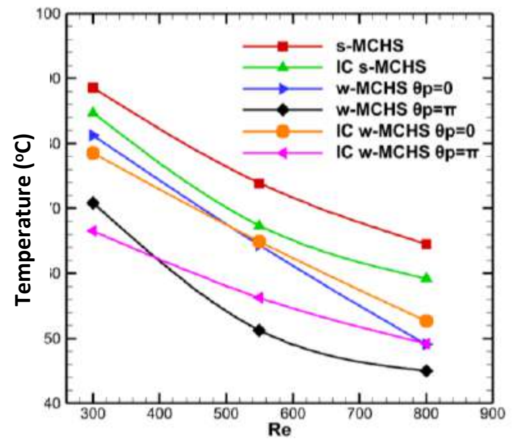

(d)

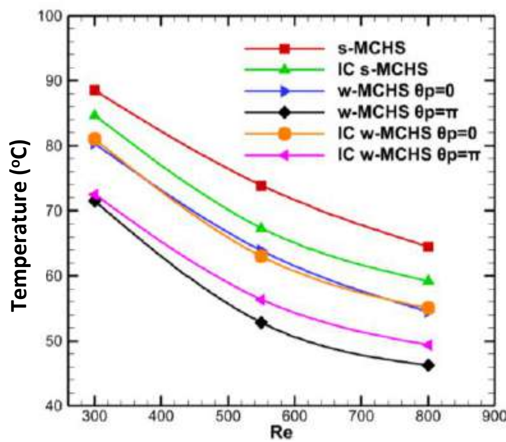

(b)

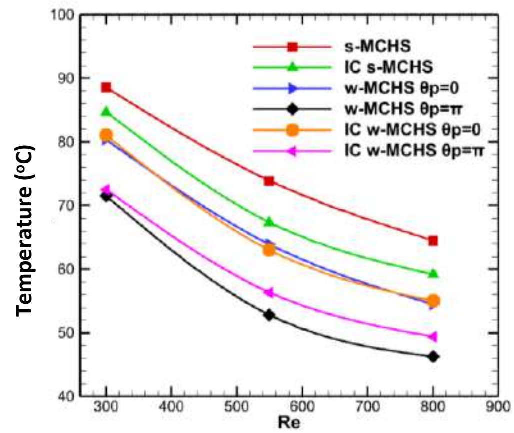

(e)

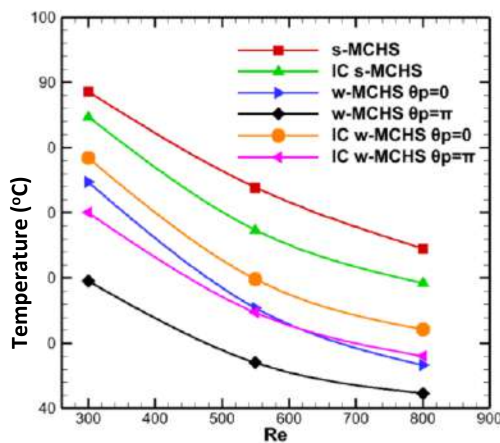

(c)

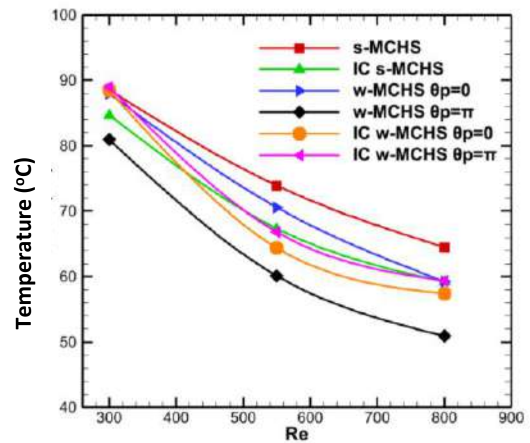

(f)

Figure 4.20: Variation of maximum bottom temperature (ºC) with Re under constant heat flux ($q''=32W/m^2$) for (a) $\alpha = 0.15$ (b) $\alpha = 0.2$ (c) $\alpha = 0.3$ (d) $\beta = 0.06$ (e) $\beta = 0.08$ (d) $\beta = 0.15$

4.4.3 Effect on Nusselt Number

Figure 4.21 and figure 4.22 illustrate the variation of Nu and Nu/Nu_o with respect to *Re*. *Nu* for IC w-MCHS increases with the increment of α and decrement of β for all *Re*. *Nu* for IC w-MCHS is higher than s-MCHS and IC s-MCHS for all cases. However, the effectiveness of interconnectors weakens with the increment of α and decrement of β in higher *Re*. Therefore, *Nu* is higher for w-MCHS than IC w-MCHS for $\theta_p = \pi$ and $\alpha = 0.3$. Maximum *52%*, *99%*, and *115%* increment in *Nu* at *Re 550* with respect to s-MCHS are evident for $\alpha=0.15$, $\alpha=0.2$ and $\alpha=0.3$ for IC w-MCHS, $\theta_p = \pi$. Again, maximum *104%, 99%* and *31%* increment in *Nu* at *Re 550* with respect to s-MCHS are evident for $\beta=0.06$, $\beta=0.08$ and $\beta=0.15$ for IC w-MCHS, $\theta_p = \pi$ respectively.

As the cross-flow is nearly unaffected by α and β, the efficacy of interconnectors at $\theta_p = 0$ is also unaffected by the variation of α and β. So, The *Nu* of IC w-MCHS at $\theta_p = 0$ is higher than w-MCHS in all cases. Maximum *37%, 59%* and *77%* increment in Nu at *Re 550* with respect to s-MCHS are evident for $\alpha=0.15$, $\alpha=0.2$ and $\alpha=0.3$ for IC w-MCHS respectively. Again, maximum *68%, 59%* and *31%* increment in *Nu* at *Re 800* with respect to s-MCHS are evident for $\beta=0.06$, $\beta=0.08$ and $\beta=0.15$ for IC w-MCHS respectively.

4.4.4 Effect on Friction Factor and PEC

Figure 4.23(a)-4.23(f) show the variation of friction factor, *f* with *Re*. It is found that *f* increases with increment of α and decrement of β. Figure 4.24(a)-4.24(f) show the Performance Evaluation Criteria (*PEC*) with respect to s-MCHS for different α and β. Increment of wave amplitude and decrement of wavelength increase the waviness effect in MCHS, so, *Nu* and pressure drop both increase with waviness. Interconnectors reduce the pressure drop in MCHS. Therefore, the *PEC* of IC w-MCHS is higher than w-MCHS.

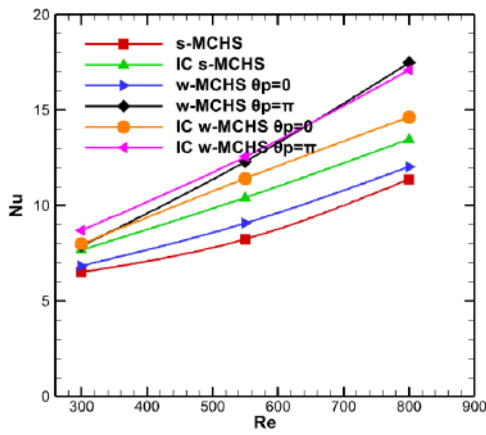

(a)

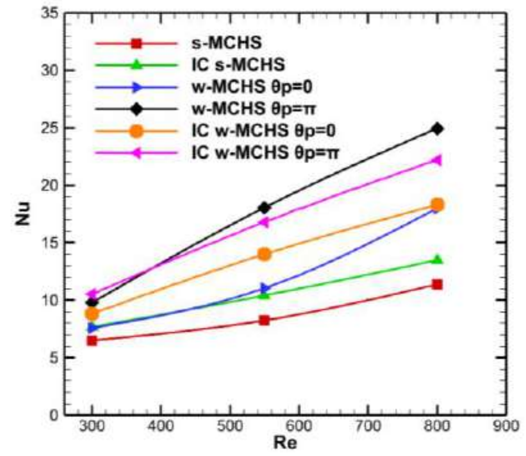

(d)

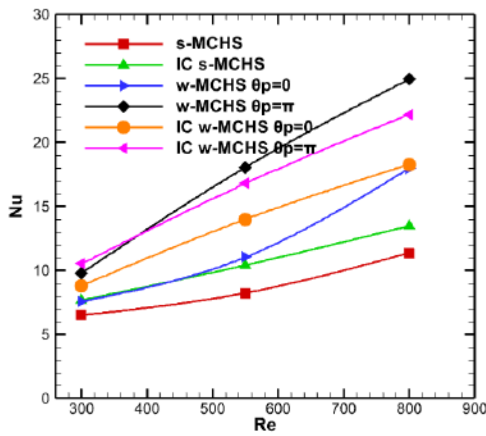

(b)

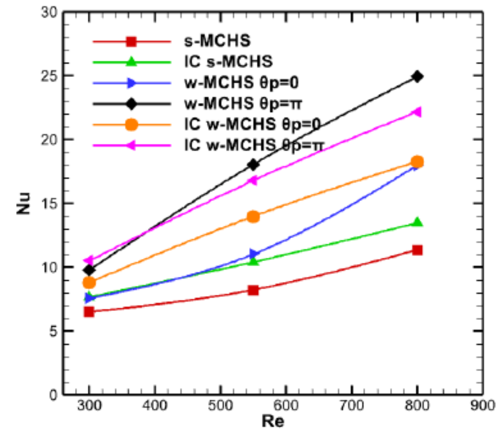

(e)

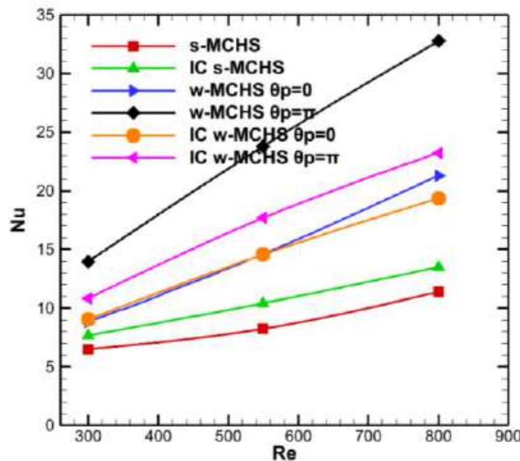

(c)

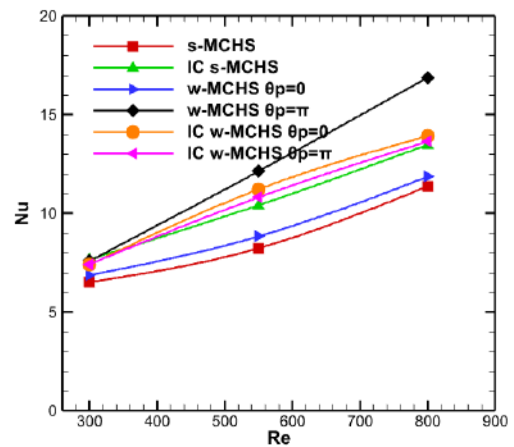

(f)

Figure 4.21: Variation of Nusselt number ratio, *Nu* with *Re* for (a) $\alpha = 0.15$ (b) $\alpha = 0.2$ (c) $\alpha = 0.3$ (d) $\beta = 0.06$ (e) $\beta = 0.08$ (d) $\beta = 0.15$

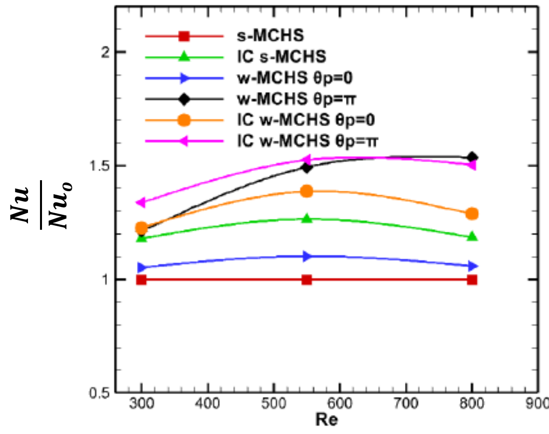

(a)

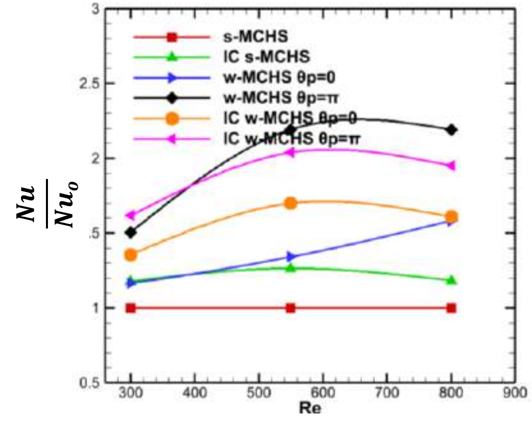

(d)

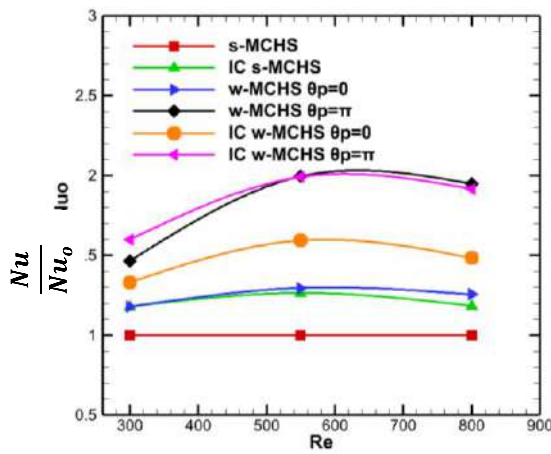

(b)

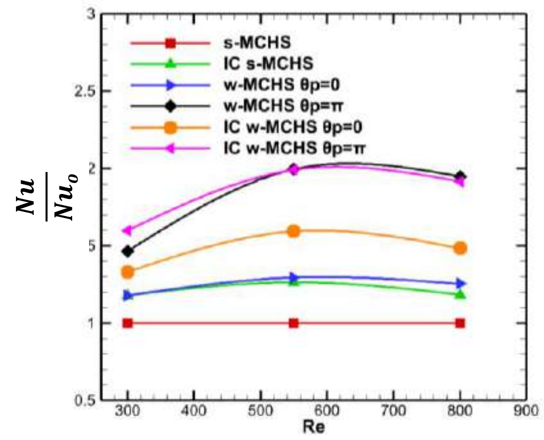

(e)

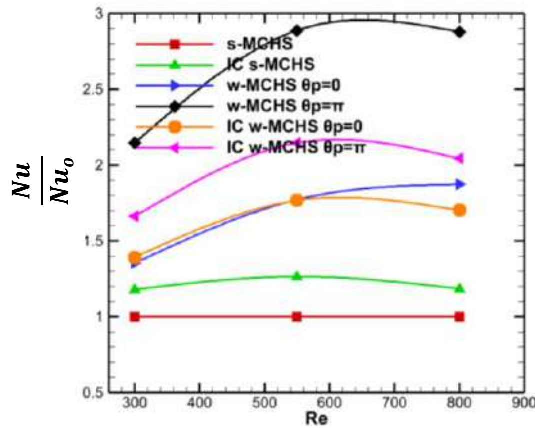

(c)

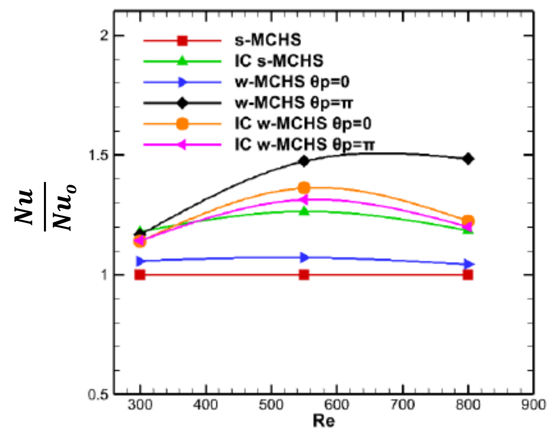

(f)

Figure 4.22: Variation of Nusselt number ration, Nu/Nu_o with Re for (a) $\alpha = 0.15$ (b) $\alpha = 0.2$ (c) $\alpha = 0.3$ (d) $\beta = 0.06$ (e) $\beta = 0.08$ (d) $\beta = 0.15$

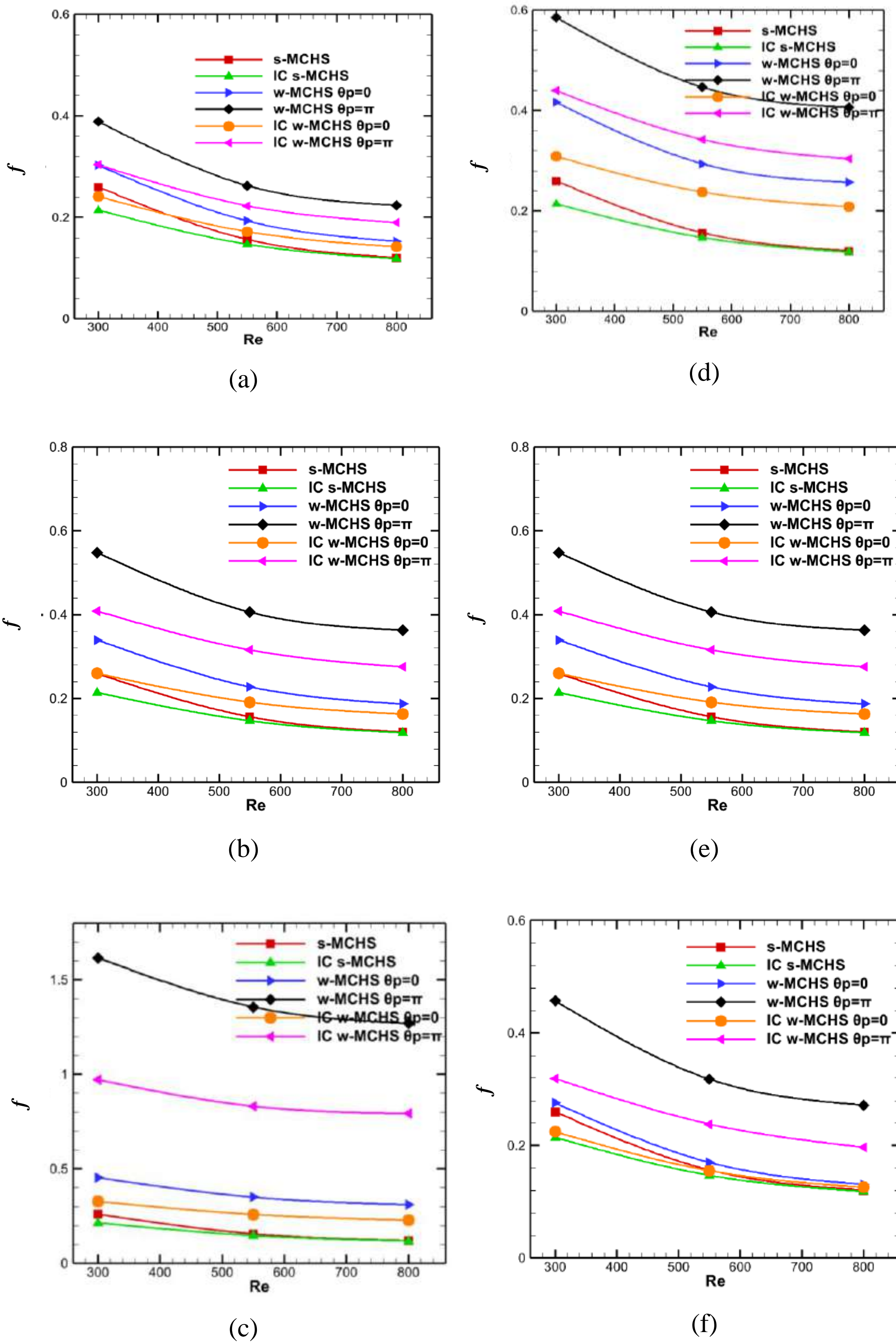

Figure 4.23: Variation of friction factor, f with Re for (a) $\alpha = 0.15$ (b) $\alpha = 0.2$ (c) $\alpha = 0.3$ (d) $\beta = 0.06$ (e) $\beta = 0.08$ (d) $\beta = 0.15$

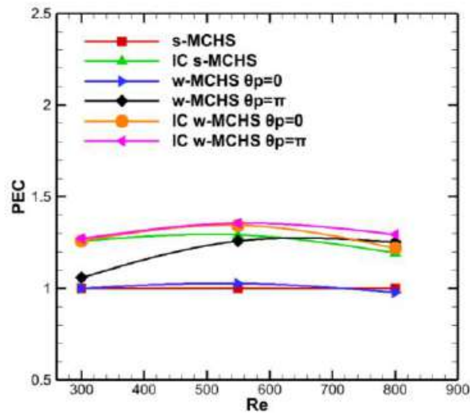

(a)

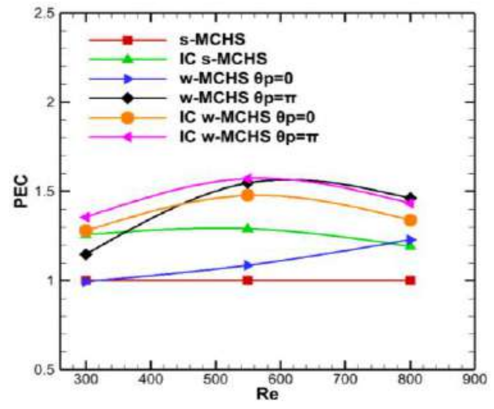

(d)

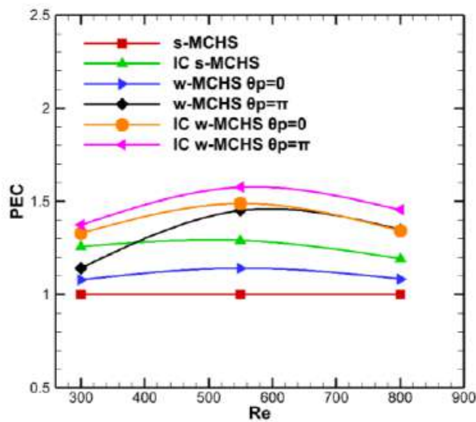

(b)

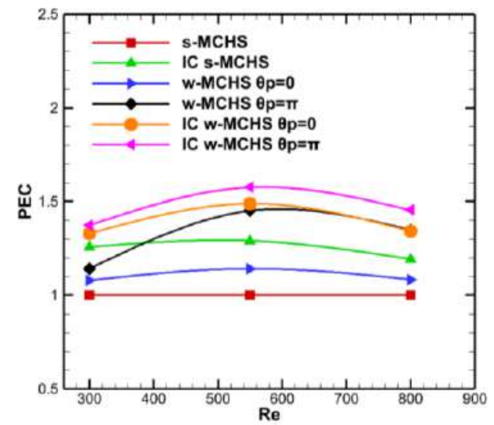

(e)

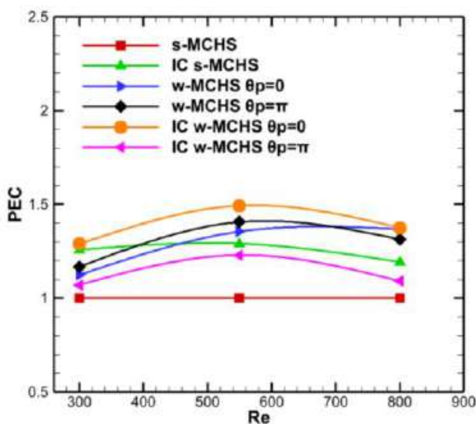

(c)

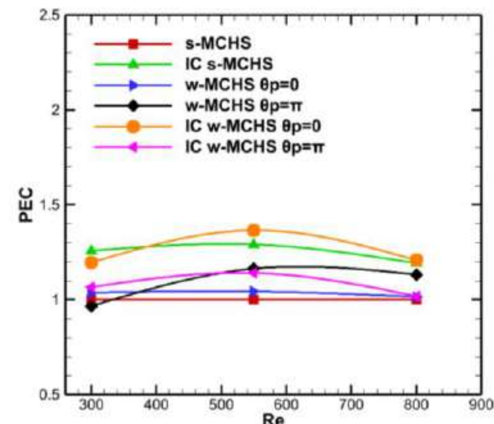

(f)

Figure 4.24: Variation of *PEC* with *Re* for (a) $\alpha = 0.15$ (b) $\alpha = 0.2$ (c) $\alpha = 0.3$ (d) $\beta = 0.06$ (e) $\beta = 0.08$ (d) $\beta = 0.15$

CHAPTER 5: CONCLUSIONS

The present study numerically investigates the fluid flow and heat transfer characteristics of wavy mini-channel with interconnectors (IC w-MCHS) at the laminar regime (*Re 300* to *800*). The wavy parameters such as wavelength (W_L), wave amplitude (W_A), and phase shift (θ_p) are varied to explore its effect on IC w-MCHS. To explore the effect of wave amplitude, three distinct wave amplitude ratio (α) = *0.15, 0.2, 0.3* are studied, keeping wavelength ratio (β)=*0.08* constant at $\theta_p = 0, \pi$. Similarly, to investigate the effect of wavelength, three different β = *0.06, 08, 0.15* are investigated under constant α =*0.3* at $\theta_p = 0, \pi$. The location and size of interconnectors are kept constant for all numerical investigations. The current study indicates that IC w-MCHS shows better thermal and hydrodynamic performance than Conventional Straight MCHS with no interconnectors (s-MCHS), straight mini-channel with interconnectors (IC s-MCHS), and wavy mini-channel with interconnectors (w-MCHS). The results from the numerical investigation can be summarized as follows:

1. Interconnected wavy mini-channel always exhibits superior thermal performance compared to that without interconnectors. Waviness increases with the wave amplitude (α), and so does the heat transfer and pressure drop; wave amplitude ratio (β) has an inverse relation. At *Re 550, 59%* enhancement in *Nu* was found for IC w-MCHS (for α=*0.2*, β = *0.08*, $\theta p = 0^o$) compared to the s-MCHS, whereas, *29%* was found for w-MCHS, and *26%* for IC s-MCHS.
2. The enhancement in heat transfer is also accompanied by the pressure drop penalty. Friction factor (*f*) is calculated as *22%* higher for the IC w-MCHS (for $\theta_p = 0$, α=*0.2*, β = *0.08*) compared to the s-MCHS at *Re 550*, and the friction factor was *45%* higher for the w-MCHS without interconnectors.
3. The vorticity and flow reversal are higher in w-MCHS at $\theta_p = \pi$ compared to $\theta_p = 0$ which results in higher heat transfer rate and higher pressure drop penalty.
4. The effect of interconnects reduces as the Reynolds number increases. At

Re 800 (for $\theta p = \pi$, $\alpha=0.3$, and $\beta=0.08$), *Nu* number for the IC w-MCHS was found to be *115%* higher than the s-MCHS whereas it was *188%* for the w-MCHS. The effectiveness of the interconnects in the wavy channel is also observed to reduce as the wavelength ratio, β decreases. At $\beta=0.08$ (for $\theta p = \pi$, $\alpha=0.2$, and *Re 800*), *Nu* number for the IC w-MCHS was found to be *95%* higher than the s-MCHS whereas, it was *119%* for w-MCHS.

5. Heat removal capacity from the IC w-MCHS was found to be larger in comparison to IC s-MCHS, s-MCHS. Maximum $94\ W/cm^2$, $84\ W/cm^2$, $57\ W/cm^2$, and $49.5\ W/cm^2$ of heat flux are removed (by limiting the surface temperature 85^oC) by w-MCHS, IC w-MCHS, IC s-MCHS, and s-MCHS.
6. IC w-MCHS have lower friction factor, f than w-MCHS. Friction factor, f was found to reduce by 31% for the introducing interconnector in the wavy mini-channel (for $\theta_p = 0$, $\alpha = 0.2$, $\beta.=0.08$ and *Re 800*).
7. Performance evaluation criteria (*PEC*) for IC w-MCHS are higher than w-MCHS, IC s-MCHS, and s-MCHS for all the cases studied. Maximum value recorded for *PEC* are *1.49, 1.14, 1.29,1* for the IC w-MCHS, w-MCHS, IC s-MCHS, s-MCHS, respectively at *Re 550*.

REFERENCES

1. Cengel, Y.A. and A. Ghajar, Heat and mass transfer (a practical approach, SI version). McGraw-670 Hill Education, 2011. 671: p. 52.
2. Incropera, F.P., et al., Fundamentals of heat and mass transfer. Vol. 6. 1996: Wiley New York.
3. Jadhav, M., et al., Review on enhancement of heat transfer by active method. International Journal of Current Engineering and Technology, 2016. 6: p. 221-225.
4. Léal, L., et al., An overview of heat transfer enhancement methods and new perspectives: Focus on active methods using electroactive materials. International Journal of Heat and Mass Transfer, 2013. 61: p. 505-524.
5. Khan, N., D. Pinjala, and K. Toh. Pool boiling heat transfer enhancement by surface modification/micro-structures for electronics cooling: a review. in Proceedings of 6th Electronics Packaging Technology Conference (EPTC 2004)(IEEE Cat. No. 04EX971). 2004. IEEE.
6. Garimella, S.V., Advances in mesoscale thermal management technologies for microelectronics. Microelectronics Journal, 2006. 37(11): p. 1165-1185.
7. Shuvo, A.A., et al. Heat Transfer Characteristics of a Phase Change Material Fluid in Microchannels Under Pulsating Flow Condition. in ASME 2019 Heat Transfer Summer Conference collocated with the ASME 2019 13th International Conference on Energy Sustainability. 2019.
8. Wu, R., et al., An immersed jet array impingement cooling device with distributed returns for direct body liquid cooling of high power electronics. Applied Thermal Engineering, 2019. 162: p. 114259.
9. Kandlikar, S.G. and W.J. Grande, Evolution of Microchannel Flow Passages--Thermohydraulic Performance and Fabrication Technology. Heat Transfer Engineering, 2003. 24(1): p. 3-17.
10. Carballo, J.A., et al. ITRS 2.0: Toward a re-framing of the Semiconductor Technology Roadmap. in 2014 IEEE 32nd International Conference on Computer Design (ICCD). 2014.

11. Hoefflinger, B., ITRS: The International Technology Roadmap for Semiconductors, in Chips 2020: A Guide to the Future of Nanoelectronics, B. Hoefflinger, Editor. 2012, Springer Berlin Heidelberg: Berlin, Heidelberg. p. 161-174.
12. Xiao, H., Z. Liu, and W. Liu, Conjugate heat transfer enhancement in the mini-channel heat sink by realizing the optimized flow pattern. Applied Thermal Engineering, 2021. 182: p. 116131.
13. Naqiuddin, N.H., et al., Overview of micro-channel design for high heat flux application. Renewable and Sustainable Energy Reviews, 2018. 82: p. 901-914.
14. Tuckerman, D. and R. Pease, High-performance heat sinking for VLSI. IEEE Electron Device Letters, 1981. 2: p. 126-129.
15. Phillips, R.J., Microchannel heat sinks. The Lincoln Laboratory Journal, 1988. 1(1): p. 31-48.
16. Zhang, H., et al., Single-phase liquid cooled microchannel heat sink for electronic packages. Applied Thermal Engineering, 2005. 25(10): p. 1472-1487.
17. Kandlikar, S.G., Fundamental issues related to flow boiling in minichannels and microchannels. Experimental Thermal and Fluid Science, 2002. 26(2-4): p. 389-407.
18. Dang, T. and J.-t. Teng, Comparisons of the heat transfer and pressure drop of the microchannel and minichannel heat exchangers. Heat and mass transfer, 2011. 47(10): p. 1311-1322.
19. Tao, W.Q., et al., A unified analysis on enhancing single phase convective heat transfer with field synergy principle. International Journal of Heat and Mass Transfer, 2002. 45(24): p. 4871-4879.
20. Shah, R.K. and A.L. London, Laminar flow forced convection in ducts: a source book for compact heat exchanger analytical data. 2014: Academic press.
21. Steinke, M.E. and S.G. Kandlikar. Single-phase heat transfer enhancement techniques in microchannel and minichannel flows. in International Conference on Nanochannels, Microchannels, and Minichannels. 2004.

22. Oudah, S.K., et al. Thermohydraulic characteristics of a knurled microchannel heat sink in single phase regime. in ASTFE Digital Library. 2018. Begel House Inc.
23. Wu, H.Y. and P. Cheng, An experimental study of convective heat transfer in silicon microchannels with different surface conditions. International Journal of Heat and Mass Transfer, 2003. 46(14): p. 2547-2556.
24. Zheng, Z., D.F. Fletcher, and B.S. Haynes, Laminar heat transfer simulations for periodic zigzag semicircular channels: Chaotic advection and geometric effects. International Journal of Heat and Mass Transfer, 2013. 62: p. 391-401.
25. Chai, L., et al., Optimum thermal design of interrupted microchannel heat sink with rectangular ribs in the transverse microchambers. Applied Thermal Engineering, 2013. 51(1): p. 880-889.
26. Chai, L., et al., Heat transfer enhancement in microchannel heat sinks with periodic expansion–constriction cross-sections. International Journal of Heat and Mass Transfer, 2013. 62: p. 741-751.
27. Li, Y., et al., Characteristics of laminar flow and heat transfer in microchannel heat sink with triangular cavities and rectangular ribs. International Journal of Heat and Mass Transfer, 2016. 98: p. 17-28.
28. Xia, G., Y. Zhai, and Z. Cui, Numerical investigation of thermal enhancement in a micro heat sink with fan-shaped reentrant cavities and internal ribs. Applied Thermal Engineering, 2013. 58(1-2): p. 52-60.
29. Ahmed, H.E. and M.I. Ahmed, Optimum thermal design of triangular, trapezoidal and rectangular grooved microchannel heat sinks. International Communications in Heat and Mass Transfer, 2015. 66: p. 47-57.
30. Xia, G., et al., Effects of structural parameters on fluid flow and heat transfer in a microchannel with aligned fan-shaped reentrant cavities. International Journal of Thermal Sciences, 2011. 50(3): p. 411-419.
31. Sui, Y., et al., Fluid flow and heat transfer in wavy microchannels. International Journal of Heat and Mass Transfer, 2010. 53(13): p. 2760-2772.
32. Mohammed, H.A., P. Gunnasegaran, and N.H. Shuaib, Numerical simulation of heat transfer enhancement in wavy microchannel heat sink. International Communications in Heat and Mass Transfer, 2011. 38(1): p. 63-68.

33. Rostami, J., A. Abbassi, and M. Saffar-Avval, Optimization of conjugate heat transfer in wavy walls microchannels. Applied Thermal Engineering, 2015. 82: p. 318-328.
34. Hung, T.-C. and W.-M. Yan, Effects of tapered-channel design on thermal performance of microchannel heat sink. International Communications in Heat and Mass Transfer, 2012. 39(9): p. 1342-1347.
35. Sui, Y., P.S. Lee, and C.J. Teo, An experimental study of flow friction and heat transfer in wavy microchannels with rectangular cross section. International Journal of Thermal Sciences, 2011. 50(12): p. 2473-2482.
36. Gong, L.J., et al., Thermal performance of microchannels with wavy walls for electronics cooling. IEEE transactions on components, packaging and manufacturing technology, 2011. 1(7): p. 1029-1035.
37. Sakanova, A., C.C. Keian, and J. Zhao, Performance improvements of microchannel heat sink using wavy channel and nanofluids. International Journal of Heat and Mass Transfer, 2015. 89: p. 59-74.
38. Lin, L., et al., Heat transfer enhancement in microchannel heat sink by wavy channel with changing wavelength/amplitude. International Journal of Thermal Sciences, 2017. 118: p. 423-434.
39. Gong, L., et al., Parametric numerical study of flow and heat transfer in microchannels with wavy walls. Journal of Heat Transfer, 2011. 133(5).
40. Khoshvaght-Aliabadi, M., A. Abbaszadeh, and M.M. Rashidi, Comparison of Co- and counter-current modes of operation for wavy minichannel heat sinks (WMHSs). International Journal of Thermal Sciences, 2022. 171: p. 107189.
41. Nilpueng, K. and S. Wongwises, Flow pattern and pressure drop of vertical upward gas–liquid flow in sinusoidal wavy channels. Experimental Thermal and Fluid Science, 2006. 30(6): p. 523-534.
42. Nilpueng, K., et al., Heat transfer and flow characteristics of sinusoidal wavy plate fin heat sink with and without crosscut flow control. International Journal of Heat and Mass Transfer, 2019. 137: p. 565-572.
43. Lee, Y.-J., P.-S. Lee, and S.-K. Chou. Experimental investigation of oblique finned microchannel heat sink+. in 2010 12th IEEE Intersociety Conference on

Thermal and Thermomechanical Phenomena in Electronic Systems. 2010. IEEE.

44. Lee, Y., P. Lee, and S. Chou, Enhanced thermal transport in microchannel using oblique fins. Journal of Heat Transfer, 2012. 134(10).
45. Lee, Y.J., P.K. Singh, and P.S. Lee, Fluid flow and heat transfer investigations on enhanced microchannel heat sink using oblique fins with parametric study. International Journal of Heat and Mass Transfer, 2015. 81: p. 325-336.
46. Fan, Y., et al., A simulation and experimental study of fluid flow and heat transfer on cylindrical oblique-finned heat sink. International Journal of Heat and Mass Transfer, 2013. 61: p. 62-72.
47. Chiam, Z.L., et al., Investigation of fluid flow and heat transfer in wavy micro-channels with alternating secondary branches. International Journal of Heat and Mass Transfer, 2016. 101: p. 1316-1330.
48. Tikadar, A., et al., Parametric study on thermal and hydraulic characteristics of inter-connected parallel and counter flow mini-channel heat sink. Applied Thermal Engineering, 2019. 153: p. 15-28.
49. Tikadar, A., et al., Enhancing thermal-hydraulic performance of counter flow mini-channel heat sinks utilizing secondary flow: Numerical study with experimental validation. International Communications in Heat and Mass Transfer, 2020. 111: p. 104447.
50. Japar, W.M.A.A., N.A.C. Sidik, and S. Mat, A comprehensive study on heat transfer enhancement in microchannel heat sink with secondary channel. International Communications in Heat and Mass Transfer, 2018. 99: p. 62-81.
51. Fluent, A., Ansys fluent. Academic Research. Release, 2015. 14.
52. Ho, C.J. and W.C. Chen, An experimental study on thermal performance of Al2O3/water nanofluid in a minichannel heat sink. Applied Thermal Engineering, 2013. 50(1): p. 516-522.
53. Shah, R. Thermal entry length solutions for the circular tube and parallel plates. in Proceedings of 3rd national heat and mass transfer conference. 1975. Indian Institute of Technology Bombay.

54. Ho, C.-J. and W. Chen, An experimental study on thermal performance of Al2O3/water nanofluid in a minichannel heat sink. Applied Thermal Engineering, 2013. 50(1): p. 516-522.